Common-path interferometric sensing with resonant dielectric nanostructures

Isabel Barth

Doctor of Philosophy

University of York
Physics

April 2021

Abstract

Photonic sensors have the potential to enable highly sensitive point-of-care diagnostic technology and become an essential element of the global health system. To maximise its benefits, the technology needs to provide affordability in addition to accuracy, which is a challenge that is reflected in the currently available diagnostic technologies. For example, the gold standard diagnostic technology, enzyme-linked immunosorbent assay, requires trained personnel and a well-equipped laboratory. In contrast, the low-cost lateral flow devices offer limited sensitivity. New technologies are emerging, such as label-free photonic biosensors that are intrinsically simple, as they can directly monitor the presence of a target biomarker without requiring additional processing steps. However, when high sensitivity is required, they typically rely on expensive components.

Circumventing the connection between high cost and high performance in photonic biosensing and demonstrating a viable alternative requires a novel approach and is the primary aim of my thesis. To this end, I have developed a common-path interferometric sensor based on guided-mode resonances to combine high performance with inherent stability. The concept of spatially superimposing two beams carrying the phase information of two orthogonally polarised resonant modes and interferometrically measuring the relative phase difference between them is here introduced and experimentally realised. To validate the developed technology, the sensor is applied to bulk refractive index sensing as well as the proof-of-principle detection of procalcitonin.

The results of this thesis reveal the interesting physics involved in an interferometric probing of resonances in dielectric nanostructures and indicate the potential of the developed sensor for high-performance diagnostics based on photonics.

Acknowledgments

Since this is where I want to thank the people who have enabled or positively influenced my PhD, the first person to mention is Prof. Thomas F Krauss. Taking excellent supervision for granted seems an easy trap to fall in for one who has never tried before, so I want to thank Thomas especially for trusting but challenging me, for giving me freedom but helping me while always listening and not only accepting but even encouraging me to disagree on eye level.

Thank you also to my first mentor, Dr. Maria Dienerowitz from my time in Jena, and my friend and supervisor Dr. Thorsten Klein from my time in Bremen, who both still encourage me and who's energy and humour against all odds is inspiring.

Then there are numerous colleagues who directly or indirectly helped me. The most important by far were Dr. Jose Juan-Colas (Pepe), Dr. Giampaolo Pitruzzello and Dr. Donato Conteduca with their true interest in science, their encouragement, advice, discussions and friendship. Many thanks also to Dr. Yue Wang and Dr. Christopher Reardon, since they are the constants to rely on. Thank you also to Dr. Kezheng Li, Dr. Stephen Thorpe, Ben Kraus, Alexander Drayton, Manuel Deckart, Dr. Augusto Martins, Dr. Steven Johnson, Dr. Casper Kunstmann-Olsen, Callum Silver, Kalum Thurgood-Parkes, Rhys Ashton, Guilherme Simoneti de Arruda, Dr. Ben Coulson, Dr. Lisa Miller and Adam Stroughair.

Thank you to Prof. Deborah O'Connell and especially Dr. Chris Murphy from the York Plasma Institute for asking great questions and being very supportive during our PhD progression meetings.

Thanks to our collaborator Dr. Steven D. Quinn from York, who introduced me the fascinating research on Alzheimer's disease and who provided the β-amyloid proteins for the corresponding experiments shown in this thesis.

I wish to thank Prof. Emiliano R Martins for indirectly challenging me through his high expectations regarding theoretical understanding and for his patience in answering my questions as well as Thomas for enabling our discussions.

Then I want to thank Daniel Clarke, Dr. James Cubiss, Prof. Kevin O'Grady, Ian Helliwell, Olga Rowe, Mark Laughton and especially Simon Oldfield, who were teaching and supervising B.Sc students with me in the laboratory and from whom I learned.

Then there is my former supervisor Dr. Mostafa Agour in Bremen, who I thank for his advice and friendly words during my PhD.

Thank you also to my friend and teacher Raul Rietmann de Freitas who invited me to speak to his young students in Brazil about my science. This opportunity made me realise that I have the enjoyable responsibility to share what I have learnt thus far so that future scientists might be encouraged.

To my friends in Germany, Brazil and India who despite the distance still keep in touch.

I am very lucky to have a family who actively supported me throughout my life without any exception. With respect to my PhD, I thank my family for their support and for always creating a home independent of where we all are. Even in times of uncertainty and separation my parents Heidrun and Erhardt and my wonderful sisters Clarissa and Lisa are always there. Our relationship of trust and reliability allows me to explore and take risks so my family was fundamental to this work.

In the end, the most important person to thank is my partner Donato. Thank you for the numerous occasions in these last years where you prioritised to encourage and strengthen me above everything else. Your consistent kindness, humour, friendship and love are the reasons why we overcame challenges in the good way we did and this thesis is therefore dedicated to you.

Declaration of Authorship

I declare that this thesis is a presentation of original work and I am the sole author. This work has not previously been presented for an award at this, or any other, University. Any ideas, fabrications, experiments, simulations, images and figures were conceived, performed, taken or made by myself unless indicated otherwise. All sources are acknowledged as references.

____-

Signature - Isabel Barth York, April 30, 2021

Nothing in life is to be feared, it is only to be understood.

- Marie Skłodowska Curie

Contents

1 Motivation and State of the Art 1

1.1 Motivation for point-of-care diagnostics 1

1.2 Motivational focus on antimicrobial guidance 2

1.3 Introduction to evanescent-wave optical biosensors 5

1.3.1 Plasmonic biosensors 7

1.3.2 Interferometric waveguide-based biosensors 9

1.3.3 Guided-mode resonance- and metasurface-based biosensors . 10

1.4 Objectives and summary of this work 12

2 Theory 14

2.1 Basics of photonics 14

2.1.1 Dielectric materials and the concept of refractive index 14

2.1.2 Maxwell's equations 15

2.1.3 Evanescent electromagnetic fields 16

2.1.4 Diffraction gratings 18

2.1.5 Waveguides 19

2.2 Guided-mode resonances 22

2.2.1 Bloch's theorem 23

2.2.2 Photonic band structure 24

2.2.3 Fano resonances 26

2.2.4 Phase response of Fano resonances 28

2.2.5 Mode confinement 29

2.2.6 Resonance regime dependence on grating parameters 29

2.2.7 Bound states in the continuum - terminology 33

2.3 Figures of merit for biosensing 33

2.3.1 Quality factor and phase sensitivity 34

2.3.2 Bulk sensitivity 36
2.3.3 Surface sensitivity 36
2.3.4 Signal-to-noise ratio 38
2.3.5 Limit of detection 39
2.3.6 Refractive index dynamic range 39
2.4 Theory of interferometry 41

3 Principle, Design, and Realisation of Resonant Phase Read-out 44

3.1 Resonant common-path interferometry principle 44
3.2 Optical setup for common-path interferometry 45
3.3 Design and fabrication of resonant nanostructures 48
3.4 Experimental realisation of resonant interferogram formation 55
3.5 Principle of phase extraction 56
3.6 Discussion 59

4 Experimental Resonant Phase Measurements 64

4.1 Noise and drift characterisation 64
4.1.1 Mechanical drift 64
4.1.2 Influence of fringe contrast on read-out noise 65
4.1.3 Temperature drift 67
4.1.4 Discussion 68
4.2 Experimental phase sensitivity 71
4.2.1 Calibration 71
4.2.2 Experimental phase sensitivity 71
4.2.3 Dynamic range extension experiments 73
4.3 Discussion 78

5 Experimental Protein Sensing 80

5.1 Principle of photonic protein sensing 80
5.2 Specificity 80
5.3 Procalcitonin sensing experiments 81
5.3.1 Interferometric procalcitonin sensing experiments 81
5.3.2 Procalcitonin control experiments 84
5.4 β-Amyloid sensing experiments 87
5.4.1 β-Amyloid control experiments 88
5.4.2 Interferometric β-amyloid sensing experiments 89

6 Outlook: Preliminary Results of Ongoing Projects 91
6.1 Interferometric sensing with dielectric nanohole arrays and visible light 91
6.2 Miniaturised interferometric setup for point-of-care device prototype . 94
6.3 Protein sensing in serum experiments 99
6.4 Alternative high-Q modes for phase sensitivity improvement 101
6.5 On ‘dark modes’ for surface enhanced interferometric scattering microscopy 105

7 Overall summary and conclusions 111

8 Appendix 125
8.1 Simulation methods 125
8.1.1 Rigorous coupled wave analysis - principle and implementation 125
8.1.2 Stanford Stratified Structure Solver (S^4) 126
8.1.3 S^4 simulation harmonics convergence test 126
8.2 Detailed experimental methods 128
8.2.1 Dielectric nanostructure fabrication 128
8.2.2 Microfluidics fabrication 128
8.2.3 Surface functionalisation protocol 130

8.2.4 Optical setup and data acquisition methods 130

8.3 Data processing methods 132

8.4 List of Figures 133

Publications, Awards and Conference Attendances

Conferences & Summer Schools

- World Congress on Biosensors 2020, postponed to July 2021, invited talk
- Europt(r)ode 2020, postponed to November 2021, talk
- CLEO Europe 2019, Munich, talk
- Nanophotonics Summer school AMOLF 2019, Amsterdam, poster
- International Conference on Biophotonics 2019, St Andrews, poster
- Centre for Future Health Research Impact Conference 2019, York, poster
- European Doctoral Summer School in Professional Development 2019, York
- Physics of Life Summer school 2018, Durham, poster

Publications

- I. Barth, D. Conteduca, C. Reardon, S. Johnson, T. F. Krauss. *Common-path interferometric label-free protein sensing with resonant dielectric nanostructures*. Light, Science & Applications 9, 96, **2020**
- D. Conteduca, I. Barth, G. Pitruzzello, C. Reardon, E. Martins, T. F. Krauss. *Dielectric Nanohole Array Metasurface For High-Resolution Near-Field Sensing and Imaging*, Nature Communications, 12, 3293 **2021**
- A. Drayton, I. Barth, T.F. Krauss, *Guided mode resonances and photonic crystals for biosensing and imaging*, Semiconductors and Semimetals, 100, pp. 115-148, **2019**

- A. Kenaan, K. Li, I. Barth, S. Johnson, J. Song, T. F. Krauss. *Guided mode resonance sensor for the parallel detection of multiple protein biomarkers in human urine with high sensitivity*. Biosensors and Bioelectronics 153, **2020**
- K. Li, R. Gupta, A. Drayton, I. Barth, D. Conteduca, C. Reardon, K. Dholakia, T. F. Krauss. *Extended Kalman Filtering Projection Method to Reduce the 3σ Noise Value of Optical Biosensors*. ACS sensors, 5, 11, 3474–3482, **2020**
- I. Barth, D. Conteduca, A. Drayton, T. F. Krauss. *Towards highly sensitive point-of-care diagnostics with common-path interferometric dielectric nanostructures*. European Conference on Biomedical Optics, ETh3A. 6, **2021**
- I. Barth and T. F. Krauss, *Interferometric sensing with guided-mode resonances*, in 2019 Conference on Lasers and Electro-Optics Europe and European Quantum Electronics Conference, OSA Technical Digest (Optical Society of America), **2019**
- A. Kenaan, K. Li, I. Barth, S. Johnson, J. Song, and T. Krauss *Label-free Chirped Guided Mode Resonance Biosensor Employing Polyethylene Glycol Spacers for Urinary Immunoglobulin G Detection* , in Conference Optics and Photonics for Sensing the Environment, Optical Sensors and Sensing Congress (ES, FTS, HISE, Sensors) (Optical Society of America), **2019**
- J. Juan-Colas, D. Conteduca, I. Barth and T. F. Krauss *Guided Mode Resonances For Sensing And Imaging*, in Conference EPJ Web of Conferences 215, 11001 (2019) (EOS Optical Technologies), **2019**

Awards

- Physics Postgraduate Conference, York, 2020 Best Talk - First place

- Rank Prize Funds Optoelectronics 2020 - COVID-19 Student hardship fund award

1 Motivation and State of the Art

Scientific advances are often initiated by a vision for our future resulting from observation (What is our current situation and why?) and imagination (What could be a preferable alternative?). The scientific realisation of a vision then also requires observation and imagination on a different level.

This introduction aims to explain the observations which have led to the vision of point-of-care diagnostic technology within an alternative future medical world as well as state-of-the-art scientific development towards this vision based on photonic technologies.

1.1 Motivation for point-of-care diagnostics

An earlier diagnosis of a disease and the continuous monitoring of the response to a treatment can increase the life expectancy of patients [1]. Moreover, early diagnosis leading to effective treatment can prevent hospitalisation and therefore save resources. A specific example is the high demand for fast and targeted antibiotic guidance [2], which is one of the chosen applications of this work, potentially proceeding from point-of-care (POC) diagnostic tools.

Although the need for early diagnosis is well recognised, the necessary technology is currently not available for general practitioners while the time-consuming enzyme-linked immunosorbent assay (ELISA), which was invented in the 1960s and revolutionised clinical diagnosis [3], is still the most widely used biomarker detection technology in clinical settings. ELISA is based on enzyme labels attached to either the antigen or the antibody [4] and is performed in specialised laboratories. The goal of POC diagnostics is to give clinicians a tool that saves valuable time, which is currently used to analyse patient samples in external laboratories. A bolder vision also includes pharmacists and the patients themselves as potential direct users of POC technology

[1].

Associated scientific challenges of developing such broadly applicable diagnostic devices lies in the need for highly sensitive and specific detection of low concentrations of biomarkers in a low-cost platform that can be operated by non-specialists. One relevant reason why the clinical translation of POC devices is still a challenge is that high performance and reliable sensing is often achieved based on high complexity and cost and, on the other hand, the performance of low-cost platforms is often inherently limited to biomarker concentration levels which are not clinically relevant and significantly inferior to ELISA.

For these reasons, the development of high-sensitivity and yet low-complexity diagnostic platforms requires a novel approach with consequently new opportunities for improving the delivery and speed of diagnostic tests which will initiate the move towards personalised treatment.

1.2 Motivational focus on antimicrobial guidance

There are many possible examples illustrating the benefit of a POC-system; of these, antimicrobial resistance (AMR) is particularly urgent, which is why it is one of the drivers of this work. AMR is the result of an evolutionary process causing bacteria, viruses, fungi or parasites to stop responding to an antimicrobial drug which was previously able to inhibit their growth [5]. Bacteria can evolve to be resistant against very different kinds of stress inducing environmental factors introduced by human society including not only common antibiotics but recently also e.g. silver nanoparticles [6]. We now know that antibiotic resistance is ancient [7] based on 30.000 year old genes showing resistance to β-lactam, tetracycline and glycopeptide antibiotics, but it was the discoverer of penicillin, Alexander Fleming, who formally described the evidence of bacterial resistance to penicillin in 1929 [8], around one year after he discovered the new drug. There, an agar disk diffusion test was used to monitor bacterial growth over time, which is still the most used susceptibility test method today [9], and Fleming made the following observations :

A certain type of penicillium produces in culture a powerful antibacterial substance. The antibacterial power of the culture reaches its maximum in about 7 days at 20°C and after 10 days diminishes until it has almost disappeared in 4 weeks.

At that time, researchers did not know how the resistance against penicillin was generated by the bacteria but 10 years later a paper was published identifying that in this specific case it was *An Enzyme from Bacteria able to Destroy Penicillin* [10] which caused the resistance to emerge. This is only one of the many creative solutions found by bacteria to escape the threat of antimicrobial drugs when these are endangering their survival.

From the perspective of human society, the evolution of bacterial adaption to our drugs is currently faster than our ability to invent new drugs or adapt in other ways. Even synthetic antibiotics, which did not exist in nature before their introduction through humans, can lead to harmful resistance over a relatively short period of time. Quinolone resistance, for example, was shown to be the cause of methicillin-resistant Staphylococcus aureus (MRSA) in hospitals [11]. The difference in the rate at which bacteria evolve compared to the human adaption rate is starting to reverse the benefits that antibiotics were able to provide for our health since their discovery. Usually, the threat is described in strong words to express the urgent need for solutions. The World Health Organisation (WHO) stated in 2014 [5]:

The problem is so serious that it threatens the achievements of modern medicine. A post-antibiotic era in which common infections and minor injuries can kill is a very *real possibility for the 21st century.*

Importantly, AMR is influencing our possibility to profit from life prolonging interventions like surgery, transplantation, and chemotherapy because these are often associated with infections. This future possibility of our increasing inability to treat infections with antibiotics is the reason why scientists from a variety of scientific backgrounds are working on AMR to address the following not yet sufficiently understood factors [2]:

1. Personalised optimum antibiotic treatment duration and dosage and the combination of different antibiotics
2. New drug discovery and optimisation of current drugs
3. Reduction in prevalence and transmission of resistant organisms
4. Better understanding of resistance mechanisms
5. Fast and targeted infection diagnostics

These factors are influencing each other and progress in one area can result in a completely new approach regarding another area. For example, if there is progress in the understanding of the biomolecular mechanisms of resistance, this could possibly lead to a different and more effective way of diagnostics even with a technology that already existed but could not be applied before. Another example would be the applicability of a more targeted and simple POC diagnostic technology to help reduce the transmission of resistant organisms and even increase the introduction of new antibiotics due to a higher awareness and cost reduction of clinical trials. Rapid diagnostics could avoid the currently occurring need to blindly prescribe broadband antibiotics as the only option to potentially treat infections on time. Diagnosing on a short time-scale is highly relevant since, e.g., sepsis is the main cause of death in intensive care units due

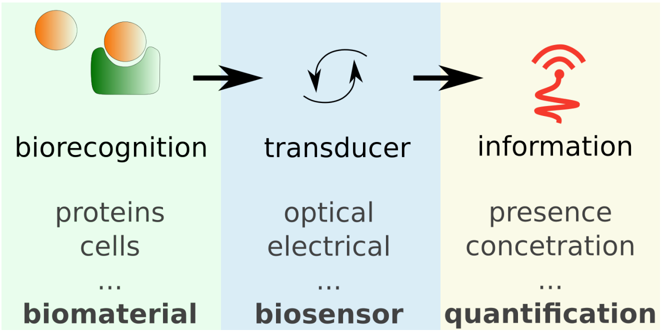

Figure 1: Schematic principle of biosensor operation as transducer. Biorecognition is commonly achieved with specific antibodies binding to a target molecule while the transducer (biosensor) enables the translation of the biorecognition into a measurable signal.

to delayed diagnosis and uninformed antibiotic therapy [1]. In addition to the direct detection and identification of specific bacteria, POC technology can also help by detecting associated biomarkers, e.g. C-reactive protein (CRP) and procalcitonin (PCT), to distinguish between viral and bacterial infections.

1.3 Introduction to evanescent-wave optical biosensors

Biosensors in general are transducers of the presence and concentration of biological material into a quantitative sensor-response information (Fig. 1). The transducer can be based on a variety of different technologies, for example electrochemical or optical approaches, and the range of biological material is also wide, including biomolecules and microorganisms.

Motivated by the above described need for POC diagnostics, photonic and plasmonic label-free sensors have evolved rapidly in the last years [12–14] with a recent further acceleration due to the Covid-19 pandemic [15]. The development not only relates to the sensing aspect but also the multiplexing capabilities, microfluidic integration and miniaturisation with the final vision of next generation biosensors to be highly sensitive, mass produced and cost-efficient while delivering real-time and reliable results

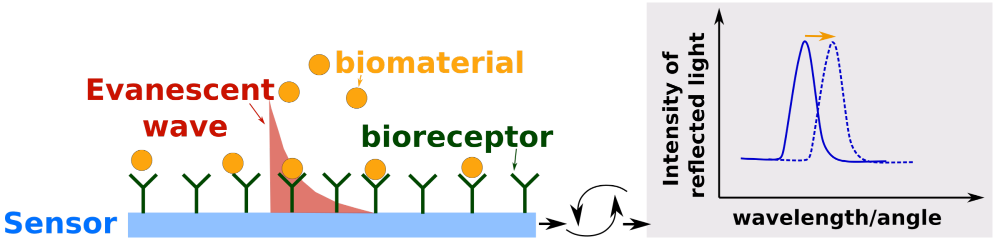

Figure 2: Principle of evanescent field refractive index sensing schematic. Any evanescent field refractive index biosensor relies on an effective index change caused by the presence of biomaterial, which perturbes the evanescent field. This effective index change is transduced usually by analysing the response in resonance wavelength or angle.

with low sample volumes [16].

For biosensing in general, label-free approaches minimise the problem of steric hindrance and potential alterations of the structural configuration of the target biomarker or the bio-receptor, which is associated with fluorescent markers [17]. The affinity of a biomarker towards the corresponding bioreceptor is therefore less disturbed in label-free biosensors compared to e.g. fluorescence-based detection. Moreover, for a time- and cost-efficient POC sensor to address challenges like AMR, the absence of labels is advantageous because of the cost and complexity associated with labelling. The following summary of the state-of-the-art of relevant photonic sensors is therefore limited to label-free approaches only. For fluorescence and nanoparticle based sensing, I refer to exemplary review papers [18, 19].

Photonic and plasmonic label-free sensors rely on evanescent field refractive index sensing (Fig. 2) and the associated light-confinement at the nanometre scale. Binding of biomarkers within the range of these evanescent fields, which are decaying exponentially from the sensor surface, perturbs the field and changes the effective index of the mode. This change in effective index can be monitored over time to extract information such as the antibody-antigen binding kinetics. Because the evanescent field typically decays within tens to a few hundreds of nanometres, only selectively surface-bound biomarkers contribute to the effective index change, conferring specificity in addition to sensitivity.

Evanescent field refractive index sensors have therefore proven to be well suited for high-sensitivity and label-free biosensing; amongst these, interferometric approaches provide particularly low limits of detection (LOD), defining the smallest measurable refractive index change, which translates into the lowest detectable biomarker concentration. Interferometric sensing in general relies on measuring optical path differences between a reference and a signal beam and thereby extracting information regarding the size or refractive index of a sample.

The advantages of phase-sensitive read-out approaches become particularly relevant in the POC environment when common-path techniques are used, because common-path techniques are inherently noise-tolerant [20]. Since the work presented here is a combination of photonic sensing and interferometry, the following state-of-the-art of the most relevant photonic sensor technologies has a focus on associated interferometric detection schemes.

1.3.1 Plasmonic biosensors

Plasmonic sensors have been extensively optimised over the last thirty years and are now one of the most used and commercialised label-free sensing techniques [21] because of the very high bulk sensitivities (3300 $\mathrm{nm\,RIU^{-1}}$ [22]), where RIU means ‘refractive index units’, and low protein LODs (typically $10\,\mathrm{pg\,mL^{-1}}$ [17]). Most recently, plasmonic-based biosensors have been applied to viral diagnostics [23], ultra-sensitive detection of miRNA [24] or malaria biomarkers [25].

The principle of surface plasmon resonance (SPR) sensors relies on light induced electron oscillations on the surface of a metal film (e.g. gold) at a specific incidence angle, called plasmons, which generate an electric field decaying from the metal surface into

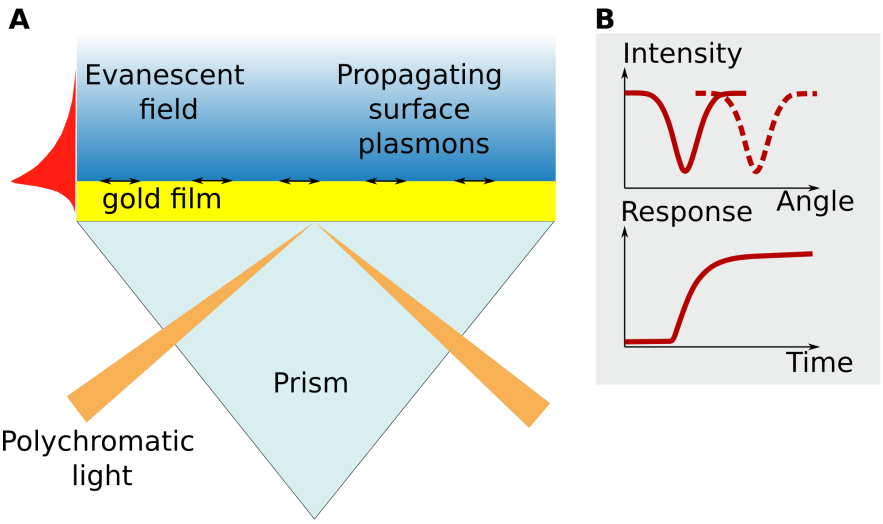

Figure 3: Attenuated total reflection method (Kretschmann geometry) used for exciting a surface plasmon resonance. Figure adapted from [17].

the dielectric medium above the gold surface (Fig. 3 A). A refractive index alteration changes the resonance condition of the SPR, which is usually determined experimentally by finding the corresponding change in resonance incidence angle.

SPR is commonly used to monitor biomolecular interactions in real-time and so extract quantitative binding kinetics information (Fig. 3 B).

An interferometric version of the SPR modality was first introduced in 1997 by Kabashin and Nikitin [26], demonstrating an improvement in LOD by two orders of magnitude (to $4 \cdot 10^{-8}$ RIU) compared to the conventional non-interferometric angular interrogation. The downside of this method, however, is the trade-off between sensitivity and dynamic range [20, 27]. For example, interferometric SPR can achieve LODs of $\Delta n \approx 10^{-8}$, but this sensitivity is only achieved over $5 \cdot 10^{-5}$ RIU, unless advanced designs are used that are costly and thus not suitable for POC applications [27].

An intrinsically simpler approach is to exploit the phase sensitivity of plasmonic nanostructures with strongly localised fields, such as gold nanohole arrays [28] which avoid the need for prism-coupling and have shown LODs of order of 10^{-4} RIU with detec-

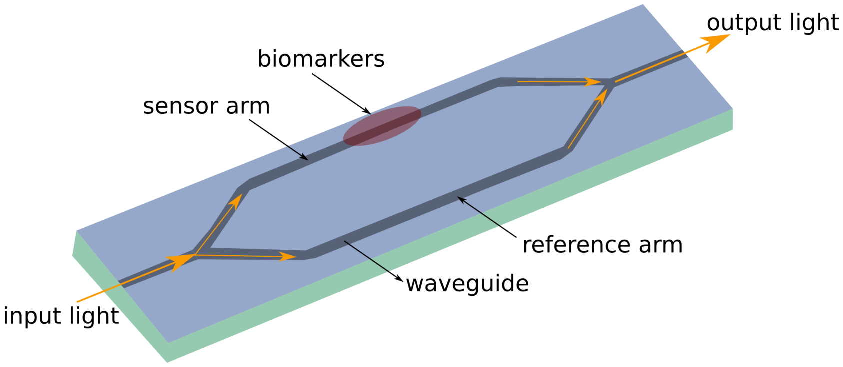

Figure 4: Schematic of standard planar waveguide Mach-Zehnder-Interferometer configuration adapted from [34].

tion limits for proteins in the tens of $\mu g\,mL^{-1}$ range [29] down to clinically relevant 145 $pg\,mL^{-1}$ in complex media [30].

Despite the extensive optimisation of these plasmonic-based biosensors, they are not yet used in clinical settings. Their limited LODs for biomolecular detection can be in some cases be outperformed by silicon resonators or waveguides showing pico- or even attomolar LODs [1]. These will be introduced in the following.

1.3.2 Interferometric waveguide-based biosensors

Interferometric waveguide-based biosensors consist of a sensor waveguide, which is interacting with the biomaterial, while a reference waveguide remains insensitive to refractive index changes (Fig. 4). The phase shift in the signal arm upon biomarker binding in the evanescent field is extracted by recombining the reference and signal arm and recording the interference dependent intensity modulations. Examples of high performance interferometric systems are integrated Mach-Zehnder interferometers (MZI) [31, 32] and Young interferometers [33] based on planar optical waveguides, which show state-of-the-art bulk LODs of order 10^{-8} RIU.

The difference between Mach-Zehnder (MZI) and Young-interferometers (YI) is the on-chip arm recombination and intensity detection in the MZI-case, while the YI generates an off-chip interferogram recorded with a camera. A bimodal interferometric waveguide sensor is a variant of the MZI showing LODs of $\approx 10^{-7}$ RIU [35], which is typical for interferometric approaches. Recent applications of waveguide-based interferometric biosensors include for example the detection of bacteria genes [36] or Covid-19 diagnostics [37].

With respect to POC devices, the disadvantage of these approaches is the relatively large footprint ($\approx$ 10 mm length) and the need for precise light coupling into waveguides, which requires high-precision angular and spatial alignment [38].

1.3.3 Guided-mode resonance- and metasurface-based biosensors

Photonic crystal (PhC) biosensors describe all sensors based on a dielectric structure with a periodically varying refractive index in typically one or two directions. Guided-mode resonance (GMR)-based sensors, which are the photonic resonances relevant to this work, are a subtype of PhC sensors [38]. A one-dimensional PhC slab, for example, is a dielectric grating supporting GMRs for out-of-plane excitation (Fig. 5), which enables large field-of-view imaging capabilities and therefore multiplexed sensing for POC. The collimated input light is diffracted by the periodic dielectric nanostructure such that it is guided in the nanostructure itself, which leads to ‘leaky’ resonant modes and an evanescent field on the sensor surface. The physical principles behind the GMR phenomenon will be discussed in detail in the theory sections below.

Typically, the resonantly reflected light is analysed with respect to refractive index alterations on the sensor surface either by measuring refractive index dependent changes in intensity or resonance wavelength.

The advantageous aspects of GMR have been first recognised and applied to biosensing by Magnusson et al. [40] and Cunningham et al. [41].

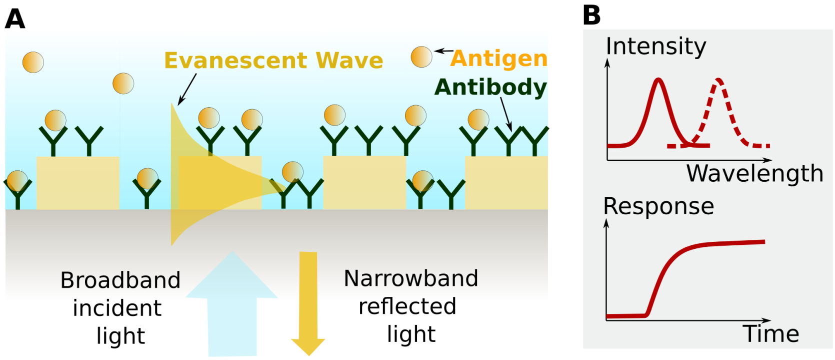

Figure 5: Guided-mode resonance (GMR) schematic sensing principle. A narrow range of wavelengths of the broadband incident light is resonantly guided in the grating layer and coupled out again, such that an intensity peak is observed in reflection. The resulting evanscent field is perturbed by the target biomolecules, which changes the effective index of the 'leaky' guided mode. The corresponding change in resonance wavelength is typically observed with a spectrometer. Adapted from [39].

Most other high-performance sensor modalities require expensive light sources, spectrometers or other readout instruments and often need precise coupling arrangements; the GMR approach can operate without any of these requirements, which includes dielectric metasurfaces that are phenomenologically equivalent. The advantages are out-of-plane coupling, high sensitivity as well as a wide field-of-view for multiplexed sensing. In particular, the chirped GMR approach translates spectral into spatial information to remove the need for a spectrometer and reaches a protein LOD of 267 pM despite its simplicity [42]. Following the same idea of translating spectral into spatial information, dielectric metasurfaces based on elliptical elements have recently been introduced [43, 44] reaching similarly low LODs.

These approaches based on dielectric nanostructures offer the necessary simplicity required for future miniaturisation and the required sensitivity for many biosensing applications.

The first proposal to explore the phase response of GMRs for sensing applications dates back to 2004 [45], where the rapid phase variation on resonance was studied in simulation and an enhanced detection sensitivity was predicted for an interferometric read-out approach. The first experimental realisation of this idea was not demonstrated until ten years later with a transmission type guided-mode resonance sensor in a heterodyne interferometer configuration [46]. The same group also investigated an approach based on phase shift interferometry [47]. Both approaches require complex experimental equipment and phase reconstruction methods. An alternative is to use an external Mach-Zehnder configuration [48]. The issue with the external Mach-Zehnder is its sensitivity to environmental noise, rendering it unsuitable for POC applications.

1.4 Objectives and summary of this work

The goal of this work, which is targeted at POC applications, is to maintain system-simplicity while improving the system performance for biosensing. Probing the phase response of resonant dielectric nanostructures instead of the intensity has several predictable advantages. First, sharp phase changes occur at the resonance wavelength, where the electric field enhancement is maximal. Moreover, phase noise of coherent light sources can be orders of magnitude lower compared to amplitude noise, which becomes especially relevant when applying inherently stable common-path interferometry. Finally, extracting information from an interferogram allows to apply a simple and intensity-noise independent read-out based on Fourier analysis.

The work presented here shows that these predicted advantages appear valid and the LOD of photonic sensors based on dielectric nanostructures can be reduced with a common-path interferometric resonance read-out without increasing the complexity of the sensor system compared to traditional spectral read-out approaches.

In summary, following the phase response simulation of typical GMR modes in one-dimensional silicon nitride gratings, I identified an approach to common-path interferometry by referencing the phase response of two orthogonally polarised resonant modes. This allowed me to design and fabricate the corresponding nanostructures to achieve spectrally overlapping resonance peaks in reflection such that both modes can be excited with a single wavelength on the same sensor. To keep the phase extraction as simple and stable as possible, I realised a polarisation interferometer using a single Wollaston prism, which generates a small divergence angle between the orthogonally polarised beams and creates a spatial interferogram in the camera plane, where these beams partially overlap. The relative phase change of the modes upon biomolecular binding on the sensor surface can be monitored over time, which I demonstrated in this work with bulk refractive index sensing as well as the proof-of-principle detection of procalcitonin [49].

In parallel to this project line, which is described in the main body of this thesis, my contributions further relate to theoretical investigations [50], surface functionalisation [51], data processing techniques [52], alternative photonic technologies based on dielectric nanoholes [53] and setup miniaturisation, some of which I will briefly describe in the outlook section of this thesis.

2 Theory

2.1 Basics of photonics

2.1.1 Dielectric materials and the concept of refractive index

Dielectrics are insulating materials which do not conduct electricity. If a dielectric material is placed in an electric field, the electrons of the material do not move freely. Instead, a relative displacement between atoms and electrons is induced [54]. The strength of this displacement depends on the material itself and on the electric field. In the case of a source-free medium and small electric fields, the relationship between displacement and electric field can be approximated as linear [55]:

$$\vec{D}(\vec{r}) = \varepsilon_0 \varepsilon(\vec{r}) \vec{E}(\vec{r}) \tag{1}$$

Here, $\vec{D}$ is the displacement field, ε_0 is the vacuum permittivity, $\vec{E}$ the electric field and ε the relative permittivity (also called dielectric constant) which depends on the material properties. The refractive index of such a non-magnetic material is defined as:

$$n = \sqrt{\varepsilon} \qquad\qquad n = \frac{c_0}{c} \tag{2}$$

and is quantifying how much higher the speed of light c_0 is in free space compared to its speed c in the medium. A high refractive index corresponds to a stronger displacement according to Equation (1) and a strong displacement in turn corresponds to slower light.

Equation (1) neglects not only the non-linear influence of higher order electric field components, but it also simplifies the material by assuming that it is macroscopic and isotropic and that it has no material dispersion ($\varepsilon(\vec{r},\omega) = \varepsilon(\vec{r})$). In the case of transparent materials, the losses are assumed to be zero and the generally complex relative permittivity is real and positive. All of these simplifications are valid in the following work.

2.1.2 Maxwell's equations

An electromagnetic field is described by two vector fields, the electric field $\vec{E}$ and the magnetic field $\vec{H}$. Maxwell's equations represent a unified classical theory of electricity and magnetism, including optical frequencies. With the same simplifications in place as already discussed for equation (1), and also assuming that the relative magnetic permeability $\mu(\vec{r}) \approxeq 1$ for dielectrics, the Maxwell equations take the following form [55, 56]:

$$\nabla \cdot \vec{H}(\vec{r},t) = 0 \qquad \nabla \times \vec{E} + \mu_0 \frac{\partial \vec{H}(\vec{r},t)}{\partial t} = 0 \tag{3}$$

$$\nabla \cdot [\varepsilon(\vec{r})\vec{E}(\vec{r},t)] = 0 \qquad \nabla \times \vec{H}(\vec{r},t) - \varepsilon_0 \varepsilon(\vec{r}) \frac{\partial \vec{E}(\vec{r},t)}{\partial t} = 0$$

with the electric and magnetic fields $\vec{E}$ and $\vec{H}$, the vacuum permeability μ_0 and vacuum permittivity ε_0. For dielectrics $\varepsilon = n^2$ (Eq. 2), meaning that when the magnetic permeability is one, the refractive index n only depends on the permittivity ε and the magnetic field $\vec{H}$ relates to the magnetic induction field $\vec{B}$ as $\vec{B} = \mu_0 \vec{H}$.

Any complex solution of these equations can be obtained by a combination of sinusoidally varying harmonic modes. The reason for the principle of superposition, meaning that if two electromagnetic fields are each solutions of Maxwell's equations then their sum is a solution as well, lies in their linearity.

There are many conclusions that can be drawn from these equations so here I will focus only on the lessons that will be most important in this work later on. The fields $\vec{E}$ and

$\vec{H}$ are each transverse to the direction of propagation (perpendicular to the wave vector $\vec{k}$) for any electromagnetic wave. Further, $\vec{E}$ is perpendicular to $\vec{H}$ and $|\vec{E}| = c|\vec{B}|$ with c being the speed of light in vacuum.

2.1.3 Evanescent electromagnetic fields

To give an intuitive introduction to the theory of nanophotonics, I want to start with a simple example of what forms, as mentioned in the introduction, the basis of photonic sensing in general: evanescent waves.

The following form of the wave equation, which can be derived from Maxwell's equations (Eq. 3), describes mathematically how a plane wave behaves in a homogeneous medium:

$$\left(\frac{\delta^2}{\delta\vec{r}^2} - \frac{\varepsilon}{c^2}\frac{\delta^2}{\delta t^2}\right)\vec{E}(\vec{r},t) = 0. \tag{4}$$

It can be easily verified that plane waves of the form $\vec{E}(\vec{r},t) = \vec{E}_0 e^{i(\vec{k}\vec{r}-\omega t)}$ are solutions of the above equation. They correspond to transverse waves with points of constant phase being aligned in planes that are orthogonal to the propagation direction, along the orientation of the wave vector $\vec{k}$.

Imagine that this plane wave encounters a discontinuity in the medium, e.g. an interface between two media with different dielectric constants ε (Fig. 6). This means that one solution of the wave equation is now valid on one side of the interface and another solution is valid on the other side. To quantitatively answer the question of what happens at the interface, the wave equation needs to be solved by taking the corresponding boundary condition into account.

Specifically, the parallel component $k_{||}$ of the wave vector $\vec{k}$ needs to be conserved (equal on both sides) due to the continuous translational symmetry along the interface, which leads to the well known Snell's law $\sqrt{\varepsilon_1} sin\theta_1 = \sqrt{\varepsilon_2} sin\theta_2$. For angles below a

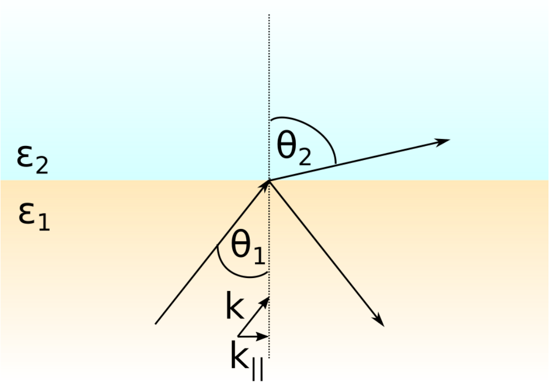

Figure 6: Interface between two dielectrics with $\varepsilon_1 > \varepsilon_2$. Light is incident with angle θ_1 and refracted with angle θ_2. Translational symmetry demands that the parallel component $k_{||}$ of the wave vector $\vec{k}$ is conserved.

critical angle of total internal reflection ($\theta_c = sin^{-1}(\sqrt{\varepsilon_2})/\sqrt{\varepsilon_1}$ if $\varepsilon_2 < \varepsilon_1$), the spectrum of possible solutions is continuous for frequencies that are larger than $ck_{||}$ (above the light line [57]). Solutions which are below the light line (lower frequencies compared to solutions in air), the vertical wave vector component becomes imaginary:

$$k_\perp = \pm i\sqrt{k_{||}^2 - \omega^2/c^2}. \tag{5}$$

The corresponding evanescent solutions are localised in the vicinity of the higher index medium and decay exponentially away from the interface into the lower index medium (e.g. air) since solutions of the Maxwell's equations with imaginary wavenumber do not represent propagating waves.

This happens because the light does not 'see' an interface as a plane but rather it is reflected partially from within the volume of the second medium. The depth from which the light is reflected depends on the medium properties and the wavelength of the light. Light of shorter wavelength will create a shorter evanescent tail than light of longer wavelengths. The higher the refractive index contrast, the shorter the evanescent

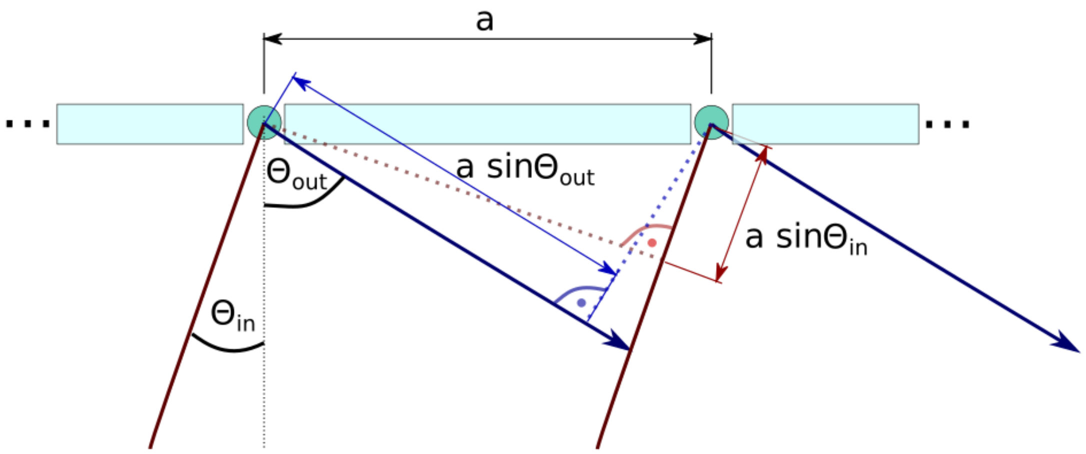

Figure 7: A diffraction grating can be seen as the interaction between waves scattered from adjacent point scatterers (grating grooves with distance a). The optical path difference between the waves scattered from adjascent grooves is $a \cdot sin\theta_{out} - a \cdot sin\theta_{in}$. Figure loosely adapted from [54].

tail.

2.1.4 Diffraction gratings

To understand the behaviour of light interacting with a diffraction grating (e.g. equally spaced ridges in glass) it helps to imagine each point of the ridge-air interface as scatterer and, as such, mathematically as a point-source.

Diffraction is the result of interference, or one could also say that diffraction is interference between waves from many sources. At normal incidence of light from a source far enough away to approximate it as a plane wave arriving at the grating, the phase in each scatterer is expected to be the same. While, more generally, if the incidence beam forms an angle with the grating, the phase at each scatterer will be different. The phase difference between two adjacent scatterers is (compare to Figure 7):

$$\Phi = \frac{2\pi a}{\lambda}(sin\theta_{out} - sin\theta_{in}). \tag{6}$$

From Equation (6), it is possible to deduce several aspects of diffraction gratings. First, the phase difference is 2π (m = 0) only if $sin\theta_{out} = sin\theta_{in}$ with $a < \lambda$. This means that for sub-wavelength gratings, no higher order diffraction orders exist and the direction at which the zeroth order leaves the grating is equal to the direction of the incident beam.

Further, the well-known grating equation predicts the angles at which the respective diffraction orders m (constructive interference) occur:

$$\theta_m = arcsin\left(sin\theta_{in} - \frac{m\lambda}{a}\right). \tag{7}$$

Here, I would like to mention Richard Feynman's book on Quantum Electrodynamics [58], which introduces a different approach of describing the behaviour of diffraction gratings based on photons and probabilities, which is an enjoyable read but not included here for consistency reasons.

2.1.5 Waveguides

If we assume a dielectric waveguide of rectangular shape (see Fig. 8) and an electric field propagating in x-direction while oscillating in y-direction, Maxwell's equations tell us that there can be no tangential field component at the boundaries of the waveguide. Since the field is oscillating in y-direction, the field component is perpendicular to the boundary in y-direction, while the field has to be zero at the z-boundary [54]. This is the case if integer multiples m of half a wave fit into the waveguide height h in z-direction for a given wavelength, which means if:

$$k_z h = m\pi. \tag{8}$$

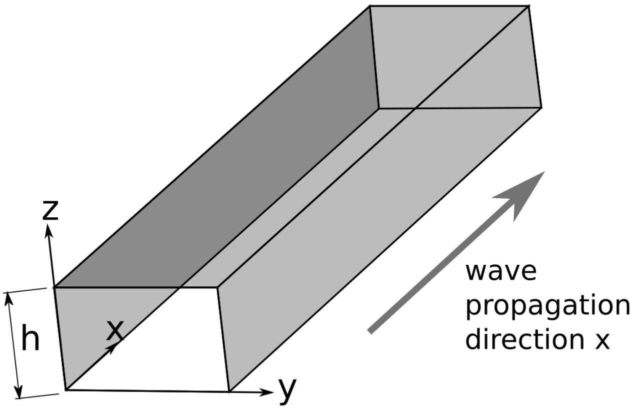

Figure 8: Waveguide schematic with the refractive index of the waveguide material being higher than that of the surrounding medium ($n_{guide} > n_{cladding}$). Rectangular shape of the waveguide with height h. The width in y-direction is not relevant for the considerations since the E-field has only one component in y-direction: $\vec{E} = (0, E_y, 0)$. In fact, the waveguide can be assumed to be infinitely extended in y and x.

To satisfy the wave equation (see Eq. (4)), with $\vec{E}$ = (0, E_y, 0), the following further condition needs to be met:

$$k_x^2 + k_z^2 - \frac{\omega^2}{c^2} = 0 \quad \Rightarrow \quad k_x = \pm\sqrt{\left(\frac{\omega}{c}\right)^2 - \left(\frac{m\pi}{h}\right)^2}, \tag{9}$$

where k_z is defined by Eq. (8) and $\frac{\omega}{c} = \frac{2\pi}{\lambda_0}$ with the vacuum wavelength λ_0. Note that k_x can have a positive or negative sign according to Eq. (9) corresponding to forward or backward propagating waves respectively.

Waves of the following exemplary form satisfy these requirements and can as such be called the possible modes of the waveguide:

$$E_y = E_0 \cdot e^{i(\omega t - k_x x)} \cdot sin(k_z z). \tag{10}$$

Combining the above equations gives an effective wavelength of the guided mode λ_g = $\frac{2\pi}{k_x}$ which depends on the height of the waveguide as follows:

$$\lambda_g = \frac{\lambda_0}{\sqrt{1-(\frac{m\lambda_0}{2h})^2}}. \tag{11}$$

The speed at which a point of constant phase of the wave propagates along the waveguide is the phase velocity v_{ph} while the envelope moves with group a velocity v_{gr}, which is lower than c:

$$v_{ph} = \frac{\omega}{k_x} \qquad v_{gr} = \frac{d\omega}{dk_x}. \tag{12}$$

The energy which is transported by an electromagnetic wave can be calculated using the Poynting's theorem, which describes the rate of the directional field energy movement or in other words the "time-average flux of electromagnetic energy" [57]:

$$\vec{S} = \frac{1}{2} Re\left[\vec{E}^* \times \vec{H}\right]. \tag{13}$$

These equations are the basis of the simulations which will be introduced later.

See reference [59] for a detailed general theoretical discussion on coupled mode theory with respect to slab dielectric waveguides. The considerations above only apply to the TE mode with its E_y (transverse electric) component, while the TM mode (transverse magnetic) will have the two E-field components E_x and E_z. For a full derivation of TE and TM modes see reference [60].

2.2 Guided-mode resonances

The previous considerations of diffraction and waveguides are meant to culminate in the following section on guided-mode resonances (GMR). GMRs originate from a combination of diffraction and wave-guiding. Conventional grating theory from the respective Section 2.1.4 above cannot explain every aspect of light interacting with gratings, in particular when the grating period is comparable in size to the wavelength. In 1902, Wood made the surprising observation of strong intensity variations in light diffracted by a grating in a very narrow range of wavelengths and called them ‘anomalies’ [61]. The anomalies occur when leaky surface waves in the grating are resonantly excited by the mechanism of phase matching between the incident plane wave and diffracted light, which, in these special cases of high diffraction angles, is guided in the grating layer.

The corresponding destructive interference between the zeroth diffraction order and the first can, under specific circumstances, lead to 100% reflectance at a certain wavelength. For the first diffraction order to be guided in the grating layer, the grating-period has to be in the range of the excitation wavelengths. This condition can be qualitatively predicted from the combination of the diffraction grating equation (Eq. (7)) and the critical angle of total internal reflection.

The resulting standing waves inside the slab can be described as a superposition of waves propagating in +z and -z. Similar to a Fabry-Perot resonance in a uniform slab, the transverse phase shift for every propagating component of a GMR mode is a multiple of 2π after a round trip in the non-uniform slab. The difference to the FP-resonance is the periodicity of the refractive index in x-direction, which leads to the coupling of multiple propagating components [62]. Guided-mode resonances are guided modes above the light line which can couple to the radiation modes due to the index perturbation of the waveguide and therefore have a limited lifetime.

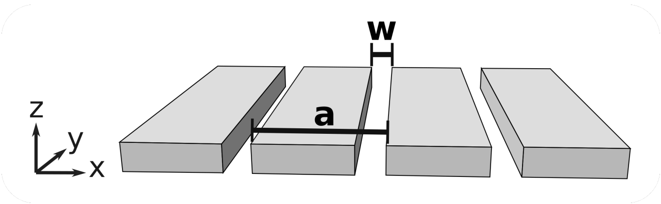

Figure 9: One dimensional grating with discrete translational symmetry, period a and groove width w. The refractive index of the grating surrounding medium is lower than the effective index of the grating layer.

2.2.1 Bloch's theorem

In an homogeneous medium, the solutions of Maxwell's equations are plane waves, as discussed in 2.1.3. In periodically varying media, the modes become travelling modes modulated by standing waves, which are called Bloch modes [56]. For example, the waveguide grating in Figure 9 has a one-dimensional periodic permittivity variation $\varepsilon(x) = \varepsilon(x \pm a)$, which, in addition to the restriction of k_z (Eq. 8), imposes a discretization of the k_x component.

The possible modes in such a structure (Fig. 9) are travelling plane waves modulated by a periodic function with the same periodicity as the lattice vector $\vec{g}$. The solutions of wave propagation in such periodic media can be acquired by solving the Helmholtz equations with periodic ε(x), which results in the following general solutions called *Bloch modes* [56]:

$$U(x) = f_k(x)e^{-ikx}, \tag{14}$$

where U represents the relevant field components of E or H and $f_k(x)$ is a period function with period a. Here, k is the wavenumber and the Bloch waves can be expressed as superposition of plane waves e^{-imgx} with the fundamental spatial frequency g of the grating and the harmonics mg such that two Bloch wavenumbers k and k' = k + g are the same [56]:

$$g = \frac{2\pi}{a}. \tag{15}$$

The vector $\vec{g} = \frac{2\pi}{a}\vec{e}_x$ is called the reciprocal lattice vector [57] with the unit vector in x-direction $\vec{e}_x$, which is the direction of periodicity in this example (Fig. 9).

2.2.2 Photonic band structure

As is evident from Figure 10, the wavelength at which light resonantly couples to the waveguide, obtaining high reflectance, depends on the angle of incidence θ. Because of the Bragg condition discussed above, the relationship between incidence angle and resonance wavelength is [63]:

$$\frac{2\pi}{\lambda} sin\theta = \pm\frac{2\pi n_{\text{eff}}}{\lambda} \pm m\frac{2\pi}{a}, \tag{16}$$

where n_{eff} is the effective refractive index of the waveguide grating. The ± signs (as discussed for the waveguide in Eq. (9)) corresponds to forward and backward propagating modes.

In Figure 10, two modes are visible in the dispersion diagram. When looking at Equation (16) and Figure 10 together, it becomes understandable how these two modes are a result of counter-propagating waves and their respective different resonance conditions. For every angle θ, the longer wavelength corresponds to one mode and the shorter wavelength to the respective counter-propagating mode. The Bragg-scattering between these counter-propagating modes results in standing waves, as discussed, which are modulated with the period of the grating. The structure supports two standing waves with different energy (corresponding to different wavelengths as visible in Fig. 10) and opposite symmetry of the field confinement, which will be discussed further below. The wavelength region in-between those two opposite modes is a region for which the counter-propagating modes interfere destructively, which is called photonic bandgap. The odd mode at the Γ-point ($\theta = 0$) cannot couple to the continuum

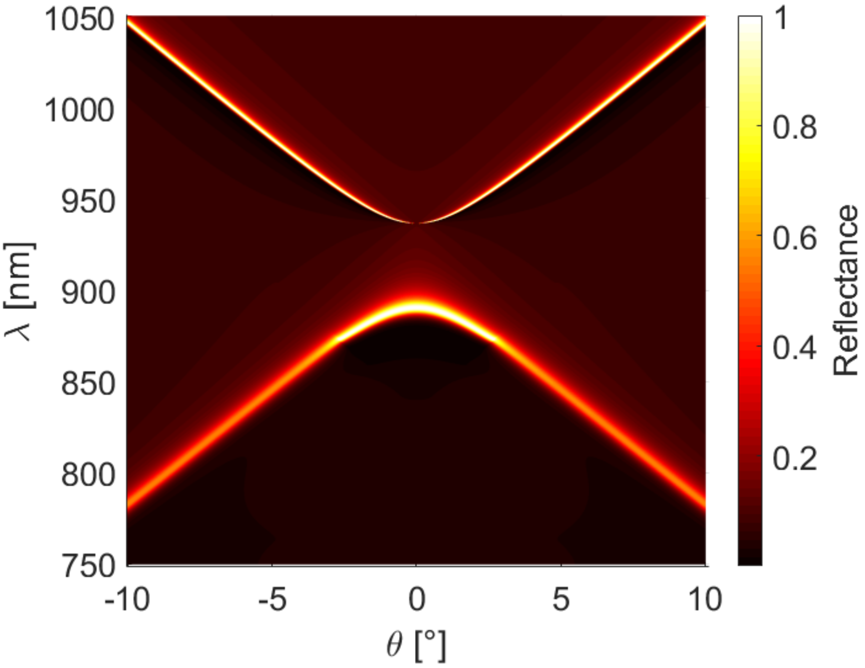

Figure 10: Simulated dispersion relation of GMR TE-mode. The structure assumed for this S^4-simulation is a one dimensional Si_3N_4-grating with x-y- infinity and height of 150 nm. For this example, there exists up-down mirror symmetry with a SiO_2 substrate and superstrate.

because of the symmetry mismatch between the mode's field confinement and the continuum [64].

2.2.3 Fano resonances

When non-resonant scattering does not occur (no Fabry-Perot background), the shape of the resonance peak (line shape) is symmetric and mathematically represented by a Lorentzian (discrete state in Fig. 11). This is generally not the case for GMRs.

The interference between a discrete state and a continuum is generally the reason for asymmetric Fano line shapes, where the first and famous example are the Rydberg spectral atomic lines. Their asymmetric shape was explained by Ugo Fano in terms of interference effects [65] and his theory can be used to understand the origin of Fano line shapes across very different areas of physics [66]. When two oscillators are coupled, at a certain frequency close to the resonance frequency of one single oscillator (corresponding to a π phase jump), the two oscillators will be out of phase and cancel each-other due to destructive interference [67].

The asymmetric line-shape of the special cases of resonantly reflected light from a diffraction grating [61] can be understood as the result of interference between the guided mode and the incident plane wave, which experiences slow spectral variations, due to a Fabry-Perot effect, as 'continuum'. This coupling of a guided mode to the broad continuum leads to the leaky nature of the resonance and the specifics of this interference process also give rise to the asymmetric Fano-shape of the resonance peaks. Depending on the thickness of the slab, the dip of the Fano peak can occur on the left or the right of the resonance wavelength (Fig. 12). For a higher effective slab index, the continuum of the Fabry Perot can also reach around 50 % reflectance which results in symmetric dip and peak reflectance values. The resonance wavelength, and so the highest field enhancement, in those cases is no longer close to the peak in reflection but between dip and peak.

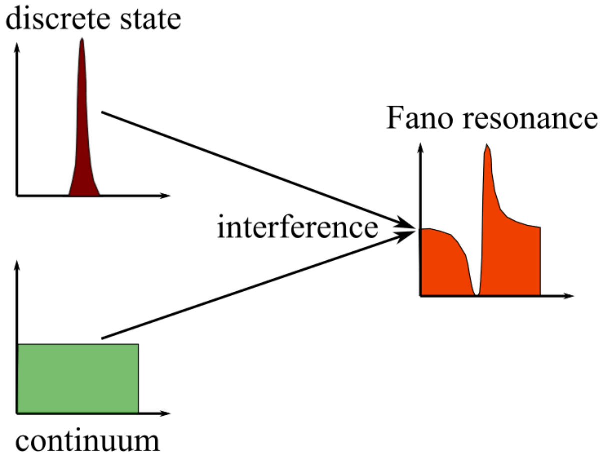

Figure 11: Schematic of a Fano resonance as a result of the interference between the radiative continuum (Fabry-Perot (FP) effect) and a discrete state of the waveguide. Due to the phase variation of the discrete state with respect to the wavelength (x-axis), and the resulting relative change in phase compared to the continuum, destructive interference leads to a dip on one side of the resonance. On which side the destructive interference is observed depends on the thickness of the waveguide layer because the FP effect determines the relative phase difference between discrete state and continuum.

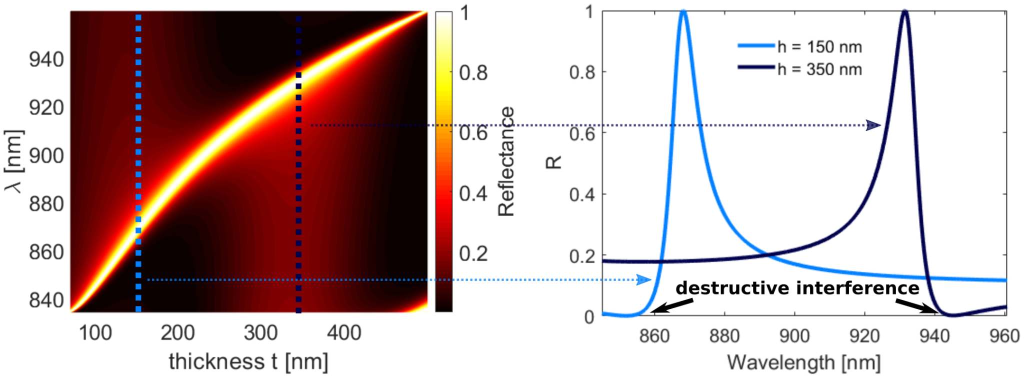

Figure 12: Dependence of Fano line shape of TE GMR mode on grating layer thickness. The asymmetry of the resonance peak depends on the thickness because the Fabry-Perot effect in the grating layer depends on it and the resonance peak is a result of interference between the resonance and the FP. The dip in the Fano line shape occurs when there is complete destructive interference between the resonance and the FP, which means when the phase difference is π and the intenisties are the same.

2.2.4 Phase response of Fano resonances

To analyse the phase response of a typical GMR Fano resonance, first we can consider the case of a resonance where the background reflectance of the slab is zero. The shape of a GMR peak in reflection is then described by a Lorentzian. This is schematically visualised in Figure 11 where the discrete state remains a discrete state if the continuum is zero. The corresponding phase of a Lorentzian peak is characterised by a typical π shift around the resonance wavelength. In this case, the phase and therefore magnitude have a symmetric distribution around the resonance wavelength, which coincides with the peak in reflection. This can, for example, be shown using coupled mode theory applied to a photonic crystal slab (adapted for zero slab reflectivity and zero losses from SI of [68]).

For a non-zero continuum, the response of the continuum and the resonance response are superimposed. The phase relation between resonance and continuum is the reason for the typical asymmetric resonance peaks and the total phase of the corresponding complex amplitude deviates from the π response of the isolated resonance without continuum interactions.

This behaviour is here illustrated by simulated phase maps showing the phase response of a GMR in dependence of the slab thickness (Fig. 13). The slab thickness determines the phase and magnitude of the continuum. Therefore, for certain thicknesses the Fabry-Perot reflectance value is zero, while the continuum is non-zero for thicknesses that are not in the minimum of the Fabry-Perot resonance in the slab.

2.2.5 Mode confinement

As a consequence of the resonance, an evanescent field enhancement is observed at the surface [66]. Compared to the purely guided modes of a uniform slab (non-leaky modes), the electromagnetic field enhancement inside the perturbed slab in the case of a GMR is lower, due to the resonant scattering, but still significant (see Fig. 14).

The evanescent field decays exponentially from the surface of the Si_3N_4 and the penetration depth d is defined by the distance z at which the initial field falls by a factor 1/e:

$$E(z) = E(0)e^{-\frac{z}{d}}. \tag{17}$$

For the GMR TM mode in Figure 14, d $\approx$ 200 nm.

2.2.6 Resonance regime dependence on grating parameters

In addition to the theoretical resonance conditions of GMRs, a more intuitive understanding can be gained when visualising the dependence of the resonance condition

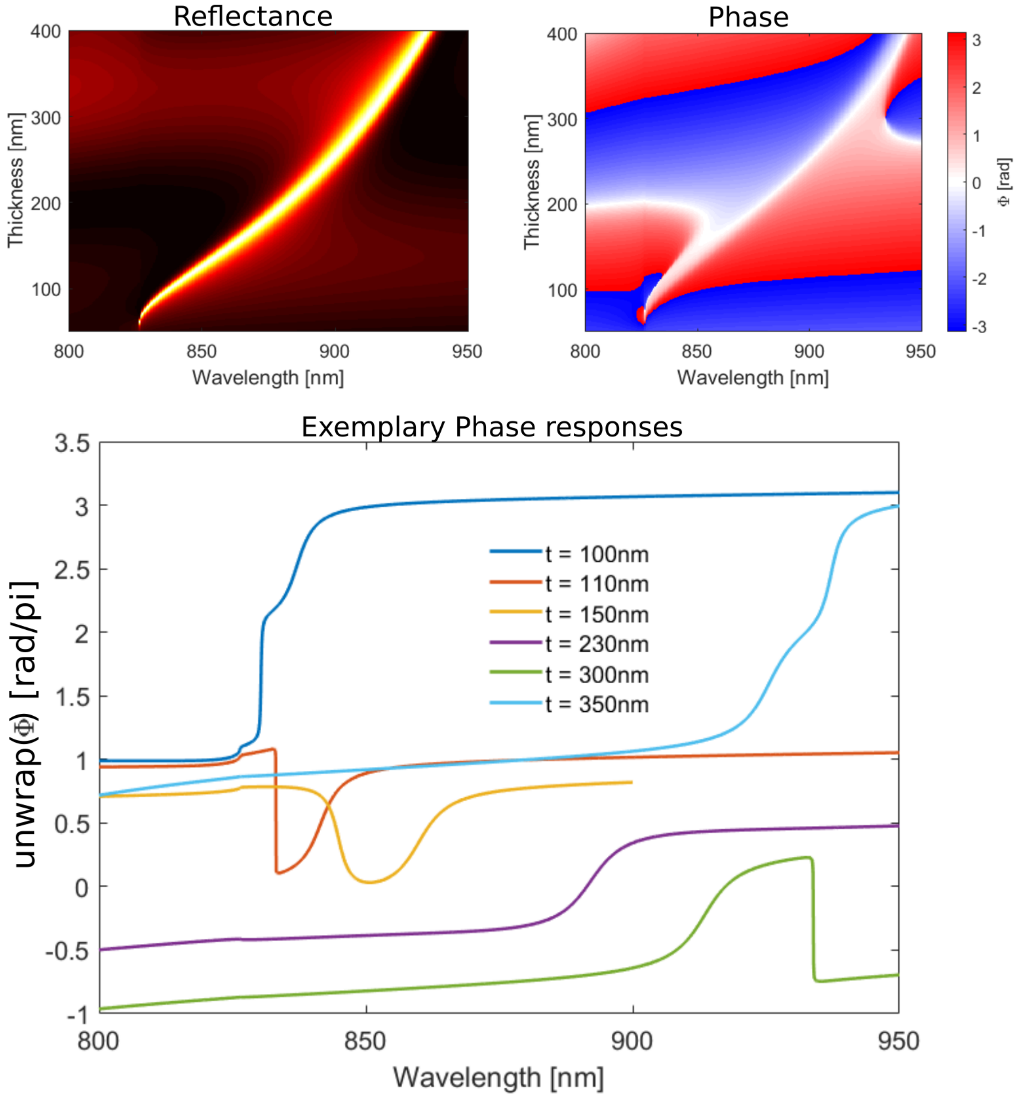

Figure 13: Top: RCWA simulations of reflectance and phase response of GMR (TE mode) depending on slab thickness. Bottom: Selected exemplary phase responses for specific slab thicknesses in the range between 100 nm and 350 nm.

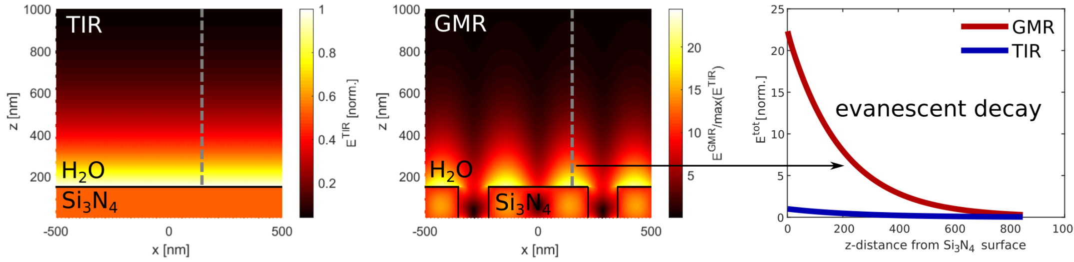

Figure 14: Evanescent field in the case of total internal reflection (TIR) from a Si_3N_4-H_2O interface (left) and in the case of a GMR mode in a Si_3N_4 grating on a SiO_2 substrate with a H_2O-cover (middle). The figure on the right shows the evanescent decay from the surface away in z-direction, indicated by the grey dotted lines in the left and middle panel.

on the grating parameters such as the slab thickness, grating period, refractive index of the grating material and filling factor based on simulations (see Fig. 15). These simulations show the operating regime of the structure, which is based on two main conditions, one related to diffraction and one to wave-guiding. First, the period of the grating has to be near the wavelength of the light, specifically, smaller than the wavelength in the medium of incidence, but larger than the wavelength in the grating layer. This ensures that the structure is above the deep-sub-wavelength regime, where the light sees the structure as slab and is not diffracted, but also that the diffraction angle is high enough to potentially couple the first diffraction order into the slab (compare to Fig. 15 A and B). This leads to the second requirement, which is that the effective index of the grating (waveguide) has to be higher than the indices of the surrounding media and thick enough to support a guided mode (compare to Fig. 15 C and D).

Figure 15 B shows a linear dependence of the resonance wavelength on the grating period a, which can be predicted from the grating equation (Eq. (7)). The resonance dependence on the filling factor FF (Fig. 15 D) as well as the refractive index of the grating material (Fig. 15 C) show the requirement of having a high enough effective slab index for index guiding. I will refer back to these simulations throughout the thesis, to discuss certain details at appropriate points.

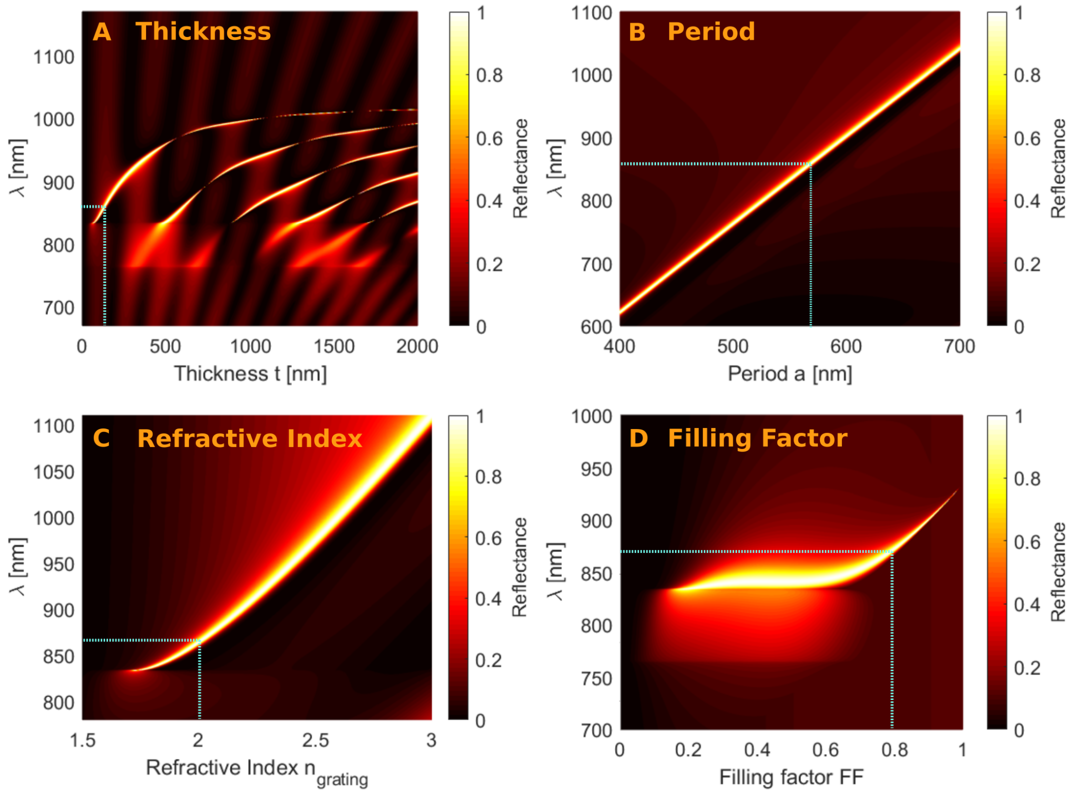

Figure 15: Resonance maps in dependence of grating parameters illustrate the limits of guided-mode resonance excitation in parameter space. The dashed bright blue lines indicate the usual point of operation, meaning the approximate parameter combination which is used for this work. The 4 maps show the dependence on **A** the grating slab thickness t, **B** the grating period a, **C** the refractive index of the dielectric grating material (not effective index) and **D** the filling factor FF of the grating ((a - w)/a see Fig. 9). The parameters, which are kept constant while one parameter is swept, are a = 575 nm, FF = 78%, t = 150 nm and $n_{\text{grating}} = 2.02$.

2.2.7 Bound states in the continuum - terminology

To further enhance understanding, and because this terminology is necessary to understand Section 6.4 in the outlook, I want to explain the origins of ‘dark modes’ also called bound states in the continuum (BIC) in dielectric grating structures and how this terminology fits into the theory of GMR.

BICs are states which are localised even though they occur in a continuum of radiating waves which usually carry energy away [69]. In general, a BIC is a perfectly confined mode without any radiation [70] but photonic BIC do not all have the same fundamental origin. Their classification in the literature is rather based on their common characteristics, the most defining of which is a theoretically infinite lifetime, which is symmetrically approached around singularities in k-space. In the proximity of the singularities, where the coupling to the continuum is not perfectly inhibited corresponding to the experimental reality, the lifetime of these so-called ‘Quasi-BIC’ modes is still arbitrarily high in theory. The physics of Quasi-BIC and GMR modes in dielectric nanostructures is not fundamentally different. Quasi-BIC and GMR are both resonances due to the coupling of guided modes to the radiating continuum and both show the characteristic Fano-shape of their resonance peaks. Photonic Quasi-BIC in resonant dielectric nanostructures could as such be classified as a subtype of GMR, which are characterised by their convergence to complete inhibition or prohibition of coupling at specific points e.g. the Γ-point in the case of symmetry protected BIC (upper band in Fig. 10) or at a $k \neq 0$ in the case of accidental or resonance-trapped BIC [70].

2.3 Figures of merit for biosensing

Since the necessary theoretical concepts for understanding the origin of Fano-shaped resonance peaks as well as the accompanying evanescent field confinement have been explained above, it is now possible to define the relevant figures-of-merit (FOM) for sensing. Note that these concepts are not all relevant for the phase-sensitive resonance read-out but they are nevertheless introduced to explain the most common read-out methods.

2.3.1 Quality factor and phase sensitivity

The quality factor (Q-factor) of a resonance is usually determined by [38]:

$$Q = \frac{\lambda_{\mathrm{peak}}}{\delta\lambda}, \tag{18}$$

where λ_{peak} is the resonance wavelength at the maximal intensity of the resonance peak and $\delta\lambda$ is the full width at half maximum (FWHM) of the peak. The origin of this definition lies in the basic theory of oscillators. The radiative energy loss of a damped oscillator leads to a 1/e decay in the oscillation amplitude. The Fourier transform of this damped oscillation is the typical Lorentz intensity profile where the decay rate correponds to the FWHM of the profile, and so the lifetime of the resonance is proportional to the defined Q-factor.

In the case of a Fano-shaped resonance peak, an alternative definition is based on the difference in wavelength between dip and peak of the resonance rather than the FWHM [71]:

$$Q_{fano} = \frac{\lambda_{\mathrm{peak}}}{\delta\lambda_{\mathrm{fano}}} = \frac{\lambda_{\mathrm{peak}}}{|\lambda_{\mathrm{peak}} - \lambda_{\mathrm{dip}}|}. \tag{19}$$

A peak with higher Q-factor can be tracked with higher accuracy than a peak with lower Q-factor with the same signal-to-noise-ratio (SNR) because for the same change in refractive index, the intensity will change more for a high-Q resonance than for a low-Q resonance with the same sensitivity. This is valid for a photonic sensor based on

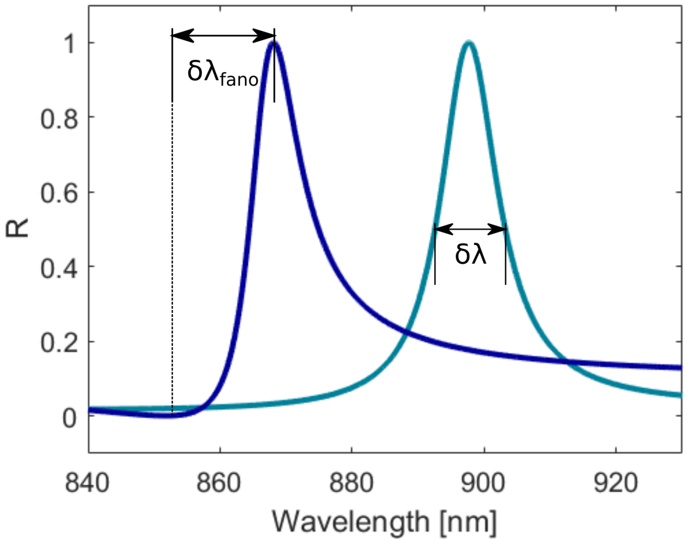

Figure 16: Lineiwdth definition depending on peak shape. $\delta\lambda$ for a symmetric line shape is the full-width-at-half-maximum (FWHM) while $\delta\lambda_{\text{fano}}$ depends on the positions of the peak and the dip of the resonance line shape.

intensity/spectral read-out, assuming that the resolution is not limited by the read-out system (e.g. a spectrometer).

So while the Q-factor determines the accuracy of the read-out if the resonance peak is tracked, e.g. with a spectrometer, with alternative read-outs the Q-factor and the sensitivity are directly correlated. For example, if spectral information is transformed into spatial information by using e.g. a chirped GMR sensor and a single excitation wavelength [42], then a higher Q-factor of the resonance allows to reduce the range of the chirped parameter (e.g. grating period variation) and the spatial signal will move to a higher degree in space when the index is altered, meaning the read-out-sensitivity (not the intrinsic sensitivity) is higher. Similarly, if the phase response is measured using a single excitation wavelength, a sharp phase curve and a high Q-factor are correlated such that resonances with higher Q-factors correspond to stronger phase responses upon index alterations.

2.3.2 Bulk sensitivity

The bulk sensitivity S is the wavelength shift response $\Delta\lambda$ to a change in bulk refractive index Δn. S is expressed in wavelength shift per refractive index unit (RIU), i.e. the extrapolated $\Delta\lambda$ for $\Delta n = 1$, and is determined by:

$$S = \frac{\Delta\lambda}{\Delta n}. \tag{20}$$

S has to be extrapolated because the change in wavelength when changing the bulk refractive index in the whole superstrate around the surface of the nanostructure is not linear in the range of $\Delta n = 1$ (see simulation in Fig. 17, left). What is usually considered the sensitivity is therefore determined by changing the refractive index slightly in a range where the wavelength response can be approximated as being linear (e.g. from n = 1.33 to n = 1.34, see Fig. 17, right) and in which biosensing responses are to be expected. The wavelength response (e.g. $\Delta\lambda$ = 1.70 nm) is then extrapolated to RIU and the sensitivity is expressed in nm per RIU (e.g. 170 nm RIU^{-1}).

The possible range of sensor response to index change is called dynamic range of the sensor and in this case I mean the *photonic* dynamic range, where usually only the linear response range is considered. The biosensing dynamic range also depends on the surface chemistry, which will be discussed in more detail later.

2.3.3 Surface sensitivity

The ability to distinguish between bulk and surface sensitivity is important for a useful estimation of the sensing performance if the biosensor relies on an evanescent field interacting with the target, and particularly, when the target layer is much thinner than the extent of the evanescent field; in that case, the sensitivity of a refractive index sensor depends on the proportion of the evanescent field which interacts with the sample.

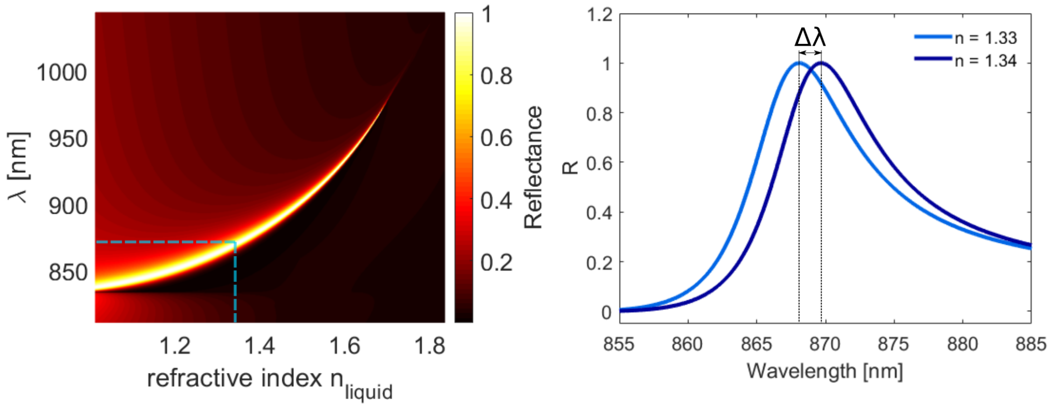

Figure 17: Left: Simulated reflectance response depending on wavelength and bulk index change of the medium surrounding the grating surface. S^4 was used for this simulation and the parameters of the grating are $n_{\text{substrate}} = 1.45$, $n_{\text{grating}} = 2.02$, grating thickness t = 150 nm, filling factor FF = 0.78, TE polarisation. Right: Wavelength shift $\Delta\lambda$ in response to refractive index alteration by $\Delta n = 0.01$.

When the refractive index of the sample changes by Δn, the corresponding wavelength change $\Delta\lambda$ is given by [72]:

$$\Delta\lambda = \eta \Delta n \frac{\lambda}{n_{eff}} \tag{21}$$

where η quantifies the overlap proportion between mode and sample, so how much of the mode's optical intensity is located in the sample (volume surrounding the surface) compared to the total optical intensity of the mode. The η of a mode, which is more extended into the liquid rather than confined in the high index material of the waveguide, is higher. Therefore, the sensitivity to refractive index changes in also higher according to Eq. (21).

One way of determining the surface sensitivity is to measure or simulate the wavelength shift upon adding a thin layer (≈10 nm) of material with n > 1.33 to the surface to mimic the effect of a surface densely covered by antibodies and target molecules. This is only an approximation to predict biosensing performance because the real surface coverage also depends on the surface chemistry, but it is a better approximation

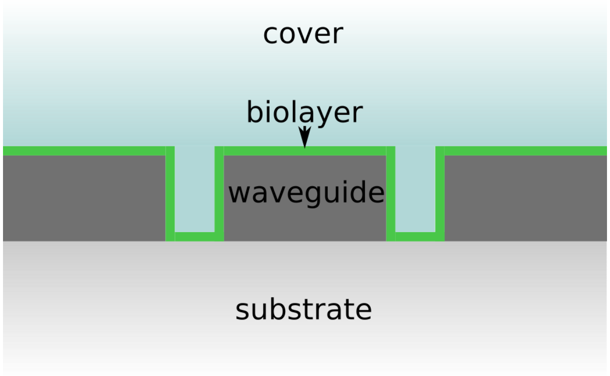

Figure 18: Surface sensitivity schematic to illustrate the principle of detecting a thin biolayer.

than the bulk LOD [53].

2.3.4 Signal-to-noise ratio

The signal-to-noise-ratio (SNR) of the resonance peak is defined as the ratio between the maximal intensity minus the minimal intensity of the resonance peak and the intensity noise.

The following equation can be used to approximate the relationship between spectral read-out noise σ and SNR of the resonance peak for all cases in which the maximum of a resonance peak is tracked spectrally [72]:

$$\sigma \approx \frac{\Delta\lambda}{4.5 \cdot SNR^{0.25}}. \tag{22}$$

This equation is derived with Monte Carlo simulations by adding a noise to a Lorentzian and repeatedly determining the generated peak position for each iteration. From there, the spectral location uncertainty is determined and this is repeated for different noise levels, which allows to retrieve the approximation found in Eq. (22). This equation illustrates the importance of SNR for photonic biosensing.

2.3.5 Limit of detection

There are different FOMs for sensing, the most common of which is the limit of detection (LOD) with respect to the bulk refractive index defined as:

$$\mathrm{LOD} = \frac{3\sigma}{S}, \tag{23}$$

where 3σ is the system noise when the refractive index is not deliberately changed and S is the bulk sensitivity, e.i. in units of $\mathrm{nm\,RIU^{-1}}$. This LOD is a ‘photonic LOD’, which depends only on the sensor system itself excluding the surface chemistry. The ‘biochemical LOD’ is defined as the smallest measurable concentration of target molecules/proteins and is usually expressed in molar or weight concentration. To achieve a better estimate of the potential ‘biochemical LOD’, the ‘photonic LOD’ is sometimes also calculated via the surface sensitivity instead of the bulk sensitivity:

$$\mathrm{LOD}_{surface} = \frac{3\sigma}{S_s}. \tag{24}$$

2.3.6 Refractive index dynamic range

The intrinsic dynamic range of a photonic sensor is defined as the range of refractive index alterations that the sensor response is able to detect. As visible in Figure 17, this range is typically considerably wider than the practically relevant range related to photonic biosensing, since the goal is typically to measure low concentrations of biomolecules. The accessible dynamic range furthermore depends on the read-out method. If the resonance peak position is tracked with a spectrometer for instance, the intrinsic dynamic range and the actual dynamic range can coincide if it is not limited by the spectrometer range. While for an intensity or phase sensitive read-out with a single wavelength for excitation, the dynamic range is limited by the FWHM of the resonance peak.

2.4 Theory of interferometry

Phase information of a single complex wave, different from the amplitude, is not accessible by the human eye or photodetectors. In order to make phase measurable, we use interference effects; the interference of the signal wave with a reference wave gives information about their mutual phase difference and how it changes over time or space. Consider two plane waves interfering; the detectable intensity I is the time average of the modulus squared of the total complex amplitude $\vec{E} = \vec{E}_1 + \vec{E}_2$ [56]:

$$I(\vec{r},t) =< |\vec{E}(\vec{r},t)|^2 >= I_1 + I_2 + < \vec{E}_1 \cdot \vec{E}_2^{\,*} > + < \vec{E}_1 \cdot \vec{E}_2^{\,*} >, \tag{25}$$

where the phase information is found in the two complex terms. This means that the measurable intensity modulation of the superposition of two waves depends on their phase difference. For two linearly and in parallel polarised plane waves of same frequency, Eq. (25) reduces to:

$$I(\vec{r}) = I_1 + I_2 + 2\sqrt{I_1 I_2} cos(\Phi) \tag{26}$$

where $\Phi = \Phi_2 - \Phi_1$ is the difference of the two phase values of the respective complex waves with their respective amplitudes (A_1, A_2) and intensities $I_1 = A_1^2$ and $I_2 = A_2^2$.

Principle of interferometry

The goal of interferometry is to determine a delay d in the optical path of one wave with respect to a reference wave. For equal intensities $I_1 = I_2 = I_0$, the phase difference and the delay are related by $\Phi = kd = \frac{2\pi d}{\lambda}$ and Equation (26) becomes:

$$I = 2I_0 \left[1 + cos\left(2\pi \frac{d}{\lambda} \right) \right]. \tag{27}$$

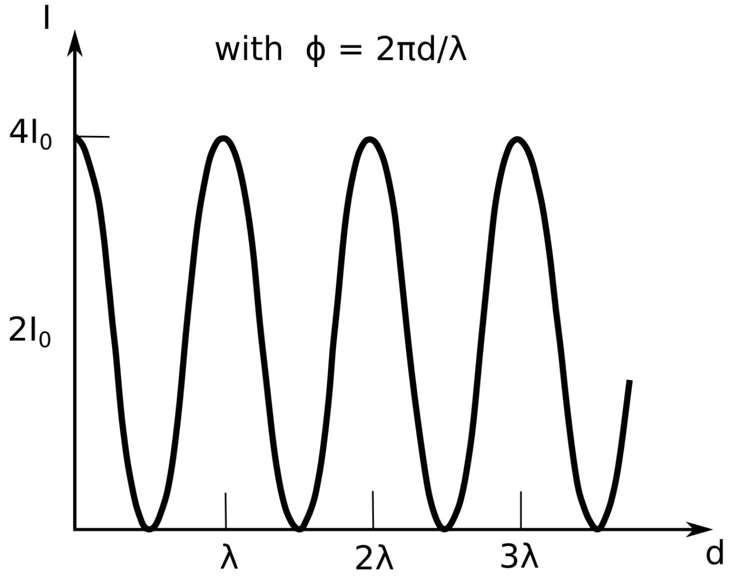

Figure 19: Intensity as a function of delay d between two plane waves according to Equation (27), adapted from [56].

A typical interferometer separates two waves to enable the difference in the optical path to be acquired and then recombines the same waves to determine d by measuring the intensity of the superposition. Constructive interference and a corresponding maximal intensity ($4I_0$) are observed when the delay is an integer multiple of λ while minimal intensity ($I = 0$) is detected for a delay of integer multiples of $\lambda/2$.

Interference of two oblique plane waves

If we look at two plane waves in the x-z-plane (Fig. 20), $\vec{E}_1$ and $\vec{E}_2$, with equal amplitudes ($A_1 = A_2 = A_0$), where one is propagating in z-direction ($\vec{E}_1 = \sqrt{I_0}e^{-ikz}$) and the other with an angle α with respect to the z-axis ($\vec{E}_2 = \sqrt{I_0}e^{-i(k\cdot cos\alpha\cdot z+k\cdot sin\alpha\cdot x)}$), then, at z = 0, the waves have a phase difference of $\Phi = k \cdot sin\alpha \cdot x$. This means that the interferogram takes the following form (see Fig. 20):

$$I = 2I_0[1 + cos(k \cdot sin\alpha \cdot x)]. \tag{28}$$

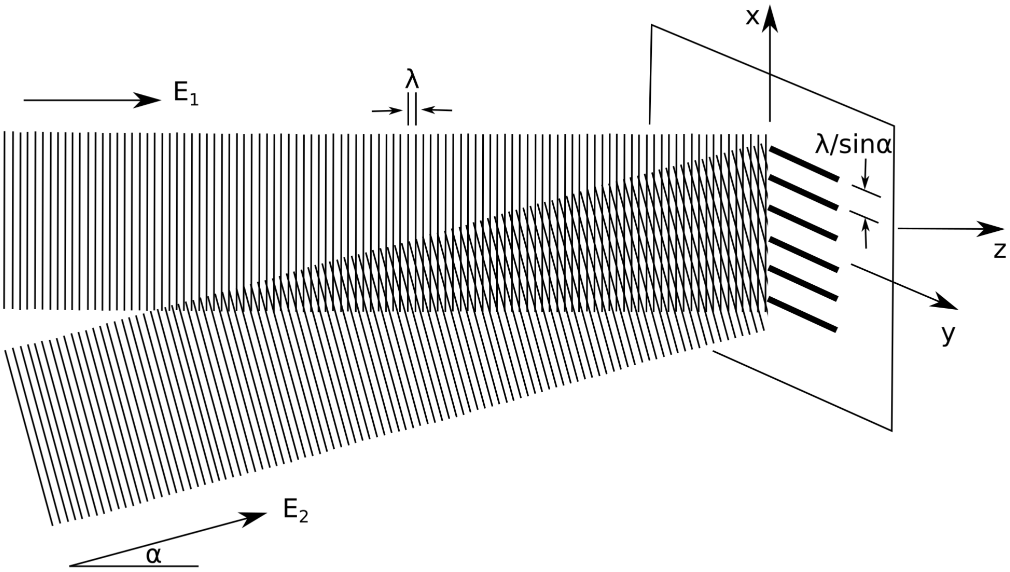

Figure 20: Interference of two oblique plane waves. Adapted from [56].

Each optical path difference (OPD) of one wavelength corresponds to a 2π phase difference and leads to the interferogram changing from one bright fringe to the next bright fringe.

3 Principle, Design, and Realisation of Resonant Phase Read-out

This section introduces the design and realisation of the relevant experimental components, mainly the optical setup, photonic nanostructures and the microfluidics, explains the motivation behind the respective designs and compares the design to the experimental data.

3.1 Resonant common-path interferometry principle

Common-path interferometry refers to approaches where the signal and the reference beam (see Section 2.4) are both directed towards the sample and travel essentially the same path. This is in contrast to, e.g., Michelson interferometers, where the initial beam is split into two beams, one of which is the signal beam interacting with the sample and the other one, travelling a different path, is the reference beam. The beams are then recombined again after the signal beam has interacted with the sample. Instead of separating signal and reference beams spatially, the relative phase difference between those beams in a common-path approach relies, for example, on polarisation dependent differences in sample interactions.

The advantage of common-path approaches [20, 73, 74], as discussed in the introduction, is that because signal and reference interact with the same optical components, mechanical instabilities affect the signal and reference beams similarly and the system is therefore more robust than a Michelson interferometer, which is relevant for a potential POC applications, since in those environments an active stabilisation is not an option.

In contrast to phase-sensitive SPR (see Section 1.3.1), light is typically mainly *resonantly* reflected from a GMR sensor and otherwise mostly transmitted, which means that reference and signal beam in a reflective common-path approach would ideally both be resonant modes because a high SNR ist achieved when signal and reference beam have ideally equal intensity (see Section 2.4).

The main idea here is to exploit the form birefringence of a one-dimensional grating in order to achieve the common-path phase read-out by exciting both TE and TM modes and measuring their phase difference over time. To generate an interferogram, I use a birefringent prism called Wollaston prism, which creates two orthogonally polarised beam-components to split the resonantly reflected light into two diverging beams, which correspond to the TE and TM mode, respectively. These components then partially overlap in the camera plane to form the interferogram which is used to visualise phase changes over time. The technicalities of this approach will be discussed in detail in the following sections. Note that the reasons for working in reflection are also discussed below.

3.2 Optical setup for common-path interferometry

There are only a few changes that need to be applied to a typical inverted GMR-setup [75] to implement the interferometric read-out (Fig. 21). The collimated output of a laser diode is focused in the back-focal-plane (BFP) of a 5X-objective to excite the GMR with collimated light. The resonantly reflected light is then directed towards the camera by a beam-splitter and the Wollaston prism splits the orthogonally polarised light. The analyser in front of the camera then enables the common components of the light to interfere when it is orientated at 45° with respect to the orthogonally polarised components.

The angle at which the orthogonally polarised beams diverge after the Wollaston prism is chosen to be 1° because it is the smallest achievable angle with available commercial prisms and it ensures that the beams have a sufficient overlap area in the camera plane to avoid the need for beam recombination for the interferogram formation. Details

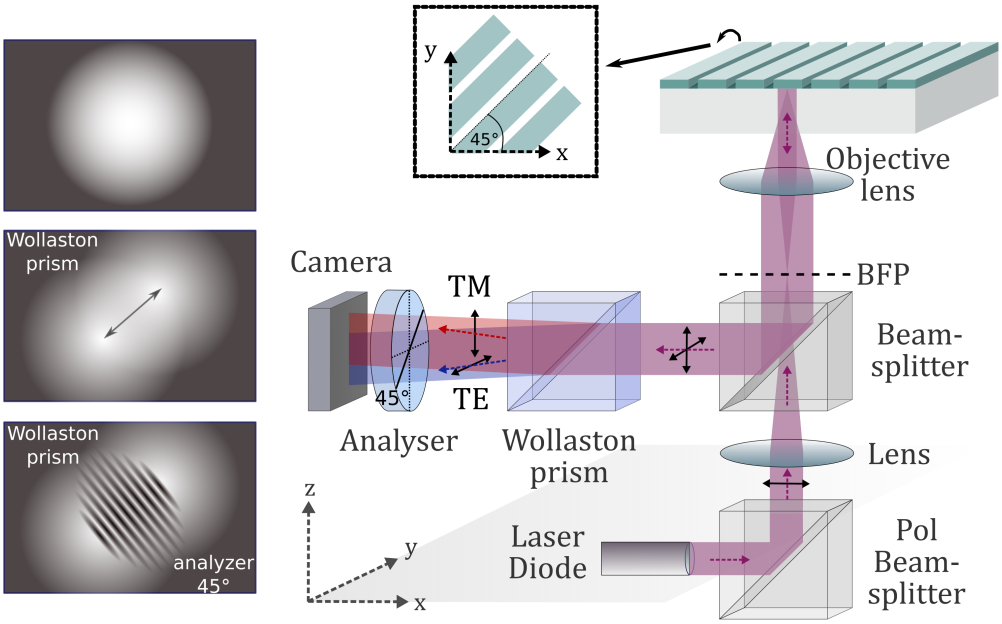

Figure 21: Schematic of the phase-sensitive detection principle. The figure shows the optical setup where the collimated output of an 855-nm laser diode is focused onto the back-focal plane (BFP) of a 5X objective after passing through a polarising beam splitter. This setup creates collimated light which excites the guided-mode resonance. The grating grooves are oriented at 45° with respect to the polarisation of the incident light, such that the TE and TM modes are equally excited. The resonantly reflected light from the sensor carries information about the effective refractive index encountered by the orthogonally polarized guided modes stored as phase information. The Wollaston prism introduces an angle of 1° between the two modes. The two diverging beams overlap in the camera plane, and generate a high-contrast interferogram for an analyser orientation of approximately 45°.

about all setup components can be found the Appendix 8.2.4.

Wollaston prism working principle

Light entering a Wollaston prism is split into two orthogonally polarised components which diverge at an angle α after leaving the prism (see Fig. 22). The key to operation is a polarisation-dependent path difference which is introduced by the birefringent material. The divergence angle α after transmission through the prism is given by [76]:

$$\alpha = (n_e - n_o) tan\theta \tag{29}$$

where n_e/n_o are the extraordinary/ordinary refractive indices of the prism and θ is the angle of the prism wedge.

If the polarisation of the incident light is oriented at 45° with respect to the optical axis of the prism and if another polariser at the output of the prism is oriented again at 45°, the common components of the light interfere and the period of the interferogram (compare to Fig. 20) is given by $\approx \lambda/\alpha$ [76].

To split the incoming beam in two orthogonally polarised beams, differential interference contrast microscopy (DIC microscopy), as an example, also uses Wollaston prisms. DIC microscopes require lenses to achieve parallel beams entering the sample and also a second prism to combine the beams at the output and let them interfere.

Because we do not need to extract the spatially varying phase information to reconstruct an image, in this approach it is not necessary to perform phase shift interferometry contrary to the approach of, for example, large-FOV interferometric on-chip microscopes (LIM) [75]. The information we want to extract is the relative phase difference between two modes. Note that for sensing, it is only necessary to extract the relative phase change over time and the required information is therefore present in the

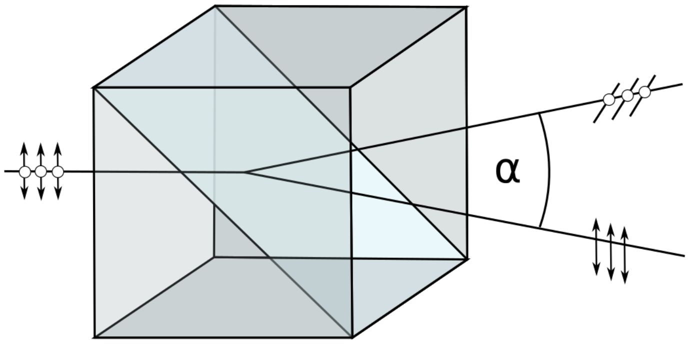

Figure 22: Working principle of a Wollaston prism. A light beam passing through the prism is split into two beams with orthogonal polarisation which diverge with an angle α. This is achieved by using a birefringent material which introduces a path difference between the two polarisations.

consecutive single interferograms themselves.

3.3 Design and fabrication of resonant nanostructures

The most obvious way of realising a resonant common-path interferometric approach would be to design a single grating such that both modes overlap spectrally. While this is possible (Fig. 23), it is only achievable for a restricted set of grating parameters and would therefore constrain the ability to optimise the sensing performance, particularly the phase sensitivity. Especially for high grating fill-factors (high ratio of grating ridge width over period a), corresponding to a higher phase sensitivity, the TE and TM modes do not overlap spectrally at all. This can be explained by the TE mode being predominantly confined to the grating grooves (Fig. 23) and therefore being more sensitive to changes in grating fill-factor.

Alternatively, it is possible to design two separate gratings with independently optimised grating parameters to ensure a resonance at the same wavelength for both polarisations. The reflected signals from the two gratings are then spatially superimposed

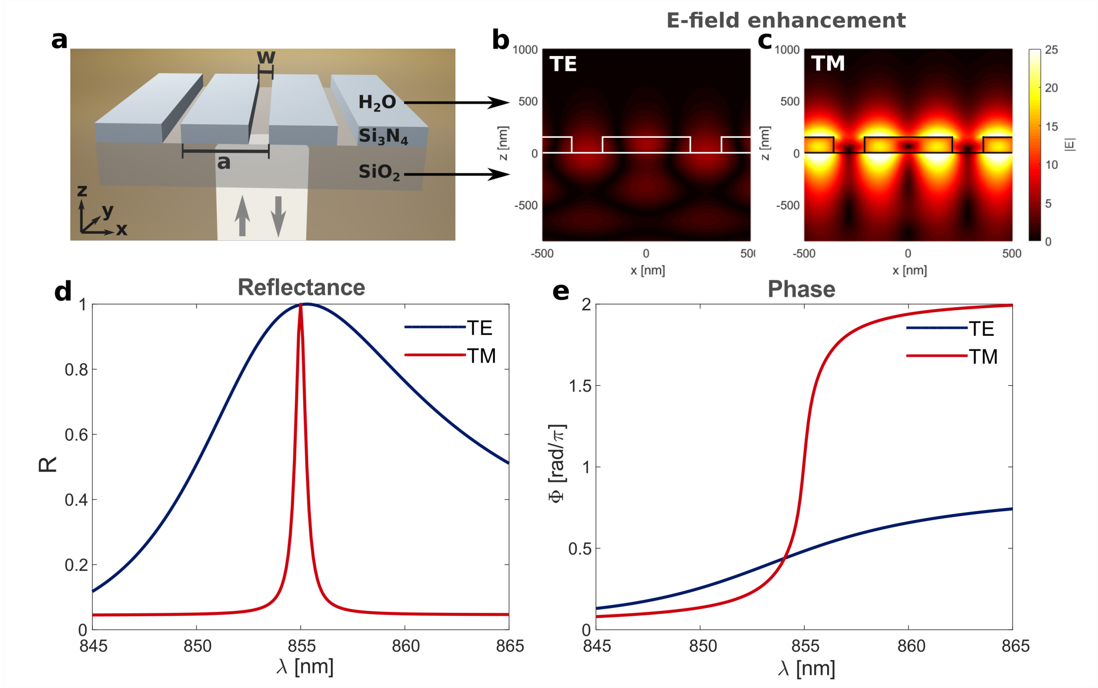

Figure 23: **a**, Schematic of a typical GMR structure consisting of a silicon nitride (n=2.02) grating of 150 nm thickness on glass (n=1.45) substrate immersed in water (n=1.33). The grating period in this example is a = 572 nm and the filling factor is 75%. A plane wave is incident from the glass substrate layer. The TE/TM mode is excited when the E-field vector of the incident beam is oriented perpendicular/parallel to the grating vector. **b, c,** Dominant E-field components of TE (y-component) and TM (z-component) modes with an evanescent field decaying from the grating surface into the cover layer. **d,** Simulated reflectance with spectral mode overlap and **e,** simulated phase response, using rigorous coupled wave analysis (RCWA).

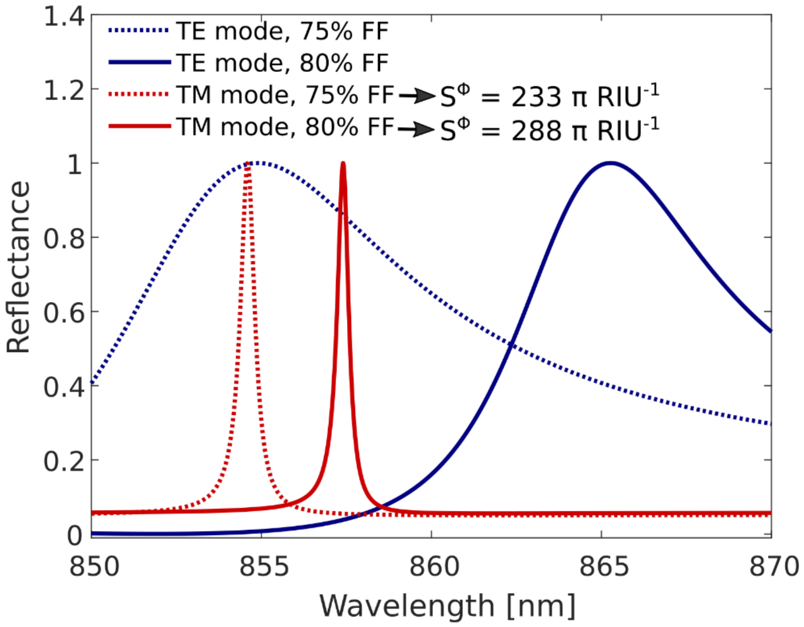

Figure 24: RCWA simulation showing the spectral mode overlap of a single structure for different filling factors (FF). The phase sensitivity is higher for maximised FF, while the spectral overlap for the TE/TM mode is only achieved for a narrow range of lower FF.

in the camera plane.

To further clarify the motivation behind the independent optimisation of the TE and TM gratings, Figure 24 shows a corresponding simulation. Since the quality factor of the GMR increases with a higher filling-factor, a high grating filling-factor is desirable for maximum sensitivity. For example, the TE and TM modes spectrally overlap perfectly in the case of a fill-factor of 75% while the overlap is close to zero for a fill-factor of 80%, where the TM mode has higher phase sensitivity.

Following this argumentation, to improve sensitivity it is necessary to measure the phase difference between the modes of two separate photonic nanostructures, which are optimised for their respective purpose as signal (TM mode, high sensitivity) and reference (TE mode, low sensitivity) without the need for spectral mode overlap. This can be achieved by designing independently optimised, adjacent gratings with a high filling-factor for the TM grating and then creating an adequate shear between the resonantly reflected TE and TM polarised light, with the Wollaston prism, to achieve spatial TE/TM overlap. In this case, the TE and TM modes of the same structure are spectrally separated and cannot interfere. Designing the two resonant structures separately adds versatility and the ability to optimise both modes independently.

Dynamic range considerations

The dynamic range of the measurement is generally limited by the sharper resonance, here the TM mode. Since the maximum phase sensitivity occurs around the centre of the resonance, both the sensitivity and the contrast of the interferogram decrease as the resonance is probed with varying refractive index. Clearly, the sharper the TM resonance, the more sensitive the measurement, but also the smaller the dynamic range. In order to overcome this limitation, I designed several grating stripes of slightly different periods for the high-Q TM mode. Having multiple stripes probing adjacent phase curves improves tolerances against fabrication, temperature and incident angle variations as well as broadening the range of available biosensing applications. Providing multiple stripes is only required for the TM mode since the TE mode resonance is substantially broader and therefore intrinsically more tolerant, which is why it is a good reference. In order to also account for any system drift, which may be caused by temperature variations either of the environment or the analyte, I further implement a differential scheme using a second interferometric GMR as a reference channel. The reference channel is isolated from the signal channel via a microfluidic system and the refractive index in the reference channel is kept constant such that is can be subtracted from the signal channel to yield the effective phase response.

The design of the dielectric structures in the field of view is shown in Figure 25. For all simulations I assume a SiO_2 substrate refractive index of 1.45, a Si_3N_4 refractive index of 2.00 and a H_2O cover refractive index of 1.33. The angle of excitation is zero.

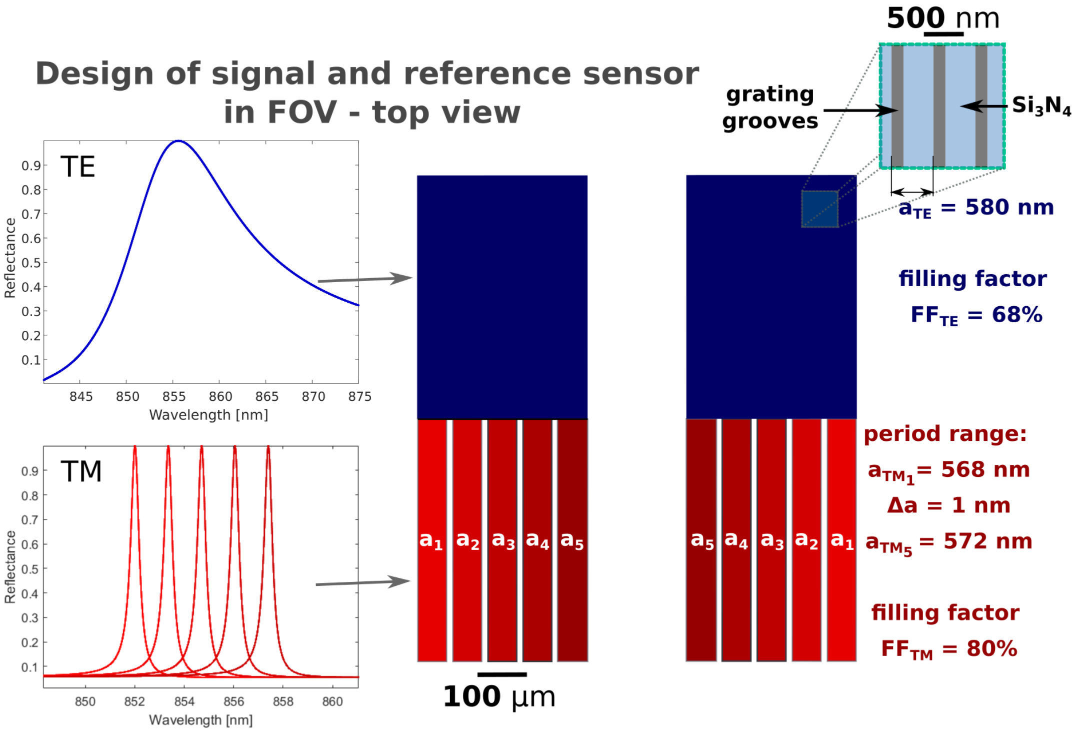

Figure 25: Design parameters (period a, filling factor FF) and corresponding simulated resonance peaks. All other parameters (index, thickness...) are provided in the caption of Fig. 23. Areas within the field-of-view (FOV) designed to excite a TE mode are marked blue and those exciting a TM mode are marked red. The orientation of the grating grooves, for both TE and TM designs, is along the long axis, as indicated in the top right zoom. This design schematic is the basis of the experimental images shown in Figure 28.

The two identical (350 x 500) μm^2 structures (blue) on the top are designed to resonate for those components of the incident light which are polarised in the direction of the grating grooves at the laser diode wavelength of 855 nm. A grating period of 580 nm in combination with a filling factor of 68% provides this resonance condition for the TE mode. The distance between the two identical structures is 200 μm, which is the distance between the microfluidic signal and reference channel.
In the right bottom row in Figure 25, the implementation of the five grating stripes in each channel is shown. The grating period of these structures varies from 568 nm to 572 nm with a period step size of 1 nm in the left channel and a mirrored version (for symmetric excitation) of these stripes in the right channel. In combination with a filling factor of 80%, these parameters ensure a resonance wavelength around 855 nm for incidence light which is polarised orthogonal to the grating grooves (TM mode).

There is a trade-off between the width of each stripe (here 62 μm), which allows for averaging and thus noise reduction, and the dynamic range, considering that there is only a limited field of view available. The best choice of size and number of stripes depends on the specific application of the sensor. In practice, I found that for the goal of measuring low concentrations of small proteins, a minimum of five grating stripes gives sufficient tolerance for both the fabrication and incidence angle of the measurement to ensure that a resonance from one of the stripes is visible at the operating wavelength. If, for example, a different application would require a wider dynamic range or higher tolerance, then a smaller grating width and a larger number of gratings could be implemented.

Nanostructure fabrication principles

The details of the nanofabrication protocol that I used to fabricate the designed grating structures are explained in Appendix 8.2.1. To summarise the main steps (see Fig.

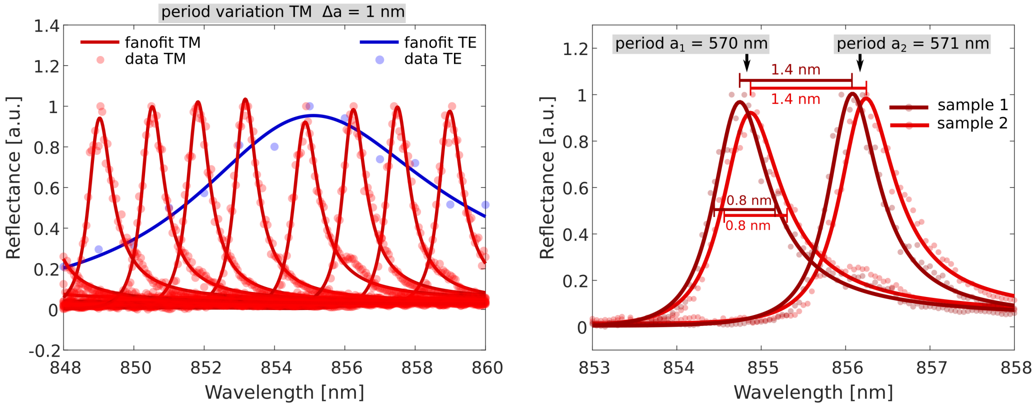

Figure 26: Spectral characterisation of structures designed as shown in Figure 25, here with a wider grating period variation range on the left. The spectra were aquired by taking hyperspectral images using a halogen lamp in combination with a monochromator and recording the intensity in every pixel. On the right, the two spectra correspond to identically designed gratings fabricated on two different samples.

27, top), after cleaning a (15x15) mm^2 the silicon nitride (Si_3N_4) sample, I spin a high resolution lithography resist using a spin-coater. The purpose of this resist is, as the name suggests, to resist the etching process. Therefore, a nanopatterned mask of resist allows to selectively etch the designed nanostructures. Because the resonances rely on nanometre accuracy, electron beam lithography (EBL) is used to pattern the resist in those areas where the grating grooves are designed to be. Since Si_3N_4 is not conducting, a charge dissipation layer has to be spin-coated on top of the resist before exposure, which is removed after exposure. The next step is to develop the resist. This means that those areas of the resist polymer, which were exposed by EBL, and thus have different material properties, can now be removed chemically. This leaves a nanopatterned layer of resist on top of the sample, which is then used to etch, with reactive ion etching (RIE), the Si_3N_4 and create the grating grooves. Any remaining resist is then removed and the gratings are in their final form (see Fig. 27, bottom).

Spectral characterisation of resonances

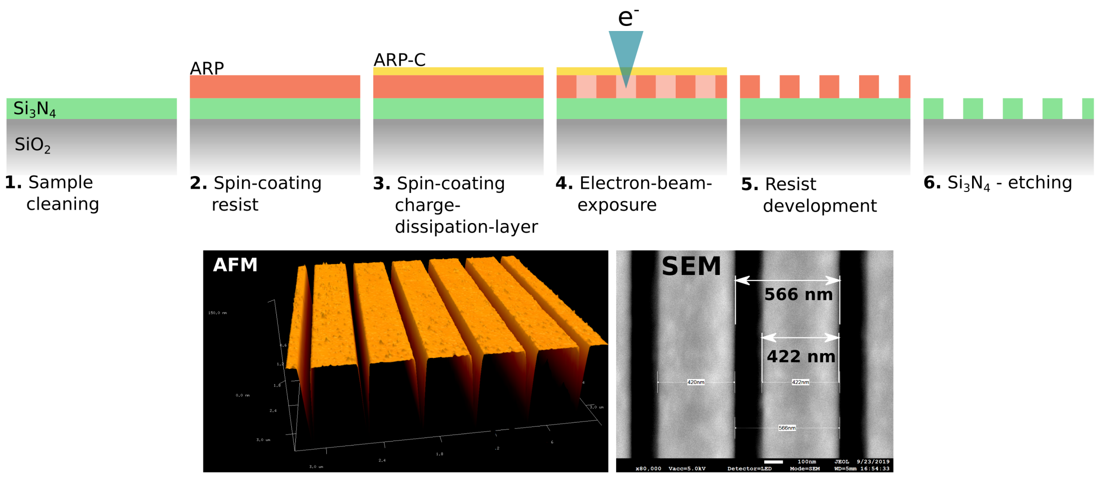

Figure 27: Top: Schematic of nanofabrication process. Bottom: SEM and AFM of fabricated grating structures in Si_3N_4 with a charge dissipation layer for the SEM to avoid distortions due to charging. A detailed fabrication protocol can be found in Apprendix 8.2.1.

To investigate the spectral characteristics of the adjacent TM modes, Figure 26 shows high-resolution spectra obtained by sweeping the incidence wavelength using a combination of halogen source and monochromator. As expected, when comparing the response of two different samples (on the right), the central wavelength of the resonance peaks can shift slightly due to fabrication variations, whereas the FWHM (0.8 nm) and the distance between two adjacent peaks (1.4 nm) stay the same.

3.4 Experimental realisation of resonant interferogram formation

Figure 28 shows the implementation of the designed and fabricated photonic nanostructures (Fig. 25) in the interferometric GMR setup (Fig. 21) and the resulting interferogram for three different analyser orientations. At an analyser orientation of 0°, the gratings that are designed to resonate for the TE mode light up (Fig. 28 c, top), while the orthogonal orientation lets through the light reflected from gratings designed for the TM mode (Fig. 28 c, bottom). The analyser operating orientation for sensing is at approximately 45°, which allows TE and TM mode to interfere and form the interferogram shown in Figure 28 e.

3.5 Principle of phase extraction

Phase extraction is often applied to reconstruct the image of an unknown phase object. In digital holography for example, an interferogram is recorded, which encodes the phase information of the wave that interacted with the object of interest, e.g. a weak scatterer like a small cell in aqueous solution. The contrast of the reconstructed image relies on the knowledge of the phase of the wave in each pixel. Without the phase information, many objects scatter light insufficiently to visualise them with high contrast either because of their small size or the low refractive index contrast that they form with their environment.

In holography, using a 2-D Fast Fourier transform (FFT), the interferogram is first converted to the spatial frequency domain, where one of the cross-correlation terms is cropped. This term is then transferred back to the image domain by a 2-D inverse fast Fourier transform (IFFT) and contains the desired complex wavefront information with the phase as argument [77].

The phase extraction requirements and aims in this work are different from such an approach. To gain information about the relative phase change of the resonantly reflected light, it is not necessary, at this stage, to reconstruct an image. Instead, the phase can be directly extracted from the interferogram (see Fig. 28 e) without image reconstruction, because the imaged sensor regions where the phase is expected to change homogeneously are known by design and can be selected and averaged in the interferogram during data post-processing. The phase can be extracted from the, now one-dimensional, information either by using the Fourier transformation approach (Fig. 29) or by fitting a cosine (see also Appendix 8.3).

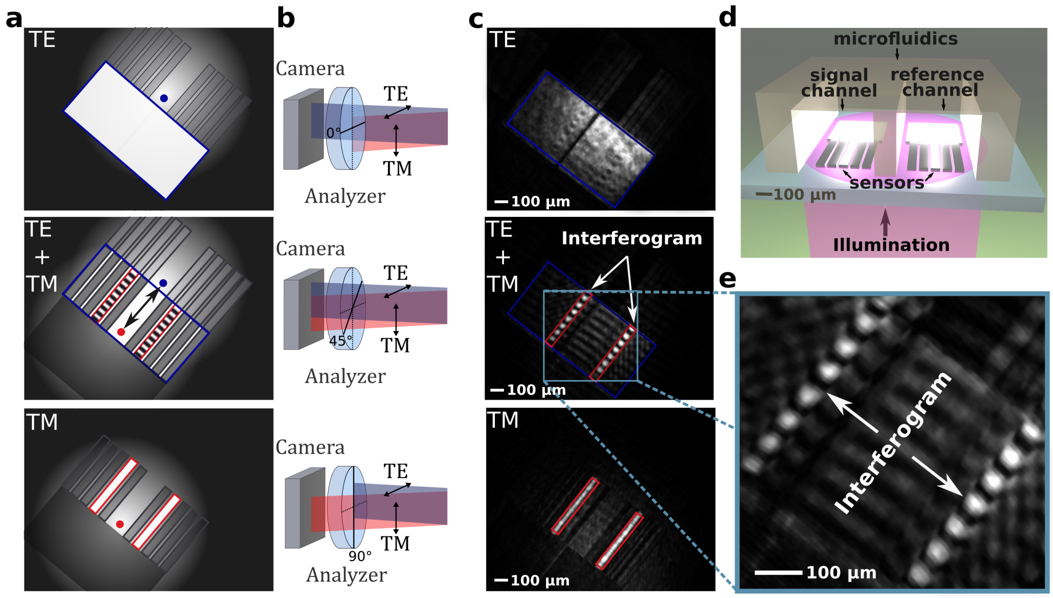

Figure 28: Schematics and camera images showing the spatial grating overlap principle. Compare to design in Figure 25. **a** Schematic of interferogram formation with spatial mode overlap of adjacent structures designed to resonate for TE/TM polarization shown for 0°, 45°, and 90° analyzer orientations. The blue/red frame indicates the structure resonating for TE/TM polarization. **b** Corresponding analyser orientations and **c** corresponding camera images. The area with a blue frame is a uniform grating designed to resonate at $\lambda = 855\,nm$ in water for TE polarization. Correspondingly, it shows high reflectance for the 0° analyser orientation. The narrow stripes are designed, such that one resonates for TM polarization; since the TM resonance is much narrower, I here use several stripes consisting of gratings with different periods ($\Delta a = 1 nm$) to ensure that at least one of them is on resonance within the expected refractive index range of the analyte. This principle ensures a high dynamic range. Correspondingly, only one of the grating stripes lights up at the 90° analyser orientation (red frames). When the analyser axis is set to 45°, the TE and TM components can interfere and create an interferogram in the beam-overlap region. **d** Schematic of sensors integrated in a microfluidic system. I use a signal and a reference channel to enable drift subtraction. **e** Zoom of **c** (middle)

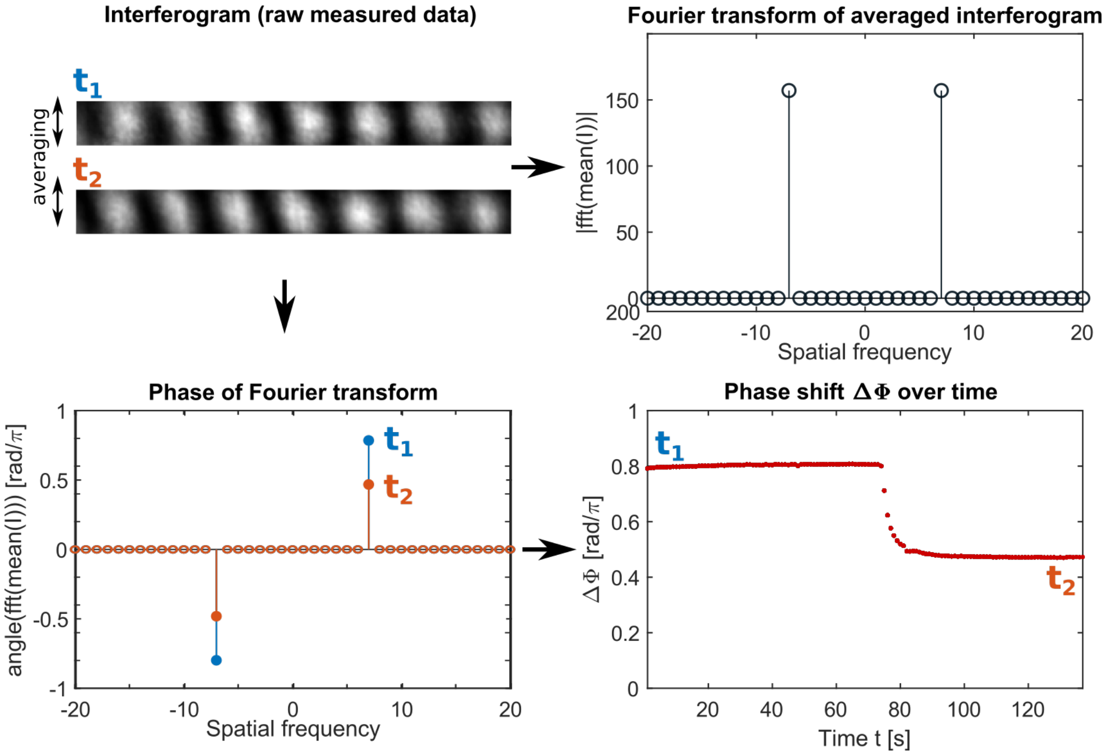

Figure 29: Principle of phase extraction from interferogram by fast Fourier transform (FFT) with MATLAB script. The 2D interferogram is first averaged orthogonal to the fringe direction and the magnitude of the FFT of this 1D sinusoidal function reveals the spatial fringe frequency (top right), while the phase angle of the complex FFT is used to extract the phase information of this spatial frequency over time. See Appendix 8.3 for details.

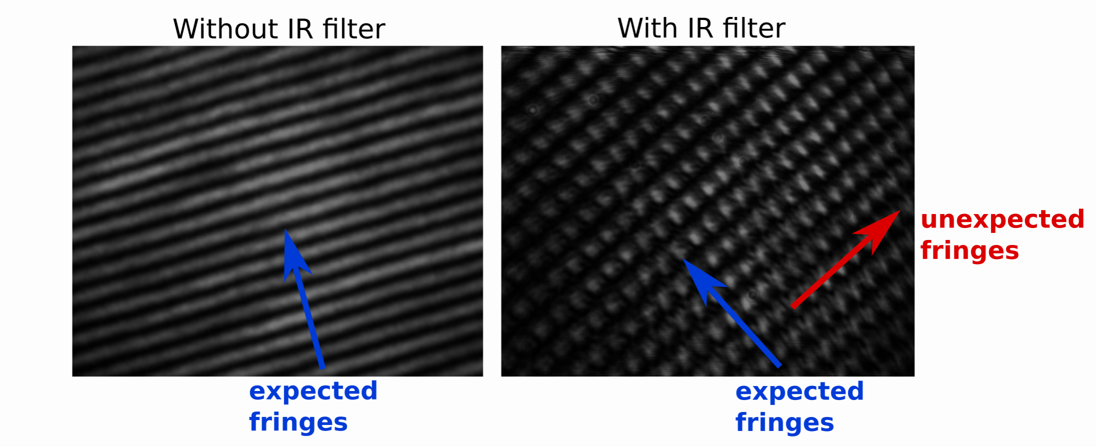

Figure 30: The camera, which is used in the optical setup for interferometry, has a default infrared filter (IR filter) in front of the camera sensor. By removing the filter, the clean, expected fringes are obtained.

3.6 Discussion

Camera infrared-filter considerations

To leave no gaps in the considerations taken for the interferometry setup, I want to briefly mention an issue I encountered in the beginning of the project when the first images looked like the image in Figure 30 on the right.

The unexpected fringes, which in this case are orthogonal to the expected fringes (Fig. 30), were introduced by an infrared filter, which is present in many cameras, including the Thorlabs camera used here (see Appendix 8.2.4). A small angle of this filter with respect to the incident light can then cause unwanted interference effects. After removing this filter, the interferogram becomes clean and only the expected fringes, created with the Wollaston prism, are visible. Another advantage of removing the filter is that it previously filtered part of the laser diode light at 850 nm, which means that we can now use lower integration times for the same brightness.

Light-source coherence considerations

Interference between two delayed replicas of the same wave can only be observed if the optical path difference is smaller than the coherence length. Correspondingly, the visibility of the interference fringes depends on the degree of temporal coherence, with the visibility or contrast being defined as:

$$C = \frac{I_{max} - I_{min}}{I_{max} + I_{min}} \tag{30}$$

The intensity of the superposition of a partially coherent wave with a delayed replica of itself (delay time τ) can be written in terms of the spectral density S(ν) [56]:

$$I = 2\int_0^{\text{inf}} S(\nu)[1 + cos(2\pi\nu\tau)]d\nu \tag{31}$$

with the frequency ν. This equation can be interpreted by saying that the interferogram intensity varies between maximal and minimal intensities which depend on the spectral width of the source such that a narrower line-width $\Delta\nu$ corresponds to a long coherence time.

The interference equations considered in the theory section above [see Eq. (26)], are derived for the case of an infinitely narrow light source. A more general and realistic equation for practical implementations is the following:

$$I = I_1 + I_2 + 2\sqrt{I_1 I_2} \cdot |g_{12}| \cdot cos\Phi \tag{32}$$

with the normalised cross-correlation g_{12} of two partially coherent waves [56]. For perfectly coherent waves with phase difference Φ, the Equation (26) is recovered with $|g_{12}|$ = 1, while for uncorrelated waves with $|g_{12}|$ = 0, there is no interference effect and the total intensity I is simply the sum of the intensities of both waves.

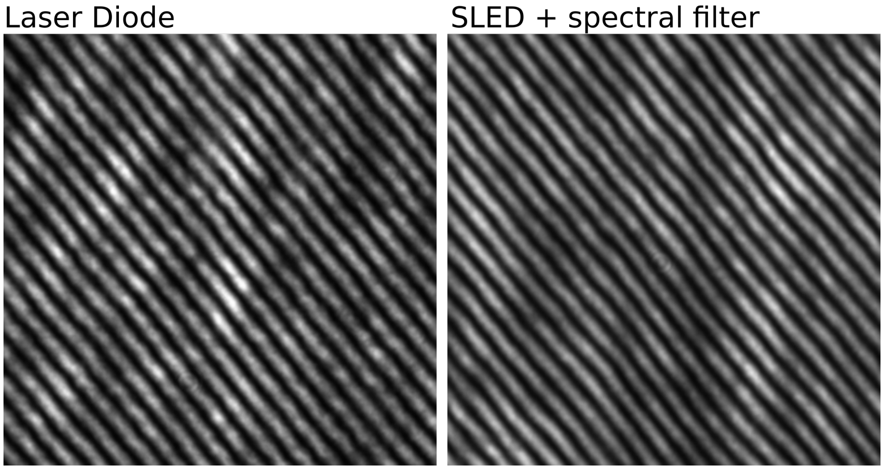

Figure 31: Raw camera images for qualitative comparison of interferogram contrast using a laser diode (left) and a spectrally filtered superluminescent diode (SLED, right).

Taking these considerations into account, the safest choice of light-source is evidently a source with high coherence length, characterised by a narrow spectral line. Alternatively, a broadband source could be combined with a spectral filter to achieve sufficient coherence.

I experimentally tested both a narrow laser diode module (LD, Thorlabs CPS850V, FWHM $< 100\,\text{pm}$) and a broad super-luminescent diode (SLED, Superlum cBLMD, FWHM $\approx 165\,\text{nm}$) using the Wollaston prism as shearing element as discussed above. The images in Figure 31 suggest that a spectrally filtered SLED diode (filter Laser 2000 LL01-852-25, FWHM $\approx 3\,\text{nm}$) could provide sufficient coherence for this interferometry setup, which is in accordance with previously published work on interferometry using spectrally broad sources, e.g. [33]. Note that these tests are carried out with a mirror rather than a resonant structure. While broadband excitation could have the advantage of an inherently wider dynamic range without the necessity of tuned structures, I have decided to focus on laser diodes for resonant interferometric sensing, mainly because probing the phase response at a single wavelength provides a higher SNR

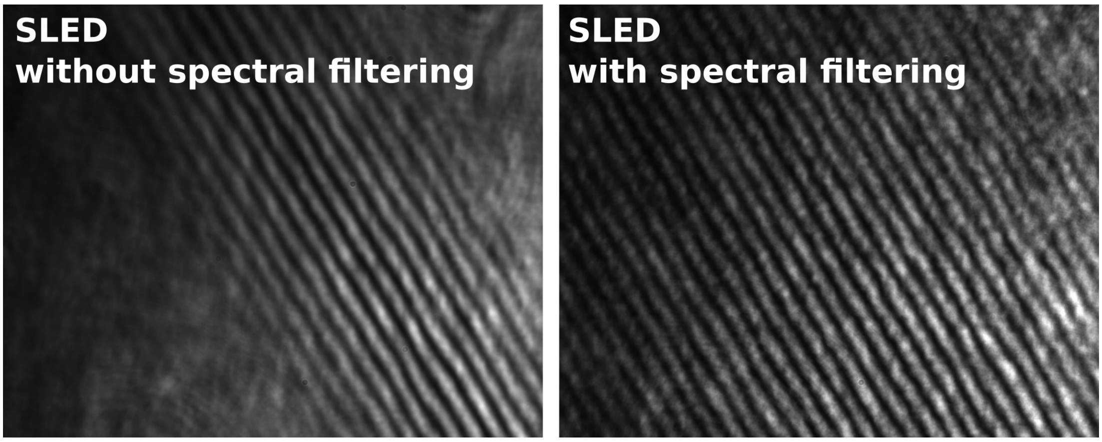

Figure 32: SLED interferogram with and without spectral filtering.

for the resonantly reflected signal with respect to background reflections. The core principle of this common-path interferometry approach relies on measuring the optical path difference between TE and TM modes. Specifically, when the goal is to measure phase differences between a narrow signal mode and a broader reference mode, using a broadband source would result in a intensity dominating reference beam. Choosing the laser diode as source is therefore the safer and more practical choice considering also the future goal of miniaturisation (see outlook, Section 6.2) and cost-effective implementation, where spectral filters would be a possible limitation.

A further interesting comparison to better understand the role of coherence in interferometry is shown in Figure 32. Without spectral filtering of the SLED, the number of visible fringes is reduced considerably. This effect is similar to the effect of low coherence on the visibility of Young's interference fringes, where the number of observable fringes can be estimated via [56]:

$$N = \frac{l_c}{\lambda_0} = \frac{\nu_0}{\Delta \nu_c} \tag{33}$$

which means that the number of fringes increases with the ratio between coherence length l_c and central wavelength λ_0 or equivalently with the ratio between central frequency ν_0 and linewidth $\Delta\nu_c$. The difference to the Young's interferometer is that, there the angle is introduced by the distance of the slits or pinholes while here, the angle is introduced by the Wollaston prism.

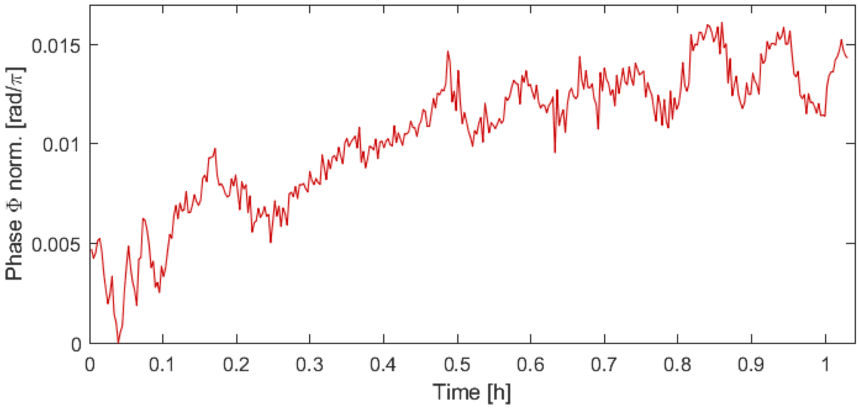

Figure 33: Mechanical noise in the case of mirror as sample when the mirror is not fixed on the sample stage. Overall drift reduces over the course of one hour, while smaller vibrations are still present after this initial stabilisation.

4 Experimental Resonant Phase Measurements

4.1 Noise and drift characterisation

Understanding the origins of system noise is crucial for low-cost, high-performance sensing. Random noise can usually be filtered and is therefore unlikely to be the limiting factor. What is, however, limiting the system stability is drift over time, which can be related to instabilities of the source, e.g. temperature dependent wavelength, as well as instabilities of the liquid, e.g. temperature dependent refractive index of water or even mechanical instabilities of the sensor position, e.g. time dependent reflection angles in combination with not perfectly collimated light.

4.1.1 Mechanical drift

To understand where the different components of the drift and noise are originating, I first analyse the signal reflected from a mirror rather than from a resonant structure. This allows to exclude the effect of drift related to temperature dependent refractive index changes of the liquid solution.

Figure 33 shows the effect of such a mechanical sample drift. The mirror was not fixed to the sample stage and as such, it initially drifts in position on the sample stage until it stabilises after around half an hour. Not being fixed in position still allows the mirror to vibrate as can be seen from the low frequency noise at the end of the measurement. Taking this drift due to poor mechanical mounting into account, all further measurements were performed with samples that are mechanically fixed to the sample stage by means of small magnets integrated in the microfluidic clamping system.

4.1.2 Influence of fringe contrast on read-out noise

As mentioned before, one of the advantages of measuring the phase difference between orthogonally polarised light is the ability to adjust the fringe contrast of the interferogram by means of the analyser orientation, which is an important advantage compared to non-polarisation based interferometry because it allows to interfere a reference and signal with maximal contrast even without inherently matching the reflectance of the resonances. The relative intensities can simply be adjusted with the analyser. Here, the analyser allows to optimise the relative brightness of the modes for each measurement individually.

The assumption is that the fringe contrast has an effect on the stability of the read-out, because a higher contrast increases the amplitude of the interferogram frequency in Fourier space and therefore should allow for more stable filtering than a low-contrast interferogram. To test this assumption, I conducted phase measurements over 1-hour periods comparing the noise for different contrasts. Figure 34 shows that an average decrease in contrast of 18% leads to an increase of the 3σ value of 8%, where the contrast was calculated using (see Eq. 34 in Section 3.6):

$$C = \frac{I_{max} - I_{min}}{I_{max} + I_{min}}. \tag{34}$$

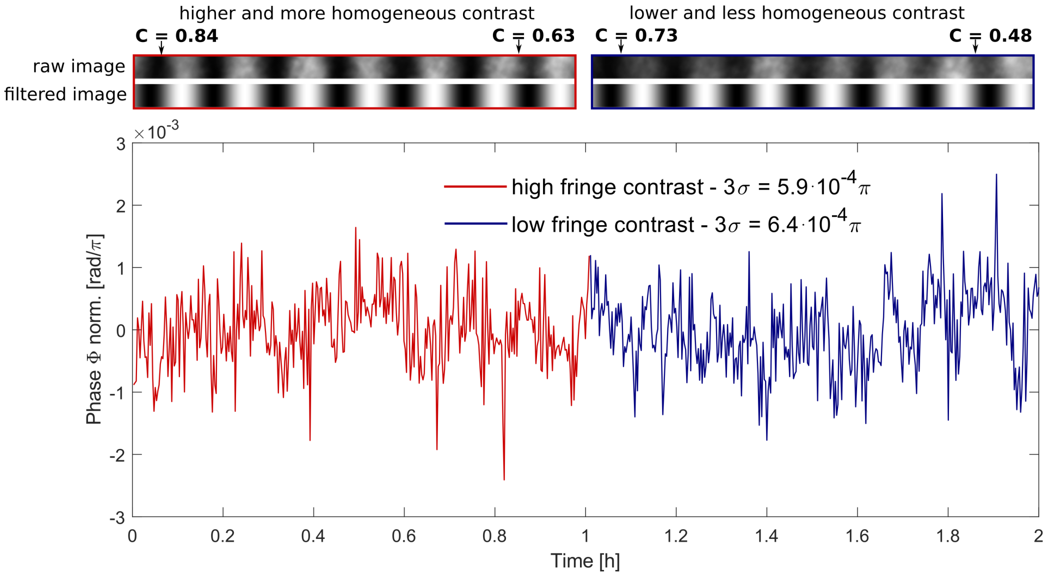

Figure 34: Noise characterisation - dependence of noise on fringe contrast independent of temperature drift. The sample is a mirror and the laser diode was switched on 1 hour before this measurement to exclude the effect of temperature dependent wavelength drift. The contrasts C are calculated with Eq. (34) and are marked in the corresponding raw image position to show both the absolute contrast and the contrast variation due to the Gaussian beam.

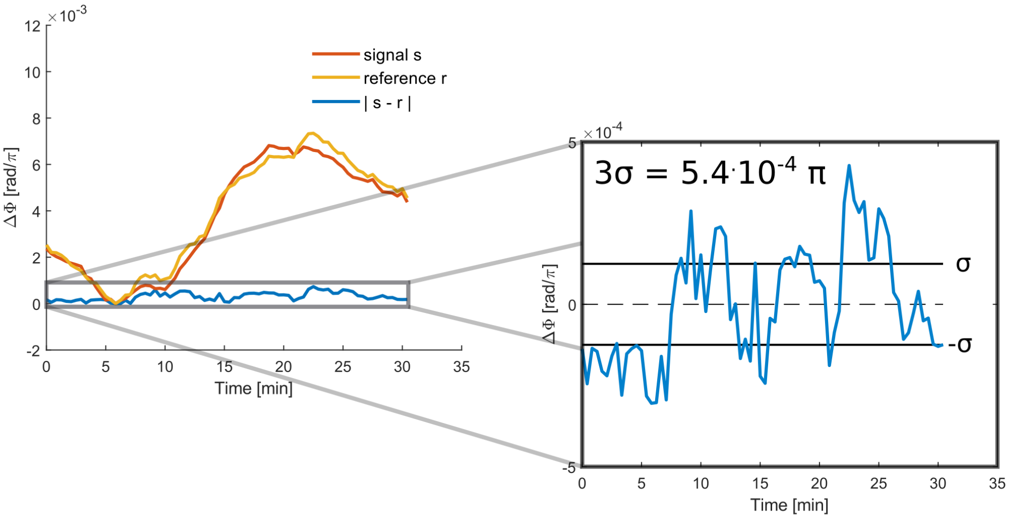

Figure 35: Example data showing the drift referencing principle. The signal ‘s’ corresponds to the phase response determined in one microfluidic channel and the reference ‘r’ to the signal obtained from the adjacent channel, which is subtracted from the signal to obtain the effective phase response over time while flowing DI H_2O through both channels in this case.

Although this increase in the system noise due to lower contrast can be considered relatively low, the contrast is maximised for all experiments to ensure that it is high enough to stably filter the interferogram by selecting the strongest frequency in Fourier space.

4.1.3 Temperature drift

Because temperature drift cannot be removed in post-processing, as it cannot be anticipated and it may not be distinguishable from the biomolecular binding response, a drift reference needs to be included in the experimental system. The drift reference is realised experimentally by including a second microfluidic channel in the FOV (Fig. 28), which includes a mirror version of the photonic nanostructure of the signal channel and is separated from the signal channel, such that the response is independent from the solution in the other channel.

As is evident from Figure 35, the signal and reference channels do not show the exact same response to a deliberately constant refractive index, which indicates either that the temperature related refractive index changes are not exactly the same in both channels or that the sensitivity in both channels is not the same. These effects are currently limiting the noise to $3\sigma = 5.4 \cdot 10^{-4}\pi$. In order to further reduce this noise, the nanostructures in channels s and r need to be even better matched and a closer similarity of temperature effects needs to be ensured in all microfluidic channels. For now, we will assume that the calculated 3σ is the lowest achievable level in this system, which will be taken into account later on, after introducing the experimental sensitivity, to estimate the refractive index LOD based on Equation (23).

4.1.4 Discussion

In this section, I want to briefly discuss another potential source of noise, which I have identified more recently and not yet solved. The reflection of partially transmitted light from the PDMS microfluidic channel is a particular type of noise that is more difficult to distinguish from other sources of noise than, e.g., temperature drift.

PDMS is a relatively soft and flexible polymer (see appendix 8.2.2 for details) and can therefore be deformed when pressure is applied. It is possible that the microfluidic pumping itself can build up pressure such that the PDMS is deformed during a measurement. Since the light source is highly coherent (Section 3.6), non-resonantly reflected light from the PDMS interface could interfere with the light reflected from the sensor; if the surface of the PDMS is deformed over time by the microfluidic pumping, this could lead to undesired time-dependent intensity variations.

To eliminate this source of noise, which is difficult to quantify, either a sturdy material needs to be used for the channel or the PDMS has to be isolated from any possible deformation due to the pumping. A preliminary solution is to use an anti-reflection coating, e.g. a light absorbing ‘camouflage´ spray paint (KRYLON Camouflage Paint

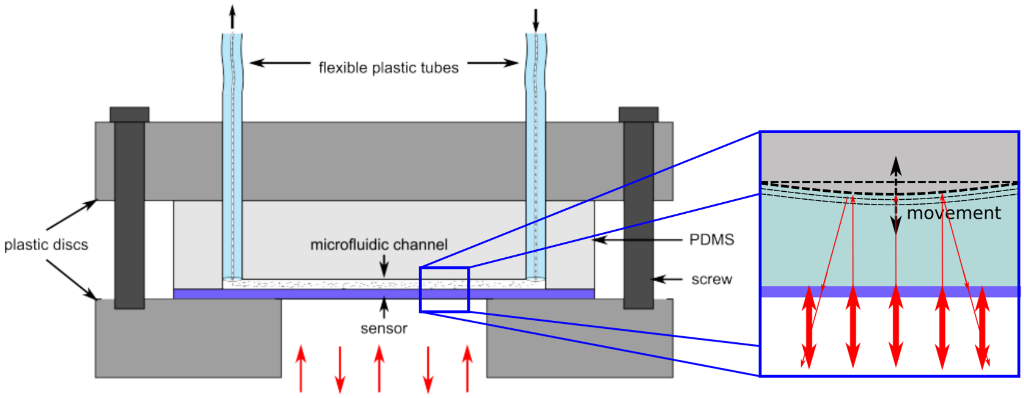

Figure 36: Variations in the PDMS microfluidic channel thickness as a possible source of noise. The tubing is not mechanically isolated from the PDMS channel, which can lead to pressure being applied to the channel by the tubing, which results in pulling the PDMS around the holes up while the pressure applied by the clamping system pushes the PDMS down, which leads to deformations.

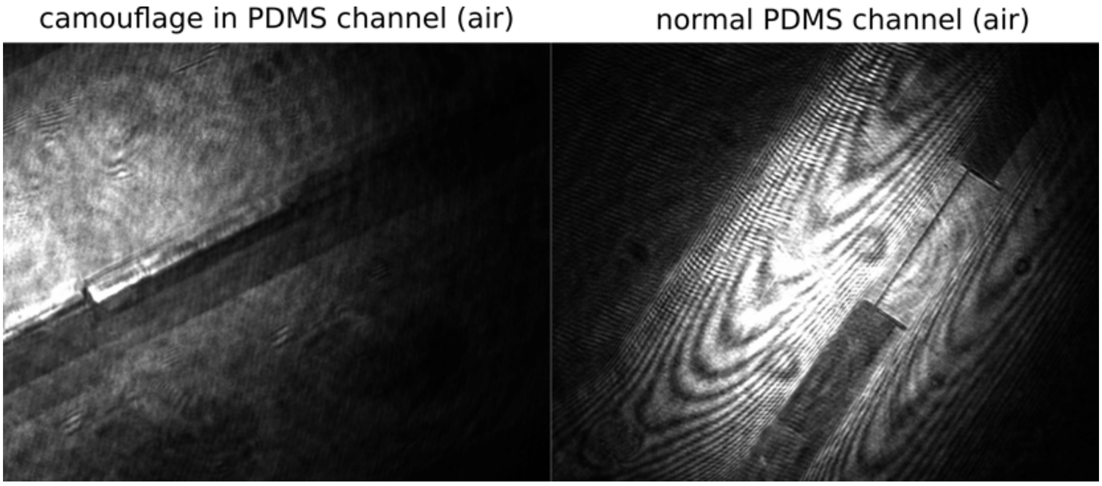
camouflage in PDMS channel (air)

normal PDMS channel (air)

Figure 37: Raw camera images illustrate backreflections from the PDMS microfluidic channel in air (right image). The interface here is chosen to be air-PDMS (off resonance) because the effect of the backreflections is difficult to visualise for the lower index contrast of a water-PDMS interface. On the left, the effect of using an absorbing layer (‘camouflage’ spray paint) which is sprayed on the PDMS surface inside the channel is visible. The absorbing layer significantly reduces the backreflections, which are not detectable by eye anymore in the left image.

with Fusion Technology (Black)) as shown in Figure 37. This approach very effectively removes the background fringes and the paint is tested to be stable in aqueous solution for at least 24 hours. The removal of PDMS reflections could thus further reduce the system noise, which was determined (see Fig. 35) without this absorbing layer in the channel. Because it is not known at this point, if the spray paint would negatively interfere with biomolecular interactions in the channel, a preferred solution would be to use, e.g., glass microfluidics, where a channel deformation is not expected.

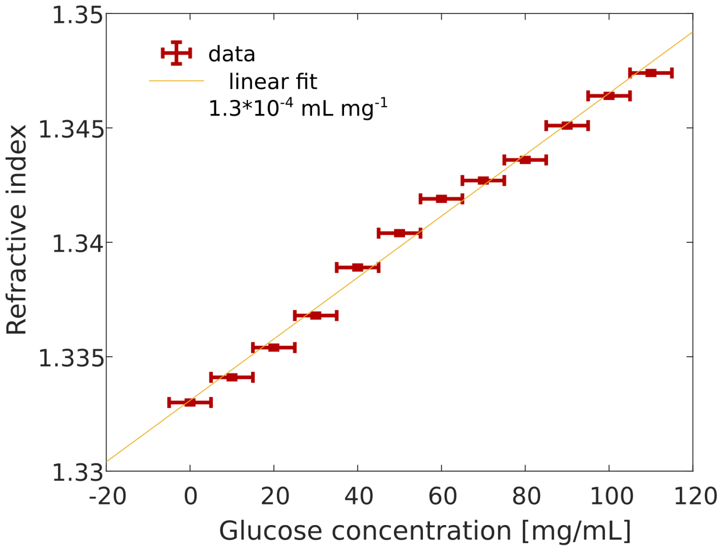

Figure 38: Experimentally determined refractive index of different glucose-H_2O-solutions. The refractometer which was used has an accuracy of $\Delta n = 10^{-4}$.

4.2 Experimental phase sensitivity

4.2.1 Calibration

To experimentally obtain the phase curve of a resonant structure and from there determine the phase sensitivity, the refractive index is altered step by step within the range of the resonance. This is usually done by flowing either salt or glucose solutions of known refractive index over the sensor and measuring the corresponding response. Here, glucose solutions are prepared and their refractive index is determined with a commercial refractometer for calibration (Fig. 38).

4.2.2 Experimental phase sensitivity

Figure 39 shows the phase change measured as a function of the refractive index of the liquid on the sensor surface using glucose solutions of increasing concentration, which were calibrated according to Figure 38.

After every glucose solution, deionised water is pulled over the surface to compare

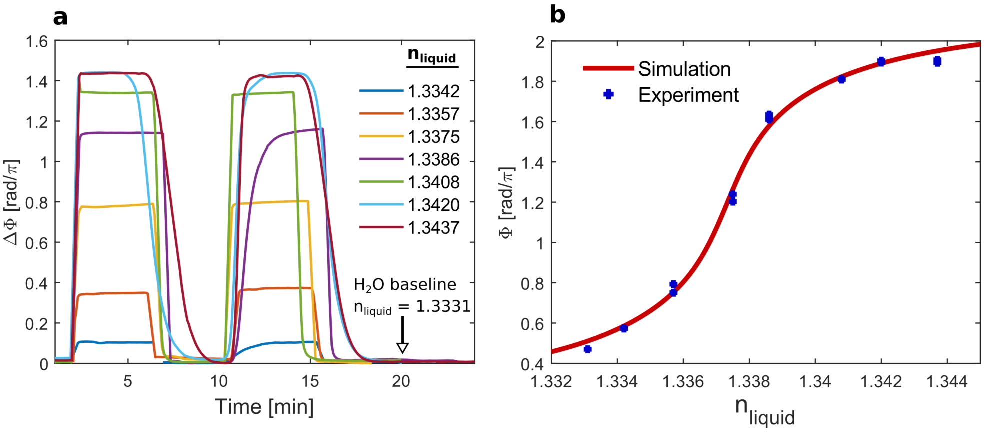

Figure 39: Bulk sensitivity measurements and experimental phase curve. **a** Starting from a H_2O baseline with a refractive index of 1.3331, glucose solutions of a refractive index in a range between 1.3342 and 1.3437 were flowed over the surface, and the corresponding phase response was measured. I repeated the measurement twice for each concentration to verify system stability. **b** Phase curve obtained from the measurement on the left in comparison with the simulated phase response. The error of Φ of each single blue point is determined by calculating the standard deviation of the saturated response in each glucose step shown in **a**. This error is smaller than the marker size in **b**.

each response to the initial H_2O-baseline (n = 1.3331). This process is repeated twice to gain insight into the repeatability of the phase response and the stability of the system.

From these responses (Fig. 39 a), the phase curve can be obtained (Fig. 39 b) and the phase sensitivity can be calculated by fitting the linear range of the phase curve. Here, the phase sensitivity S is calculated to be $290\,\pi\,\mathrm{RIU}^{-1}$. In combination with the measured 3σ noise level of $5.4{\cdot}10^{-4}\pi$, a bulk limit of detection (see Section 2.3.5) of

$$\mathrm{LOD} = \frac{3\sigma}{S} = 1.8 \cdot 10^{-6}\,\mathrm{RIU} \tag{35}$$

is determined.

Note that the simulation in Figure 39 is plotted with the experimental data to show the good agreement of the phase curve shape and therefore the phase sensitivity. The grating parameters of the simulated and the expected fabrication are the same and to achieve the agreement in the position of the phase curve, I altered the incidence angle since I am also using the angle of incidence as a means to fine-tune the resonance wavelength in the experiment. This approach of incidence angle sweeping in the experimental alignment is thus taken also in the simulation to achieve an overlap between the experimental data and the simulation. It would be more conventional to fit the experimental data, but the aim here is to visualise the agreement between experiment and simulation in terms of the phase curve *shape*.

4.2.3 Dynamic range extension experiments

As discussed in the design Section 3.3, a sharper resonance peak of a single nanostructure corresponds not only to higher phase sensitivity but also to a lower dynamic range. In this section, I describe the experimental implementation of the idea to image several structures with slightly different resonance conditions in the same FOV.

To increase the tolerance of the sensor, the most obvious approach is to use tuned structures with slightly different grating periods, because the resonance wavelength depends linearly on the grating period (see Fig. 15 B) and the Q-factor and therefore the phase sensitivity does not change significantly when altering the period, since the effective index of the mode does not depend on the period, but rather on the filling-factor. To guarantee a close proximity of sensitivity while also increasing fabrication tolerance, I alter the grating period between adjacent gratings by 1 nm (Fig. 40), which is the minimum of the achievable electron beam lithography resolution (see Appendix 8.2.1 for detailed fabrication methods). As visible in Figure 40, two grating structures with a 1 nm period difference correspond to consecutive phase curves. While this approach increases the fabrication tolerance such that one of the gratings in the 5 nm period range resonates for every sensor fabrication, it is also clear that it does not enable to probe several points of the phase curve simultaneously because a 1 nm difference in period corresponds to a 1.4 nm change in resonance wavelength and the FWHM of the TM mode is ≈0.8 nm (see Fig. 26).

An alternative approach is therefore to tune the filling-factor of the grating instead of the grating period. The filling-factor can be finely tuned by varying the electron beam exposure dose because a higher dose leads to a higher degree of electron scattering in the resist and thus to a larger exposure area, which corresponds to a reduction of the FF. The advantage of tuning the FF instead of the period is the higher accuracy of the resulting resonance wavelength steps [42]. I validated this experimentally by measuring the phase response of two different gratings which were exposed with a difference in dose of 0.05 μC/cm^2 (see Fig. 41). The corresponding phase curves overlap spectrally such that the single laser diode wavelength can probe more than one point of the phase curve simultaneously when the index is altered. This can be useful to guarantee a measurement at the point of highest phase sensitivity in a setting where the incidence angle cannot be finely tuned to align with the maximum phase sensitivity of a single structure. Nevertheless, the non-linear dependence of the resonance wavelength on the FF and the dependence of the Q-factor on the FF (see Fig. 15) suggests that the tuning of the FF cannot provide fabrication tolerance without changing the phase sensitivity. As a discussion of future possibilities, in the following I argue in favour of a combination of period and FF tuning for an extended refractive index dynamic range.

The grating period variation for an extended dynamic range provides a resonance wavelength compensation, meaning that at the single laser wavelength, an increase in refractive index leads to a resonance of structures with lower grating periods. Since the refractive index – resonance wavelength dependence as well as the period – resonance wavelength dependence is approximately linear, this compensation is straightforward. Nevertheless, a period variation is not able to compensate for the change in spectral characteristics of the resonance when increasing the refractive index. This can be achieved by a combined period and filling-factor variation. As an example based on simulations, a change in refractive index of $\Delta n = 0.03$ would lead to an approximate FWHM decrease of 0.2 nm, corresponding to a 40% increase in phase sensitivity. Since a period variation does not influence the phase sensitivity of the resonant mode, this would thus lead to a non-linear dynamic range. Instead, the same phase sensitivity can be achieved for the same index change, if the filling-factor is reduced from 80% to 74% while the period is reduced by only 1 nm to ensure the same resonance wavelength. In this manner, a dynamic range with constant phase sensitivity can be realised if the application requires a quantification of biomaterial on the surface over a refractive index range which exceeds the range of a single structure.

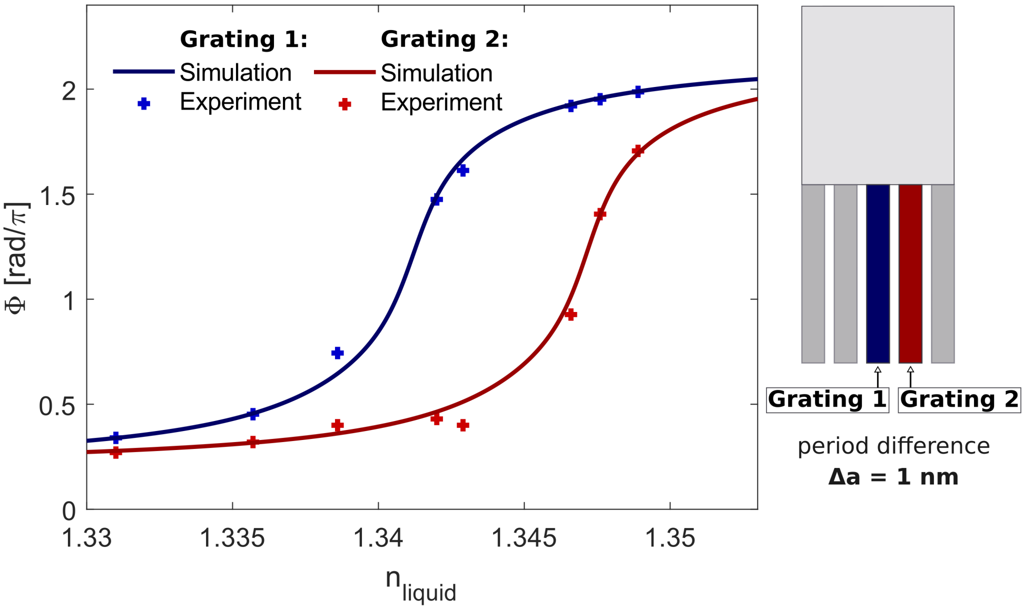

Figure 40: Phase response measured upon introduction of glucose solution of calibrated refracted index. The figure shows the phase response of two adjacent gratings with 1 nm difference in grating period. The standard deviation of Φ over time, which is the data that the graph is based on, while flowing the glucose solutions is smaller than the marker size. The bulk refractive index is calibrated by measuring the refractive index of glucose solutions with a refractometer. The two grating structures are introduced to the same glucose solutions at the same time. The response is referenced with the microfluidic referencing system.

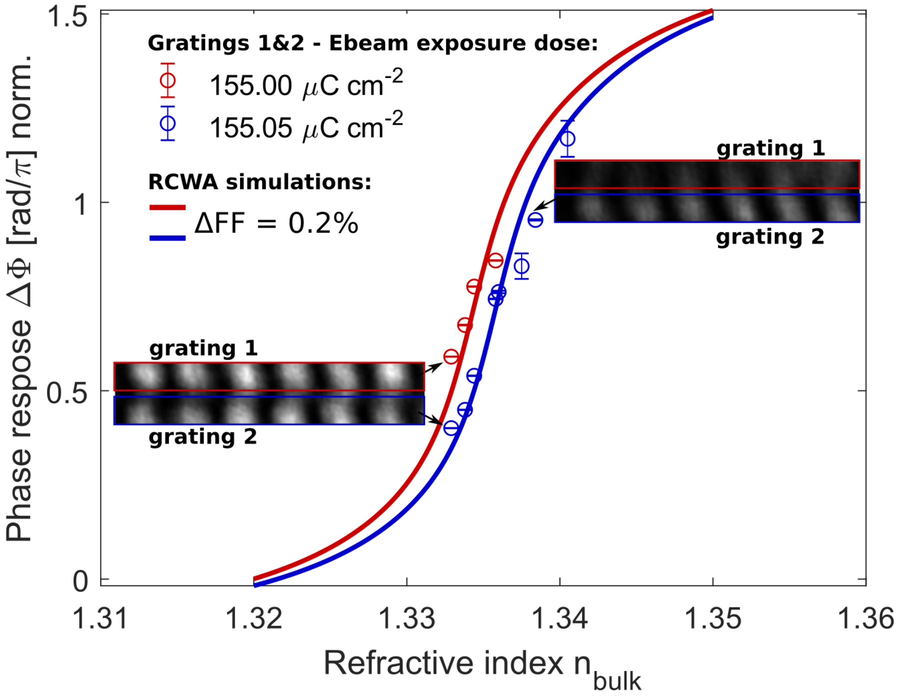

Figure 41: Measured phase response of two different grating structures, which were fabricated using a difference in electron beam lithography dose factor of 0.05 μC/cm^2. The errorbars correspond to the standard deviation σ of the phase response over time while flowing each glucose solution. Calibration and experimental details as described in caption of Fig. 40.

4.3 Discussion

To finalise this section on the sensing performance, I want to discuss the definition of LOD more critically. In some publications describing biosensing technology, the LOD does not take into account the system-noise (3σ) and instead the theoretical system-resolution is considered to estimate the smallest measurable refractive index change. Nevertheless, when LOD values are compared in the literature, this distinction is often not made, such that LOD (Eq. (35)) and resolution are considered to be the same and the performance comparison is therefore not particularly valid. For instance, the work by Sahoo et al. [48], which I mention in the introduction, takes into account the theoretical resolution of their Mach-Zehnder interferometer and the measured phase sensitivity to estimate a very low refractive index resolution of $3.43 \cdot 10^{-7}$. This value does not take into account the system-noise, which is potentially significant in an unstabilised Mach-Zehnder interferometer. Because my work is targeted at POC applications, a noise characterisation is critical to characterise and improve the performance. Therefore, I determined the LOD based on sensitivity and system-noise over a time interval of 30 minutes. It will become evident in the following section that this time interval is both necessary and sufficient, since biochemical binding in this system happens on this timescale.

As a further discussion point, I want to mention that the phase sensitivity depends on the angle of incidence and therefore also on the degree of collimation of the laser beam. A low degree of collimation would correspond to a wide spread of the k-components of the incidence beam and therefore to a non-perfect plane wave, which would broaden the resonance peak compared to the simulated peak. The close agreement between experimental and simulated phase sensitivity (Fig. 39) suggests that the setup provides a sufficiently high degree of collimation.

To test this hypothesis, I performed a measurement of the beam diameter at two dif-

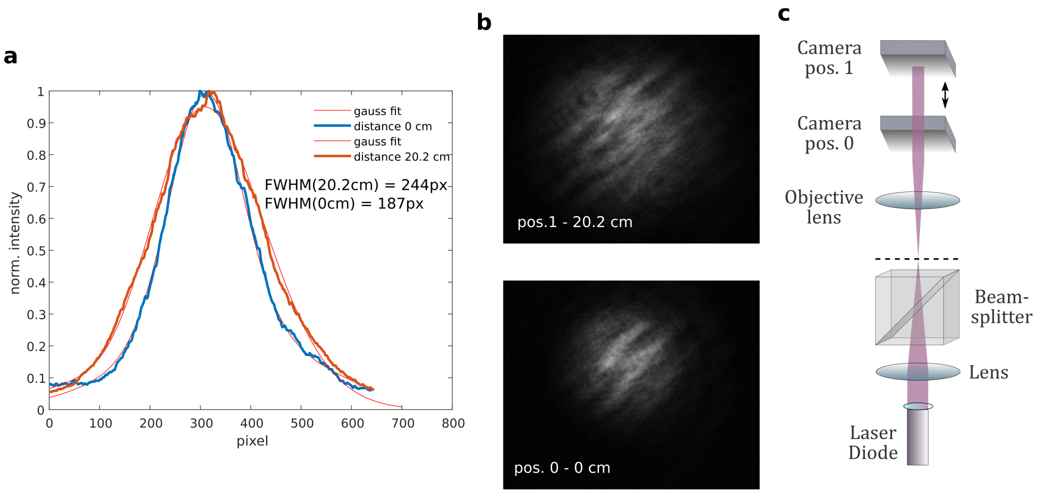

Figure 42: Divergence angle determination. **a** beam profiles at position 0 and position 0 + 20.2cm. **b** camera images of beam profile taken at different camera positions as indicated in setup schematic in **c**

ferent z-positions and calculated the corresponding angle of divergence. The beam diameter increases by $205\mu m$ over a distance of 202 mm, which corresponds to an angle of divergence of 0.03°. When comparing this value to those in the literature, it becomes evident that this is a very low degree of divergence. For example, in the supplementary information of reference [68], the authors write that their beam divergence is 0.034° and is *not* the limiting aspect of their state-of-the-art experimental Q-factors ($Q \approx 10^4$). Note that the laser diode I use is a coherent source, which facilitates focusing accurately in the back-focal-plane of the objective and therefore collimating to a higher degree than would be possible with e.g. a low coherence halogen source.

5 Experimental Protein Sensing

5.1 Principle of photonic protein sensing

The principle of protein detection based on refractive index sensing relies on specific surface chemistry that allows the target proteins to bind onto the surface and within the mode volume of the photonic structure, which alters the effective index of the mode. Quantitative mass imaging of single biological macromolecules shows that proteins all have basically the same refractive index of $\approx$1.59 (Fig. S1 in [78]), but they vary in size from large proteins like antibodies ($\approx$ 150 kDa) to smaller proteins as, e.g., procalcitonin ($\approx$ 13 kDa).

As motivated in the beginning of this work, the final goal is to measure specific proteins or molecules and to decrease the limit of detection to as low concentrations of proteins and as small proteins as possible. Since the sensor is a refractive index sensor, pushing the limits of protein concentrations is almost equivalent to also pushing the lower limit of the size of detectable proteins. These goals are *almost* equivalent, because even though both, sensing low concentrations and sensing small proteins, profit from high sensitivity, the surface chemistry dependence on large antibodies renders these goals not exactly equivalent thus requiring different optimisation strategies, as will become evident later on.

5.2 Specificity

Specificity is an essential requirement of protein sensing because diagnostics are performed using patient samples, meaning highly complex matrices containing a variety of proteins which are present in bodily fluids such as blood, urine, or saliva. The usage of antibodies is the most common approach to achieving specificity, since they are proteins produced by the immune system of all animals to fight unwanted components entering the body, for example pathogens like viruses and bacteria. Antibodies are produced specifically to bind only to the target proteins, e.g. on a pathogen cell membrane. The proteins, which are indicators of specific diseases, are called biomarkers. Antibodies can be extracted from a host animal and immobilised on our sensor's surfaces; the corresponding surface chemistry ensures that only the target protein binds to the antibodies and none of the other proteins of the matrix do. A related aspect of specificity is to prevent the other proteins from binding to the sensor surface in other ways, i.e. non-specific binding. Therefore, the following two aspects are considered for specific biomarker detection:

1. immobilisation of a **specific capture molecule** (e.g. antibody) which only the target molecule (e.g. biomarker) can bind to
2. **blocking** of any non-specific binding sites on the surface around the antibody to avoid false positives

There are a variety of approaches available to achieve surface functionalisation. The protocol I used was developed and optimised in our group [51]. The special aspect of this approach is to use a Polyethylene glycol (PEG) monolayer between the surface and the antibody which serves both as means to immobilise the antibodies and as a blocking agent once the antibodies are immobilised (see Appendix 8.2.3 for details).

5.3 Procalcitonin sensing experiments

5.3.1 Interferometric procalcitonin sensing experiments

To characterise the protein detection performance, I used procalcitonin (PCT), which is synthesised in the human body in response to the invasion of pathogenic bacteria. PCT has been recognised as an early and specific indicator for bacterial infection, which renders it clinically relevant. As PCT can differentiate between bacterial and viral infections, it has the potential to inform the appropriate use of antibiotics. Despite being

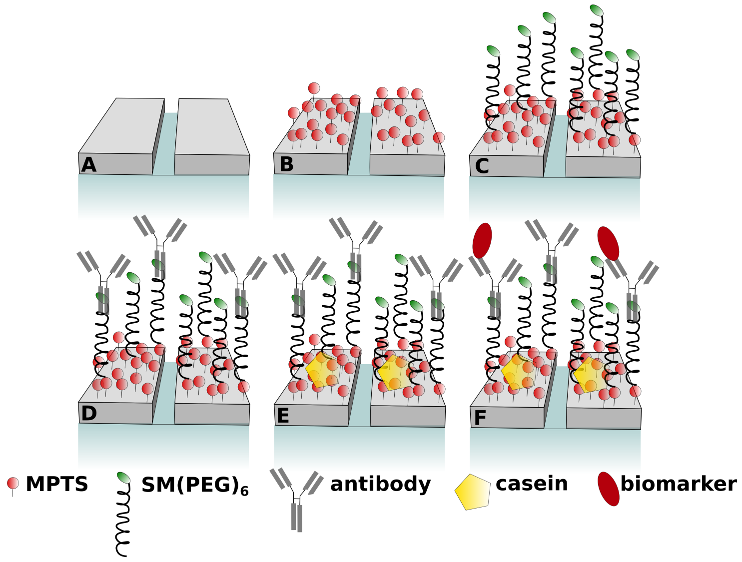

Figure 43: Schematic of surface functionalisation steps (not to scale). **A** the bare sensor is cleaned either using Piranha or ozone cleaning (see Appendix 8.2.3) to introduce hydroxyl groups on the surface which allows **B** MPTS to form a monolayer on the surface. This MPTS step is called silanisation, during which covalent -Si-O-Si- bonds are formed. **C** SM(PEG)$_6$ binds to the MPTS and forms another monolayer to which **D** any antibody can bind. **E** Casein is a blocking buffer and binds to any remaining non-specific binding sites on the surface. **F** the target antigen then binds to the specifically chosen antibody.

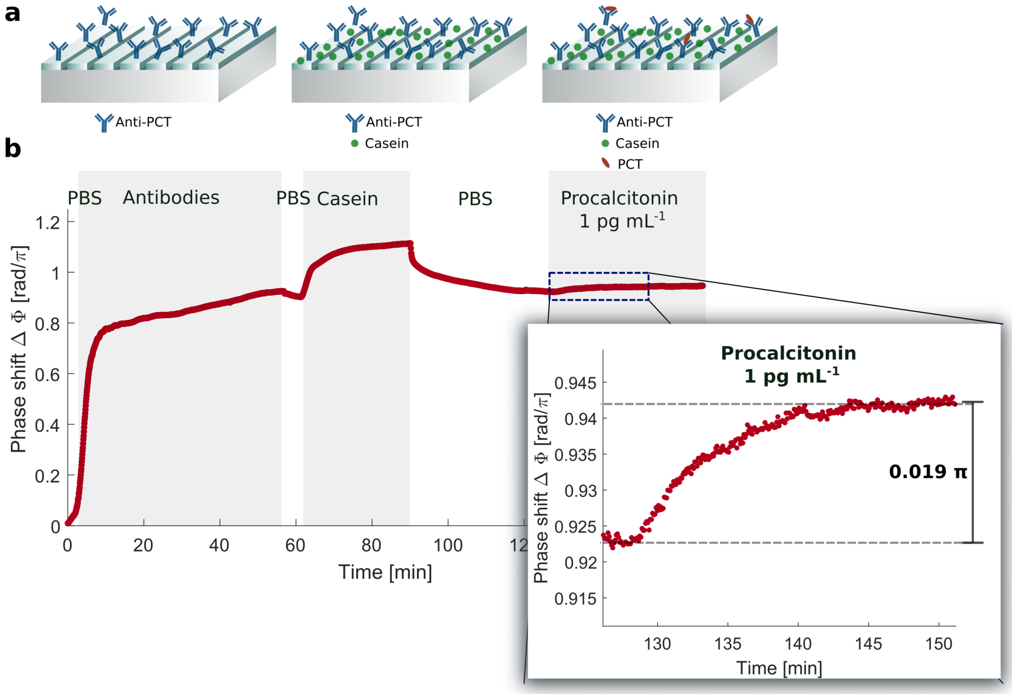

Figure 44: **a**, Schematic of functionalisation steps and the corresponding phase shift observed experimentally in **b**, Anti-PCT antibodies (50 µg mL^{-1}) are binding to the PEG spacer layer (see methods appendix 8.2.3). After saturating the surface, casein is introduced to block any remaining non-specific binding sites. The following PBS washing results in most of the casein being washed away suggesting the PEG layer is already blocking the surface effectively. We observe a 0.019 π phase shift in equilibrium for a procalcitonin concentration of 1 pg mL^{-1}.

a promising biomarker, PCT is not used widely in label-free POC devices because it occurs at low concentrations and is relatively small (13 kDa). A potential POC device for PCT needs to provide an LOD of tens of pg mL^{-1}, which is challenging, especially for label-free detection. ELISA, the ‘gold standard’ technology, provides a limit of detection for PCT sensing of approximately 15 pg mL^{-1} [79].

Figure 44 shows a complete PCT sensing experiment. The first curve of the initial ≈ 60 minutes corresponds to the antibodies binding to the PEG layer (methods in Appendix 8.2.3). After washing with PBS, casein is introduced as a blocking buffer after which

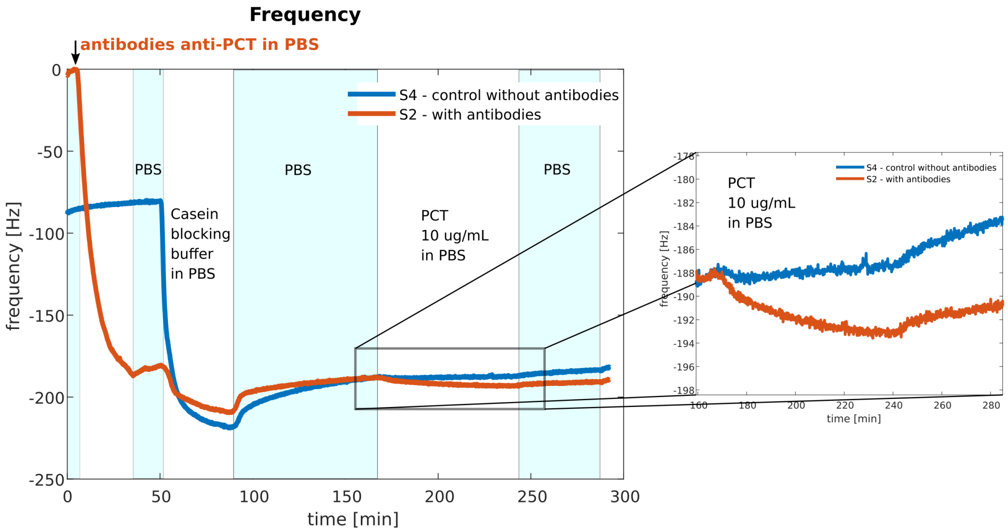

Figure 45: PCT control sensing with a commercial Quartz-crystal-microbalance (Biolin Scientific, Qsense Analyzer) instrument. Note that, unlike in the photonic measurement, mass binding registers as a reduction of the resonance value. The anti-PCT antibody concentration is the same as for the measurement shown in Fig. 44, $50\,\mu\mathrm{g\,mL^{-1}}$. The experiments are performed at room temperature and the microfluidic pump speed is $20\,\mu\mathrm{L\,min^{-1}}$, which are the same parameters as for the photonic sensing experiments.

any non-specific binding sites, that the PEG is not sufficiently protecting, are blocked from non-specific adsorption of proteins. The PEG is hydrolysed at this point, which means there is no expected binding of proteins to the PEG itself after the antibody immobilisation [51].

After washing for half an hour, the PBS baseline is stable and PCT is introduced to the surface at a concentration of $1\,\mathrm{pg\,mL^{-1}}$ in PBS, which produces a binding curve saturating at approximately 0.02π, a value above the noise level of $5.4{\cdot}10^{-4}\pi$ (see Section 4.2.2).

5.3.2 Procalcitonin control experiments

Figure 45 shows a control experiment using a quartz-crystal-microbalance (QCM-D) with two different channels, i.e. a signal channel with anti-PCT antibodies and a refer-

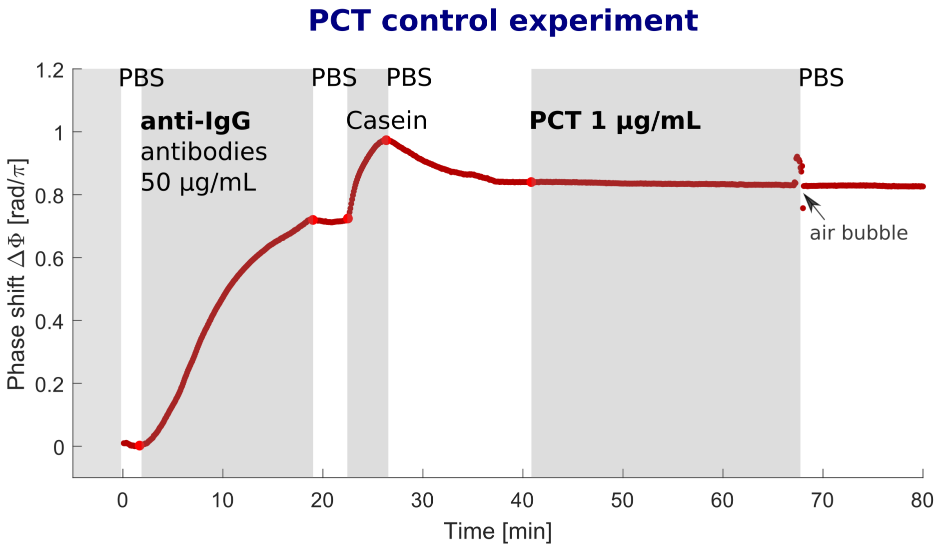

Figure 46: Procalcitonin sensing with non-specific antibodies as control experiment. The antibodies are specific to immunoglobulin G (anti-IgG antibodies, R2004 Sigma Aldrich). The rest of the experimental details are identical to the previously discussed experiment shown in Fig. 44 with the difference that a higher PCT concentration is chosen to test the specificity at concentrations that are far from the LOD.

ence channel without. No specific binding of PCT in the reference is expected, so any shift that is observed in this channel is likely due to non-specific binding. Due to the small size of the PCT molecule, the detection is challenging for a QCM-D approach, but nevertheless a change in frequency is observed in the signal channel. There is a considerably smaller shift for PCT in the reference channel, which indicates that there is possibly a certain low degree of non-specific binding in this case. In a final POC device, a biochemical reference channel needs to be included into every experiment so that the effective resonance response can be measured by subtracting the reference channel (non-specific antibody) from the signal channel (specific antibody).

An example of such a photonic control experiment is plotted in Figure 46, where I was flowing a control antibody, which is not specific to PCT. Antibodies that would bind to immunoglobulin G (IgG) are chosen because they are often used in sensing experiments and therefore readily available. Figure 46 shows a binding curve for these antibodies followed by a short introduction of the blocking buffer casein, as discussed before, and a long washing step with PBS. Introducing PCT at the relatively high concentration of 1 μg mL^{-1} does not result in any effective shift in the phase response. In conclusion, the surface chemistry is shown to prevent non-specific binding and fouling of PCT with the photonic Si_3N_4 sensors, which in turn allows to conclude that the observed phase shifts for PCT in channels that were functionalised with anti-PCT antibodies is specific.

Discussion

The above shown PCT sensing experiments are to be seen as preliminary results. A variety of further experiments would strengthen the evaluation of the sensing performance. For example, higher concentrations of PCT should be detected in the future to gain information regarding the dynamic range and to extract the dissociation constant. Moreover, further control experiments should be performed in addition to the ones shown above to quantify the degree of reliability of the surface chemistry within the photonic sensing environment. The PCT sensing results at this stage should be seen as proof of concept protein sensing rather than a characterisation of the corresponding binding kinetics and other aspects of the surface chemistry. The specificity and sensitivity related to the surface chemistry has been validated extensively in our group by using the same kind of photonic structures as I am using here, but with a different, non-interferometric read-out approach showing a LOD for PCT of approximately 10 pg mL^{-1} [51].

In conclusion, the data presented in this section allows to predict an improved LOD for small proteins with an interferometric read-out compared to a non-interferometric approach.

5.4 β-Amyloid sensing experiments

To show the versatility of the sensor, I conducted another sensing investigation on a different protein in collaboration with Dr. Steven Quinn. β-amyloid are small proteins, which are aggregating in the brain in the form of plaques accompanying Alzheimer's disease (AD). Detecting early monomeric stages of β-amyloid could potentially help a future AD detection at stages where the late stages of AD could still be prevented, if a treatment were to exist. The role of these β-amyloid monomers or oligomers as biomarkers in bodily fluids such as urine or serum is not yet well established with respect to early AD diagnostics. Defining biomarkers for AD is not a straightforward endeavour because of the blood-brain barrier and yet, recent studies show the existence of potentially useful biomarkers even in the easily accessible urine matrix [80].

Biochemistry related specifics of amyloid sensing

While the general surface functionalisation protocol is described in detail in the methods (Appendix 8.2.3), there are aspects of amyloid sensing which are specific and different compared to conventional protein sensing. There are several challenges associated with amyloid sensing. The first is the size of the monomeric 'amyloid(1 - 42)', 4.5 kDa, which is even smaller than PCT (13 kDa). Since we are using antibodies to specifically detect the amyloid proteins and antibodies are considerable larger (150 kDa), this corresponds to a low density of antigens, even at high concentrations, because a limited number of protein binds to one antibody at a time.

The second challenge is related to the tendency of amyloids to form oligomers, which means that the exact state of the protein or protein aggregate is unknown. The temperature of the solution is one particular aspect of relevance to the oligomerisation rate. To avoid the clustering of the amyloids before the measurement, they are kept in the freezer at -20° and only defrosted immediately before the measurement.

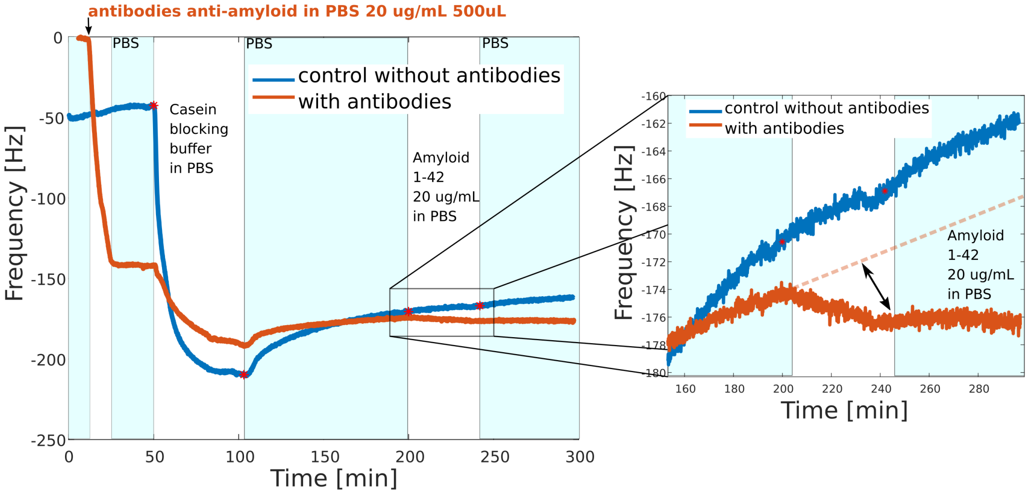

Figure 47: QCM-D amyloid sensing to test the surface functionalisation and, in particular, the specificity by flowing β-amyloid in both a signal and a reference channel, the latter without any antibodies (blue). The arrow on the right indicates the shift in the signal channel upon amyloid binding, which is non-existent in the control experiment. The drift of the system, which is extrapolated by the dashed orange line, should be taken into account when analysing this data.

5.4.1 β-Amyloid control experiments

To provide a system-independent validation of the surface chemistry for amyloid sensing, I first conducted QCM-D experiments (Fig. 47). The antibodies are evidently binding to the sensor, even if in this experiment the available volume of the antibodies was not sufficient to see a nice binding curve. The following effective shift for casein is lower in the channel with antibodies than in the channel without antibodies, which can be explained with the fact that antibodies ideally occupy most of the available binding sites. Casein then fills the remaining gaps. There is a small but evident shift in frequency upon amyloid binding and no shift is visible in the control channel without antibodies, which again validates the specificity of the surface chemistry.

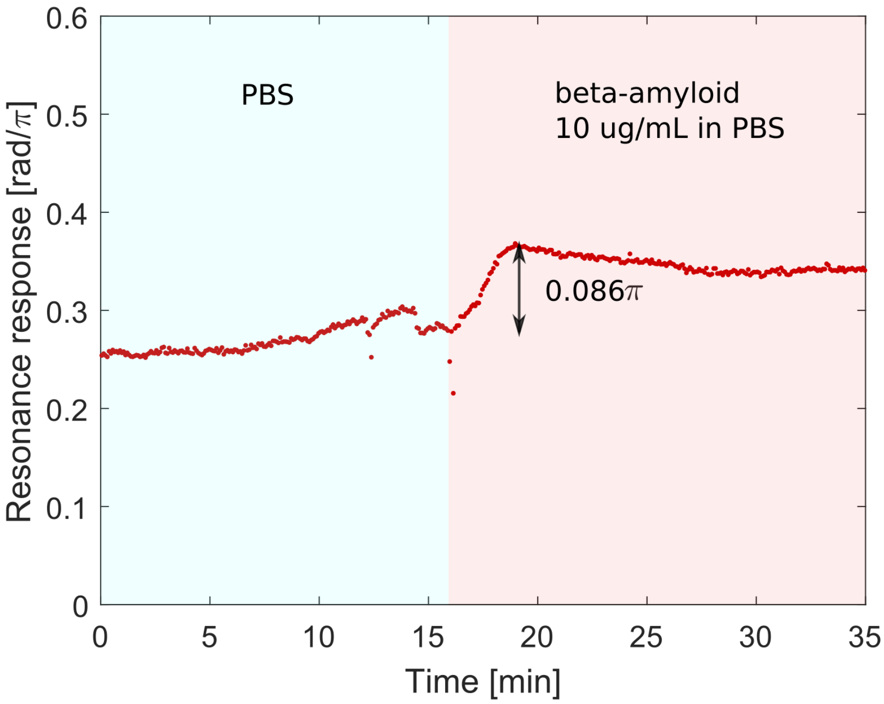

Figure 48: Interferometric amyloid sensing with 1D GMR grating

5.4.2 Interferometric β-amyloid sensing experiments

The surface chemistry used in the following photonic amyloid sensing experiment is the same as in in the QCM-D test experiments above (Fig. 47) with the only difference that the optical measurements are initiated after antibody-immobilisation and surface blocking with casein. Once the surface chemistry is confirmed and extensively tested [51], this pre-functionalisation with antibodies mimics the way a diagnostic device would operate. Here, the pre-functionalisation with antibodies also has the advantage of avoiding any time delay after introducing the PEG-layer to aqueous solution, which initiates the hydrolysis of the PEG, to ensure that a high antibody coverage can be achieved before the PEG is completely hydrolysed and solely acts as a surface blocking agent.

Discussion

While the above results are promising and the QCM-D experiments show that the chemistry is working for amyloid sensing, these results have to be seen as preliminary. The next steps will be to repeat the above measurement several times more to establish the degree of reliability which in this amyloid-case is more critical due to the added uncertainty introduced by oligomerisation. Observing the oligomerisation in real-time [81] could be enabled by these measurements as well, if the measurement time was increased to give the monomers time to aggregate and form oligomers on the sensor surface. These reactions would be detected as slow phase drifts corresponding to an increase in refractive index upon oligomerisation.

Moreover, the LOD for monomeric β-amyloid will be determined in future experiments to characterise the potential applicability for diagnostics and compare the sensitivity to other techniques.

6 Outlook: Preliminary Results of Ongoing Projects

The realisation of a photonic device based on common-path interferometry is driven by the necessity to develop high-performance and cost-efficient POC instruments for biomedical applications. On the path towards this goal, several further challenges need to be met and the following outlook gives a summary of my current progress in addressing, for example, the need for the miniaturisation of the optical setup, protein detection in complex matrices such as serum and the prospect of photonic modes providing potentially increased phase sensitivity by increasing the Q-factor and the surface sensitivity.

6.1 Interferometric sensing with dielectric nanohole arrays and visible light

An important advantage of the common-path approach using a Wollaston prism as shearing component (Fig. 28) is that it can be applied to two-dimensional photonic nanostructures as well as the one-dimensional gratings that were discussed previously. A resonant structure with two-dimensional periodicity is polarisation insensitive, which suggests that using the interference of orthogonally polarised light generated by the Wollaston prism would be ineffective in measuring phase differences.

When using the spatial mode overlap approach, however, two different modes can be excited in adjacent structures. Since these modes are both excited with un-polarised light, the Wollaston prism creates two beams with identical information. When the dimensions are chosen correctly, the two different modes can be overlapped in space and interfere. The Wollaston prism selects the orthogonally polarised components of each mode and the analyser creates the interferogram in the same way as it is done with a one-dimensional grating.

Figure 49 shows a raw image of resonant dielectric nanoholes in oxygen-enriched hy-

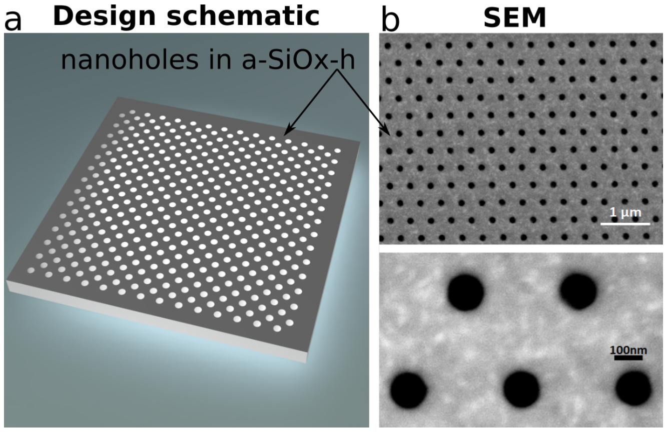

Figure 49: **a** Design of nanohole array. **b** SEM images of dielectric nanoholes. Both generated by Dr Donato Conteduca.

drogenated amorphous silicon (a-SiOx:H), which were fabricated by my colleague Dr. Donato Conteduca. These particular structures are designed to have both separate modes resonating at a wavelength of around 635 nm. Using the Wollaston prism, the reflected beam is sheared and the analyser at 45° creates the high-contrast interferogram for the several resonant structures in the FOV. Note that the fringe period (see theory in Section 2.4, Fig. 20) is a bit smaller compared to the previous studies because of the lower wavelength (635 nm compared to 855 nm).

The motivation for exploring these novel photonic nanostructures [53] and combining them with interferometry lies in several aspects. First, it adds versatility to the interferometric approach to be able to apply the phase read-out to two dimensional structures, because many sensors are based on them, e.g. 2D photonic crystal slabs [82]. Secondly, using higher-index materials increases the mode confinement close to the surface and therefore the surface sensitivity. The Q-factor of these preliminary modes (see Fig. 50) is unsurprisingly not as high as in the case of the TM mode of the 1-D Si_3N_4 grating used before, exactly because of the high index contrast and the lower wavelength for which they are designed to resonate. To explore this further, a combination with alternative symmetry protected high-Q resonances as described in

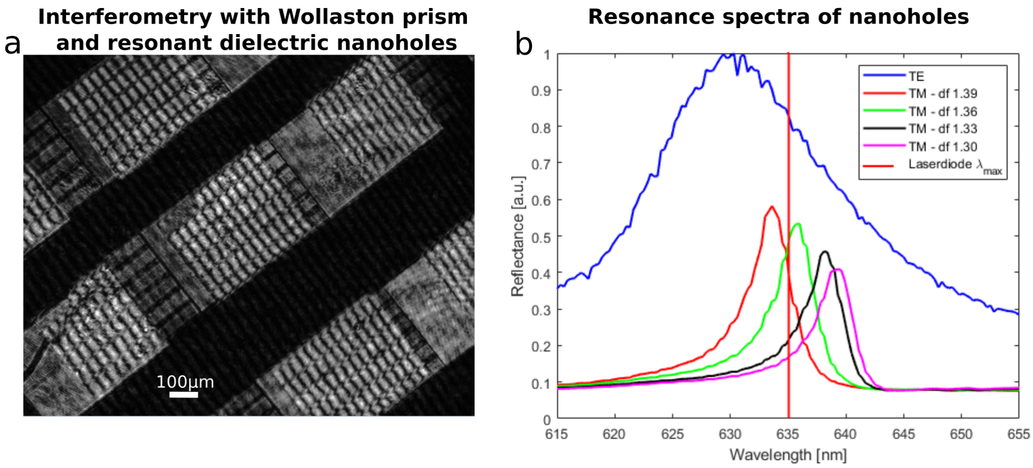

Figure 50: Interferometry with dielectric nanoholes in hydrogenated, amorphous silicon instead of silicon nitride fabricated by Dr. Donato Conteduca. The interferogram is created by means of the Wollaston prism as in Figure 28. The difference between this structure and the one-dimensional structures above is not only the two-dimensional periodicity of the nanoholes and the material with higher refractive index but also the choice of resonance wavelength, which here in this image is 635 nm. **a** Interferogram showing several stripes resonating for the 'TM'-mode and a single structure each resonating for the 'TE'-mode. **b** - Spectra of TE and TM modes of dielectric nanoholes resonating around the laser wavelength (red line). The spectra were recorded by Dr. Donato Conteduca.

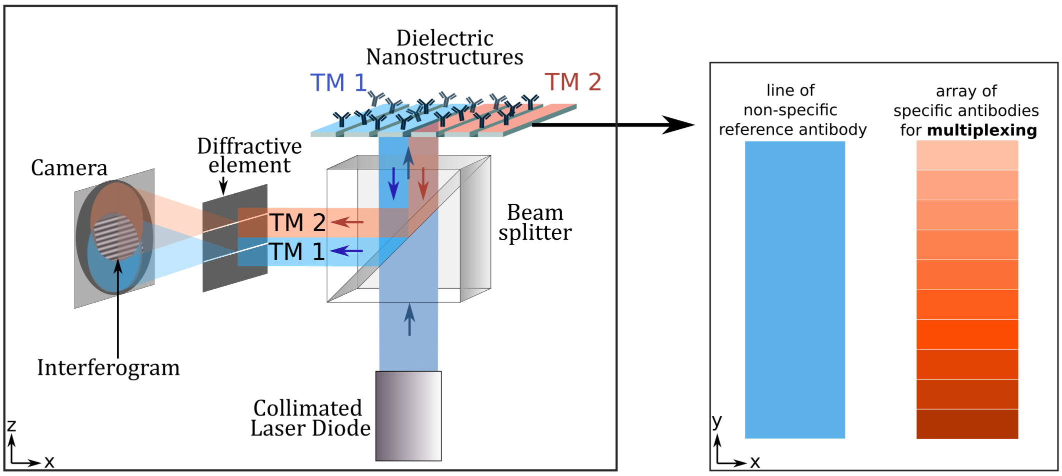

Figure 51: Schematic of a miniaturised lensless optical setup using a double slit as diffractive element to replace the Wollaston prism. The light of a collimated laser diode module is used to excite a TM resonance in the GMR sensor. The only difference between TM 1 and TM 2 is their separation by a microfluidic system and their functionalisation. Therefore, TM 1 is a resonant structure operating in channel 1 while the photonically identical TM 2 structure operates in channel 2. The reflected light from each of these channels is then each aligned with a slit such that the interferogram contains information about the relative phase changes between the two channels. This system, as such, is a self-referencing system.

Section 6.4 could be considered.

6.2 Miniaturised interferometric setup for point-of-care device prototype

Spatial mode overlap without Wollaston prism

The Wollaston prism has a certain size and cost and these factors are currently not easily scalable. It is therefore worth investigating alternative means for realising common-path interferometry which would allow a reduction of cost and size for a miniaturised POC device.

One idea is to replace the Wollaston prism with a simpler diffractive element, which can generate a shear between reference and signal beam by other means than birefrin-

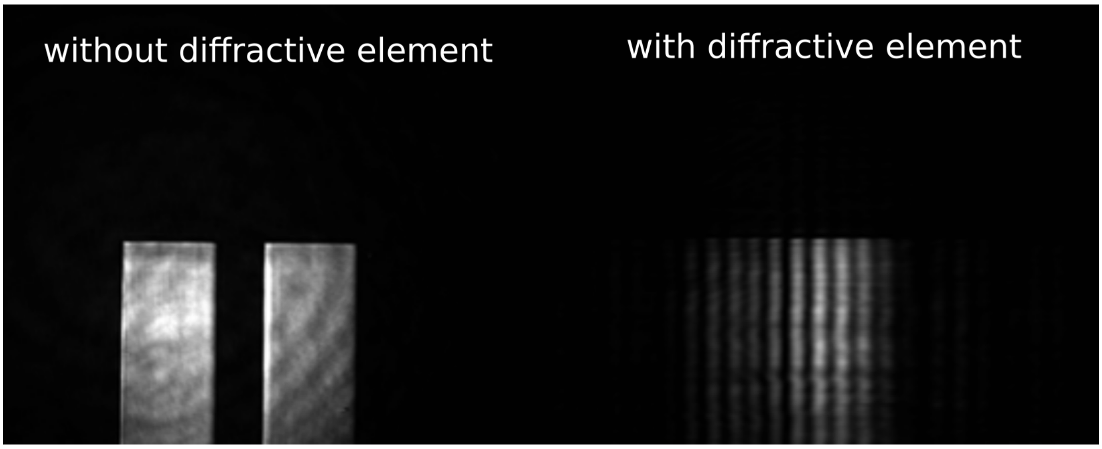

Figure 52: Raw images demonstrating sensing with a double slit as the diffractive element. On the left, two identical gratings are on resonance and are imaged. On the right, a double slit is aligned with the same gratings such that the light from each grating falls onto one slit only, thereby being able to interfere in the camera plane. The method is based on the well-known Young's slit interference experiment. The images are meant to illustrate the working principle only.

gence. Such a very simple diffractive element is, for example, a double slit which is aligned to two different parts of the resonantly reflected beam.

For a proof-of-principle, I first replaced the Wollaston prism in the bulk setup (Fig. 21) with a double slit of distance $g = 300\,\mu m$ and width $b = 100\,\mu m$ (3B Scientific Diaphragm with 3 Double Slits of Different Widths). Figure 52 shows the resonant excitation of two separate gratings (here using TE polarisation for illustration) with the usual 855 nm laser diode. The grating stripes are then each aligned with one of the slits (compare to Fig. 51) and the resulting interferogram can be seen on the right of Figure 52.

To indicate the refractive index sensing capability of the double slit read-out, Figure 53 shows the measured phase response over time. The initial value corresponds to a deionised water drop on the surface of the sensor and the phase step corresponds to adding a small drop of IPA to this water drop. Since the goal of this experiment is a simple verification of the double-slit read-out principle, refractive index quantifica-

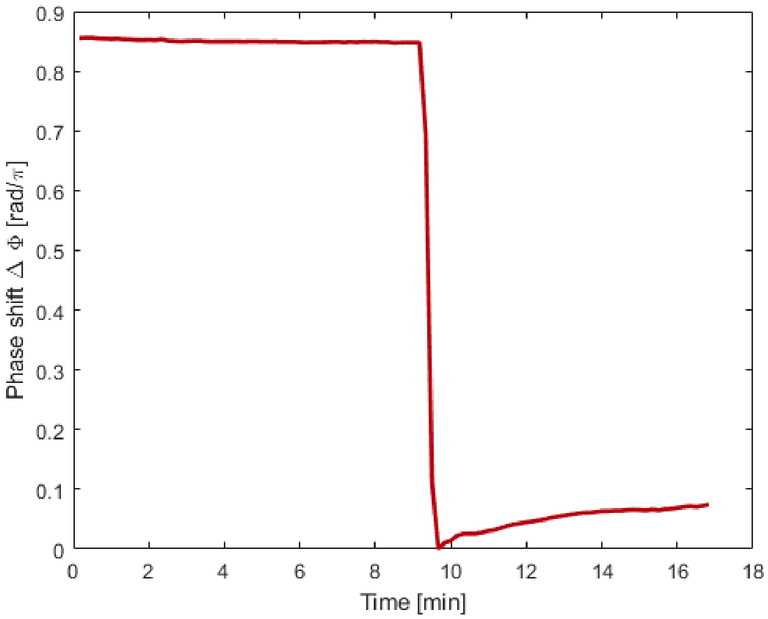

Figure 53: Refractive index sensing with double-slit read-out in bulk setup for proof-of-principle. The jump in phase corresponds to dropping a small drop of IPA onto the initial water drop which increases the refractive index by an unknown amount. Quantification is not the goal of this test experiment, its purpose is solely to verify the operation of the interferometer with a double slit.

tion is not aimed for here. Note the flat curve in the beginning of the experiment in comparison to the drift in the curve after adding the IPA drop. This can be explained by diffusion of IPA through the water. The initial drop value corresponds to the IPA being forced onto the surface and the drift to a lower average corresponds to the IPA diffusing away from the surface and mixing with the water, which reduces the effective refractive index of the initial drop.

Miniaturised setup - dimensions and distances

The parameters of the double slit need to be carefully considered for the miniaturised setup, because there are several aspects (theoretical and practical) influencing the design realisability:

1. diffracted light needs to overlap in the camera plane ⇒ slits need to be small enough to create large enough angles for a given distance between slits and camera
2. distance between slits and camera cannot be arbitrarily small because of the requirement of printed components and holder footprints and cannot be arbitrarily large because we want a small device
3. the intensity transmitted through the slits needs to be sufficient ⇒ slits cannot be arbitrarily narrow
4. the smaller the slits the smaller the interferogram period ⇒ the minimum fringe period with respect to the camera pixel size needs to be considered
5. alignment of gratings with slits to avoid crosstalk between two modes ⇒ slit distance cannot be too small

In collaboration with Alexander Drayton from my group, who already designed and printed a miniaturised setup for the chirped grating sensing approach during his PhD

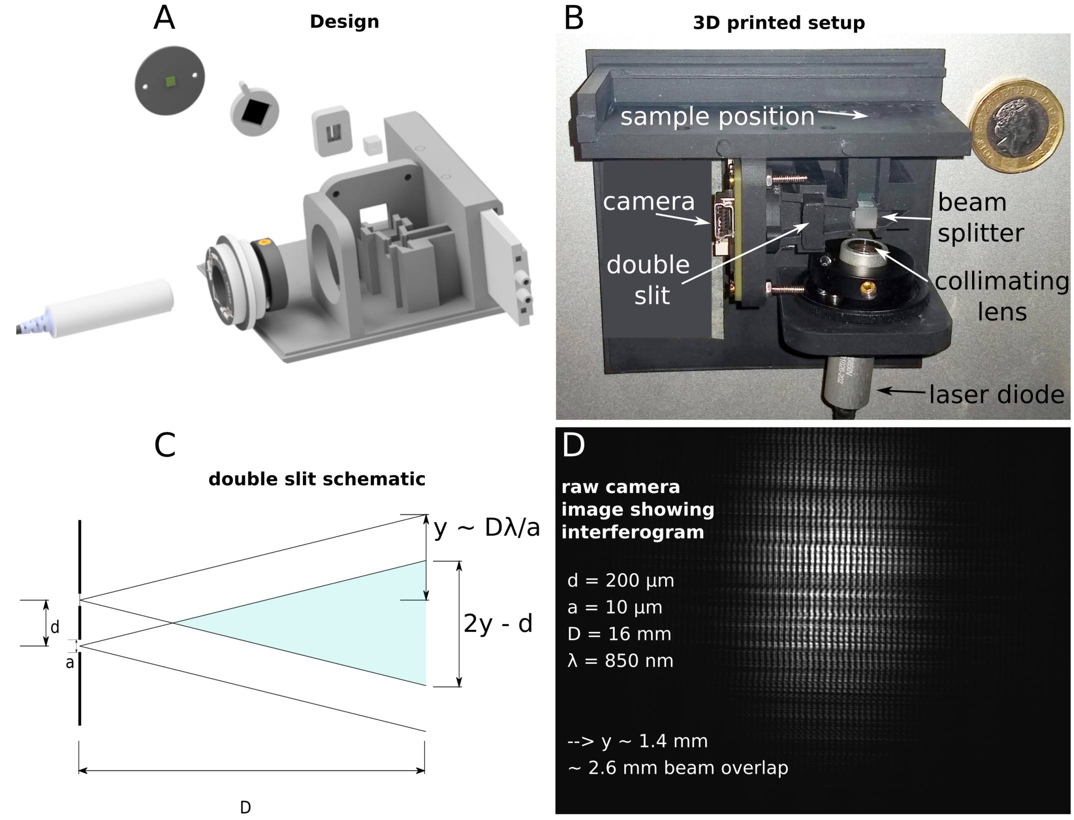

Figure 54: Consideration with respect to double slit distance, width and camera distance. On the right: corresponding interferogram recorded in the miniaturised setup. Design figure in A by Alexander Drayton.

[83], we designed a 3D-printed miniaturised interferometric setup based on Figure 51. According to the considerations above, a reasonable distance between slits and camera is $\approx 16\,\text{mm}$. Based on this restriction, calculations show (Fig. 54) that slit widths of $10\,\mu\text{m}$ at a distance of $200\,\mu\text{m}$ would give an overlap of 2.6 mm and approximately 15 camera pixels per fringe period. Based on these considerations I implemented specially designed double slits (Premium grade High Resolution Film Photomasks from Micro Lithography Services Limited).

First experimental data taken in this miniaturised setup are presented in Figure 54. These results are currently at a proof-of-principle stage and the next step will be to integrate the microfluidic system with the sensors into the miniaturised setup and determine the LOD both for bulk refractive index and biosensing.

A slightly different idea is to remove any external diffracting element and use the nanostructure itself both as sensor as well as diffracting element in a lens-free setup. This idea is at a very initial stage and could also be pursued as one of the simplest possible implementations of miniaturised, resonant interferometric sensing.

6.3 Protein sensing in serum experiments

In collaboration with Dr. Donato Conteduca, we carried out protein sensing in serum to test the surface chemistry with respect to specificity. We used undiluted fetal bovine serum (FBS), spiked with IgG, as a proxy for human serum [84]. For these measurements, we used a chirped GMR on a 2D array of nanoholes, i.e. a non-interferometric approach. The principle of chirping the nanohole array in one dimension is the same as described in references [42, 51].

We then excite the sensor with a single wavelength of a filtered halogen source and track the spatially distributed resonance peak by taking camera images as described in detail in [42, 51, 53]. The surface functionalisation protocol used for the measurement in Figure 55 is almost the same as described previously and in detail in Appendix 8.2.3.

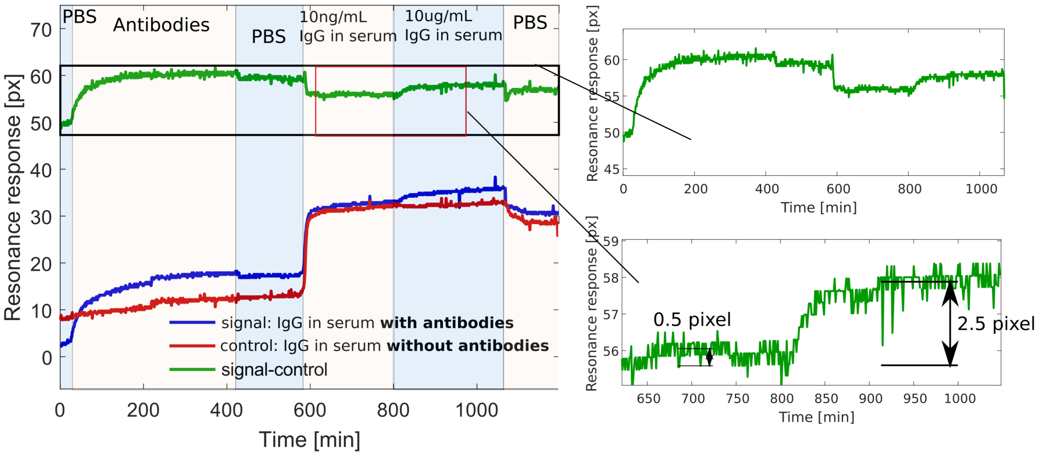

Figure 55: IgG sensing in serum using a chirped GMR sensor (no interferometry).

The only difference is that in this case I refrained from using the additional casein blocking buffer because of the implementation of a biochemical reference. I here used the reference not only for drift elimination but also as biochemical reference. This kind of control experiment can be implemented by only flowing the specific antibody (here anti-IgG) in one channel and flowing the antigen (here IgG) in both channels. Any binding that occurs in the channel without antibodies (red curve in Fig. 55) is non-specific since there is no specific antibody present. As visible in Figure 55, the red curve stays flat when introducing the IgG spiked serum while the blue curve (which has the antibody) shows a binding curve. Note that the overall shifts are relatively small for the relatively high IgG concentrations in comparison to reference [53]. It is not clear if these small shifts are related only to the chirped sensor configuration or also to the serum. There are many different proteins, salts and ions in serum [84] and their interaction might influence the binding efficiency of the IgG to anti-IgG. The slowed down kinetics because of competition with abundant serum constituents is known in literature [85] and serum is therefore often diluted.

I expect that higher shifts can be achieved by ensuring a higher antibody concentration in the evanescent field. On the other hand, the main purpose of this measurement was to confirm the suitability of the surface functionalisation protocol for measurements in a complex matrix such as serum. In particular, we wanted to test whether the PEG layer, which after hydrolysis acts as a blocking layer, successfully avoids non-specific protein adsorption on the surface. Non-specific adsorption is a major issue in a complex matrix such as serum, which is more complex than e.g. urine. Measurements in urine have already been demonstrated by our group in detail (see reference [51]). The low degree of non-specificity observed in these measurements can in part be contributed to low charge effects for example compared to gold-based sensors [86], while the positive anti-fouling effect of PEG has also been recognised previously [87]. These results will be developed further and tested repeatedly in the future with the interferometric read-out approach.

6.4 Alternative high-Q modes for phase sensitivity improvement

There are several potential routes to further increase the phase sensitivity. While the phase sensitivity of the TM mode can be improved both by increasing the angle of incidence or by increasing the filling factor, these are in practice not easily achievable because of fabrication or setup limitations. The grating groove's size cannot be arbitrarily reduced because the RIE etching process gives a practical limit to the achievable aspect ratios. The incidence angle cannot be arbitrarily high for practical reasons, at least in current setups, and because the reflectance of the TM mode is reduced with higher angles as well. Moreover, the reflectance of the TM mode is affected more by scattering losses than modes which are more strongly confined in the core of the waveguide because the TM mode has a higher degree of overlap with the rougher surface (see Fig. 56 b). The main limitation regarding an increase in Q-factor, and therefore phase sensitivity, is the correlated reduction of reflectance associated with high-Q modes in the presence of loss. Even though a reduction in reflectance is expected for every experimental high-Q mode, some modes may be less affected by non-radiative decay than others.

This outlook section aims to introduce preliminary design and experimental results regarding symmetry protected quasi-bound states in the continuum in one-dimensional Si_3N_4-gratings (see Section 2.2.7 for terminology explanation).

As already discussed in the theory section (see Fig. 10), in addition to the even modes, which can couple to the continuum of radiation at the Γ-point ($\theta = 0$), there exist odd modes where the coupling is prohibited due to the symmetry incompatibility between resonant mode confinement and radiative background. Introducing a non-zero incidence angle enables these modes to couple because the perfect symmetry of the field is broken. The Q-factor at the Γ-point is infinite in theory because the prohibition of coupling to radiation means that the light is trapped in the photonic structure for an infinite time, which per definition (see Section 2.3.1) is related to an infinite Q-factor. The higher the incidence angle, the less symmetric the mode becomes which is accompanied by a reduction of the Q-factor. A more detailed theoretical explanation is beyond the scope of this outlook, so I refer the interested reader to references [62, 68, 70, 88, 89].

The goal is to fabricate the simulated structures shown in Figure 56. An initial approach to finding the correct grating parameters for a mode to overlap with the laser diode wavelength of 855 nm is to implement a chirped grating. As mentioned before, a chirped grating is a structure with a continuously increasing period in the direction of the grating grooves. In this particular example I varied the grating period horizontally (see schematic in Fig. 57 on the right), which results in a vertically extended 'resonance line' in those grating areas in which the period matches the resonance condition. The initial results show that the high-Q odd modes close to the Γ-point may provide higher Q-factor as well as higher reflectance than the TM mode, which in turn corresponds to a higher phase sensitivity.

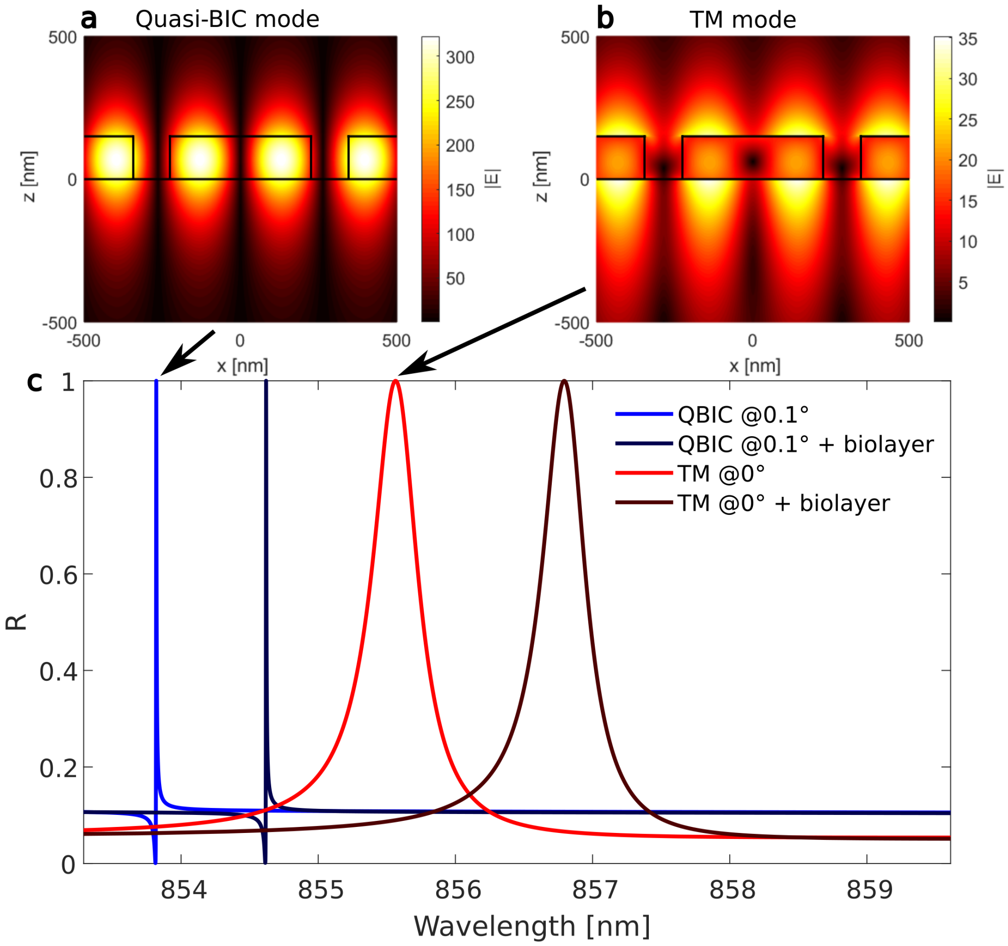

Figure 56: Simulations showing a symmetry protected Quasi-BIC mode in **a** (compare upper band in Fig. 10), where the symmetry is broken by assuming an incidence angle of $\theta = 0.1°$ as well as **b** a typical TM mode both in the same Si_3N_4-grating with the only difference being the grating period to achieve resonances at similar wavelengths. The Quasi-BIC is based on a grating period a = 527 nm and the TM a = 570 nm both with FF = 0.8. The spectra in **c** qualitatively show the corresponding surface sensitivities by simulating the response with and without a 20 nm thick generic model layer of biomolecules of refractive index n = 1.43 on the surface of the structure.

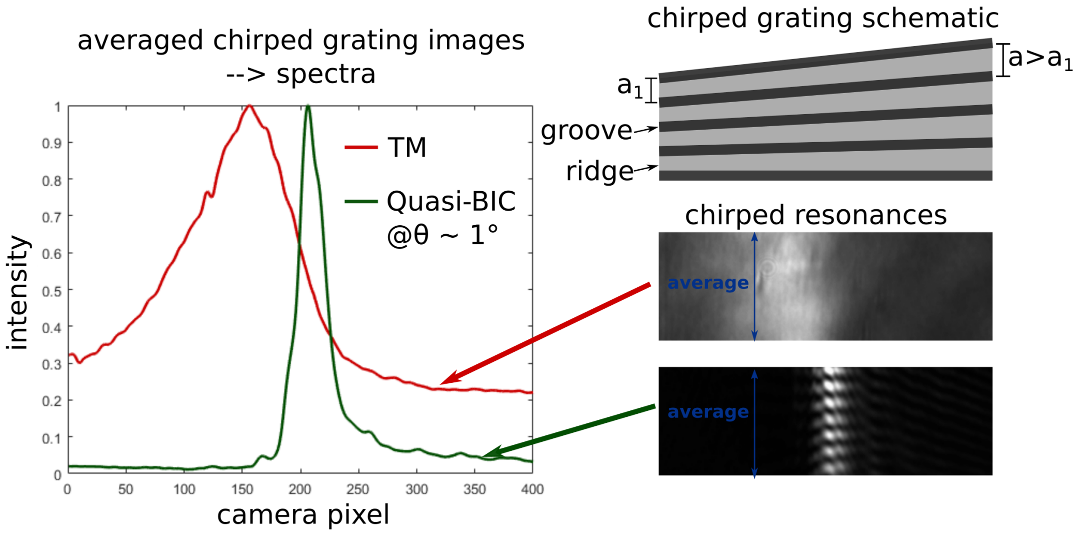

Figure 57: Red curve: TM mode spectrum obtained from a chirped grating response (upper right image) when excited with single wavelength laser diode at 855 nm. The green curve was obtained in same manner, but for a Quasi symmetry protected mode excited at the same wavelength as the TM mode in a grating with lower period at an incidence angle of $\approx 1°$. Note that the fringes visible in the bottom camera image on the right are unexpected and their origin will be part of future investigations. Those fringes were not created by means of a Wollaston prism or any other diffractive element.

Although these preliminary qualitative results are promising, further considerations will need to be taken into account for an application of these symmetry protected Quasi-BIC modes for biosensing. First, the E-field enhancement of a Quasi-BIC mode (Fig. 56 a) is almost an order of magnitude higher (here calculated at an incidence angle of 0.1°) than that of a TM mode (Fig. 56 b), which is a results of the expectedly higher lifetime of mode. For biosensing, however, the field distribution in those volumes where the biomolecules can bind to the surface determines the surface sensitivity (see Eq. (21)). As evident from Figure 56 c, adding a thin layer of biomaterial to the surface (see Fig. 18) results in a smaller shift for the Quasi-BIC (or 'near-Γ-BIC') mode compared to the TM mode, because the TM mode has a more advantageous field distribution on the surface.

Secondly, sensitivity is not the only variable of interest for applied biosensing. Reliability is of high importance as well and should be considered in the choice of the resonant mode. For example, the Q-factor and therefore phase sensitivity of the Quasi-BIC mode depends strongly on the angle of incidence, while a non-vanishing typical GMR mode shows higher Q-factor tolerance to variations of the incident angle (see Fig. 10). This could result in, maybe less sensitive, but more reliable sensing when using a TM mode rather than a Quasi-BIC mode and these points will be quantified and taken into consideration for future optimisations steps.

6.5 On 'dark modes' for surface enhanced interferometric scattering microscopy

Interferometric Scattering Microscopy (iScat) [78, 90–93] is a relatively recent technique to image, e.g., single proteins at extremely high frame-rates, which allows to extract information of binding kinetics in real-time on a single protein level. iScat relies on the contrast which is generated by coherent interference between the scat-

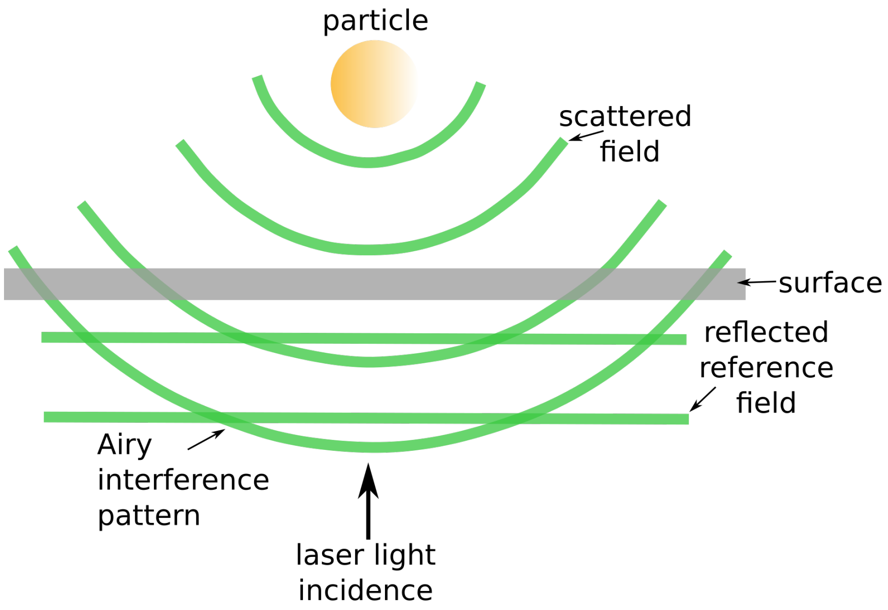

Figure 58: Interferometric Scattering Microscopy (iScat) working principle. The scattered light from the particle (e.g. protein) is interfered with a reference field, which is the light reflected from the surface-liquid interface. This superposition of a spherical scattered wave and a plane reference wave results in a characetristic Airy interference pattern where the contrast depends on the particle size and the phase depends on the particle's distances from the surface. Adapted from [92].

tered light from the protein and a background wave reflected from the surface interface where the protein is located. The intensity of the background reference beam is adjusted for example by means of numerical aperture filtering [90] to match the very low intensity coming from the protein scattered signal light.

Similar to surface enhanced fluorescence imaging or surface enhanced Raman scattering, the integration of a resonant structure could help to enhance the intensity of the scattered signal beam and therefore facilitate contrast generation and reduce background noise. The background noise would be reduced because of the localisation of the resonantly generated electromagnetic field close to the surface of the sensor.
Enhanced iScat was very recently accomplished using a resonant structure in transmission [94]. If we, however, restrict our approach to measurements in reflection to avoid

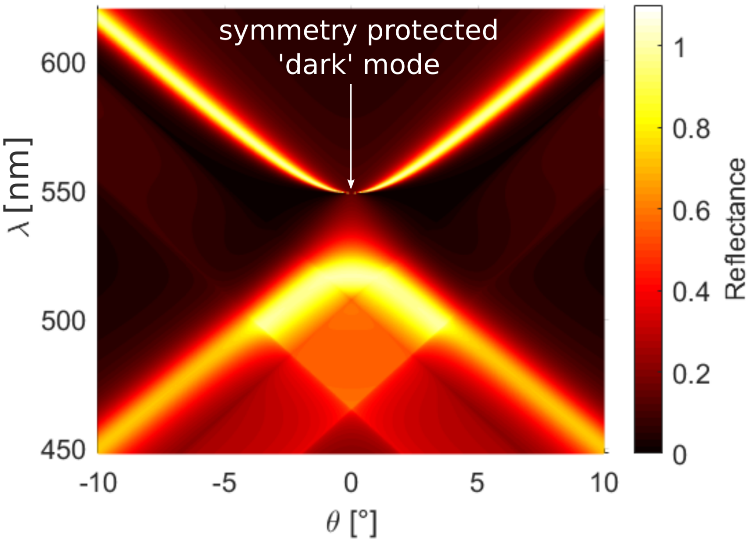

Figure 59: Dispersion diagram of TE mode in an one-dimensional grating with period a = 350 nm, thickness t = 150 nm and filling factor FF = 50%. The lower band is the even TE mode which is spectrally broad at an incidence angle $\theta = 0°$ (Γ-point) while the upper band odd mode vanishes at $\theta = 0°$ which is the symmetry protected mode discussed in this section for iScat.

noise from the microfluidics, an obvious disadvantage of using a resonant structure, even if it enhances the scattered signal, is the high reflectance which is usually associated with GMRs. The idea, which is therefore proposed here, is to use a ‘dark’ mode as discussed in the BIC-part in the end of Section 2.2. More specifically, an odd mode which is protected by symmetry around the gamma-point could be used. In theory, at zero incidence angle, the mode cannot couple to the continuum unless the symmetry is broken or non-resonant scattering is introduced. The field enhancements associated with these dark modes at near-zero incident angle are very high compared to regular leaky modes (see Fig. 60), which would mean a strong enhancement of the scattering signal. Ideally, the idea is to introduce the proteins on the sensor surface as the means to couple the symmetry protected mode to the radiation continuum. In other words, only when a protein perturbs the symmetry protected field confined on the sensor surface is the field coupled to radiation and the resonantly enhanced scattering signal is detected.

Even though these considerations are plausible in theory, the practical realisation will likely face several challenges, one of which is to fabricate photonic structures resonating at low wavelengths. For iScat, a green laser is typically used, because lower wavelengths generate higher scattering signals (according to the λ^{-4} scaling of Rayleigh scattering). Achieving resonances in the green wavelength range (here precisely 520 nm) requires low grating periods, which in turn can only be achieved with low filling factors due to RIE aspect ratio limitations of the etched slots.

Fabricating nanostructures with the correct parameters and ensuring the right incidence angle to excite a dark mode with the single wavelength of the iScat laser would require high precision. Therefore, tuning of the grating period can help to ensure a resonance and to help identify the required period. Preliminary experimental data, which have been collected with Manuel Deckart in the setup he built in our group, showing such resonances are displayed in 60 in comparison to the corresponding simulations.

The nanostructure itself will already break symmetry and introduce non-resonant scattering because of the non-perfect fabrication and non-zero surface roughness. It is therefore currently unknown to which degree the field could be enhanced in practice and how much higher the scattering of the protein will be compared to the scattering introduced by surface roughness alone. The average surface roughness of commercial Si_3N_4 introduces peak values in the order of approximately 1 nm while proteins like IgG have a size of approximately 10 nm. Moreover, the scattered signal from the surface roughness is static, while protein interactions are not, which means that image post-processing can remove the background scattering signal.

One positive aspect is that the low reflectance associated with high-Q resonances is an advantage, because ideally, we would want a high field enhancement to increase the scattered signal but without high reflectance since this adds to the reference intensity and would need to be dimmed. Note that the simulations shown in Figure 60 show the

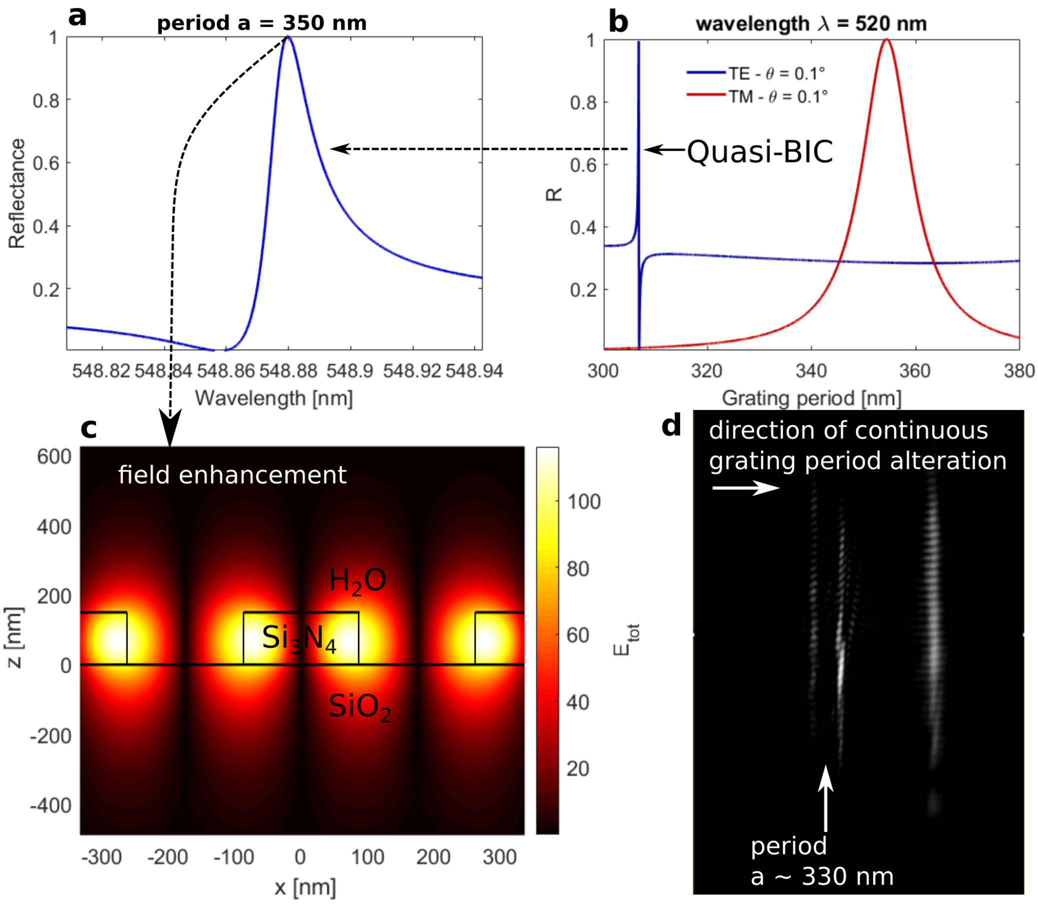

Figure 60: Simulation and first experimental data of Quasi BIC resonances for resonantly enhanced iScat. **a** Simulated spectrum of Quasi BIC in Si_3N_4 grating with 0.1° angle of incidence to break symmetry for the purpose of identifying a resonance wavelength to simulate the field enhancement shown in **c**. **b** shows the resonance response depending on the grating period for TE and TM polarised light. The Quasi-BIC mode is excited with TE polarised light. This 'period-spectrum' is realised experimentally by tuning the grating period in one direction and achieving a spatially defined spectrum in the imaged grating as shown in **d**. The modes seen in this chirped grating in **d** are not yet in accordance with the simulations. The experimental period sweep was fabricated in a range from 300 nm to 400 nm and the image is taken with 45° polarised light where the left resonances at around 330 nm period are TE modes and the right mode at around 350 nm period is a TM mode. These measurements were taken with Manuel Deckart in the iScat setup that he built in our group.

field enhancement of a 'near-Γ-BIC' mode at an incidence angle of 0.1°. This approximation is necessary to be able to carry out these simulations, but it does not represent the expected field enhancement, which could be achieved experimentally when non-perfect fabrication and surface roughness would reduce the theoretically infinite field enhancement found at the Γ-point to an unknown degree.

An alternative idea for future studies on resonantly enhanced iScat is the possibility to use the intrinsic destructive interference between the guided mode and the background Fabry-Perot signal to reach a field enhancement while working in the dark field regime with normal incidence. For example, in Figure 60a, the dip of the Fano resonance at $\lambda \approx 548.86\,\mathrm{nm}$ will have a lower degree of field enhancement compared to the peak, while providing the advantage of zero reflectance. The field enhancement in the peak dip would be stronger for higher index materials, because these would generate a higher background leading to the destructive interference at wavelengths closer to the maximum field enhancement at the resonance wavelength. In this way, high field enhancement with low reflectance values could be reached, but it should be noted that using higher index materials, e.g. hydrogenated amorphous silicon, would be challenging at low wavelengths due to absorption losses.

7 Overall summary and conclusions

The main goal of the work presented in this thesis was to find a feasible way of measuring the phase response of resonant dielectric nanostructures for sensing. This aim was based on the assumption that the advantage of the well-known high sensitivity of interferometric approaches would translate into a better sensing performance with resonant photonics compared to usual read-out approaches. The main challenge was to maintain this advantage of interferometry while also preserving simplicity and cost-efficiency. This effectively means that no active stabilisation, which is commonly applied to interferometric sensing, could be used.

Instead, I implemented a common-path approach to maintain stability by introducing the novel concept of spatially superimposing two beams carrying the phase information of two independently excited resonant modes with different phase sensitivities, and interferometrically measuring the relative phase difference between them. This idea can be applied to other resonant nanostructures and metamaterials. For example, by using higher refractive index materials, a higher surface sensitivity and thus an even lower limit of detection for biomolecules could be achieved in the future. Further, the application of this idea does not require form birefringence of the resonant structure, meaning that nanostructures with two-dimensional symmetry can also be used, which further adds to the versatility of the approach.

The results of this thesis allow to conclude that probing the phase response of guided-mode resonances does provide an improved limit of detection compared to previously applied methods. The most critical aspect of this performance improvement, based on my data, appears to be the ability to create comparably clean data from the generated spatial interferograms using Fourier analysis, which results in low, intensity-independent noise levels. To reach this low-noise regime however, care must be taken to consider all potential sources of noise, as discussed in detail in the thesis.

One further advantage of interferometry compared to spectral peak-tracking is the ability to use a low-cost laser diode, which not only retains simplicity, but also allows to collimate the excitation beam to a higher degree than possible with a typical broadband source, enabling to probe potentially even higher Q-factors than the approximate Q-factor of 1000 achieved here. In other words, the Q-factor of a resonant mode in an interferometric read-out approach could potentially be limited by scattering losses due to the surface roughness of the dielectric material, which corresponds to much higher Q-factors than those measurable with a typical spectrometer. An intensity based read-out has the same advantage of not being limited by spectrometer resolution, but intensity noise is typically orders of magnitude higher than phase noise, as discussed in the thesis. Therefore, creating a spatial interferogram is key.

To discuss the future steps towards a prototype diagnostic tool, I also want to mention the limitations of the current bench-top setup as described in the main body of this thesis. First, the sensing shown here relies on microfluidic channels for local antibody immobilisation, which limits the multiplexing capabilities. An important next step is therefore to use a spotter to immobilise antibodies in specific small areas in the field-of-view to allow true multiplexing. Further, the fabrication technique that I used for this work relies on electron-beam lithography and has to be replaced eventually with a more feasible mass-production technique, i.e., nanoimprinting lithography.

This brings me to the final, more general, conclusion regarding the required next steps towards point-of-care diagnostic technology. While the focus of my thesis lies on the development of a novel sensing technology and the protein sensing experiments are proof-of-principle tests, the most important aspect of the implementation of a miniaturised interferometric setup, as discussed in the outlook of my thesis, is reliability. To potentially achieve high accuracy in diagnostics, the sensor has to provide reliability not only in terms of the photonic aspect of, e.g., high fabrication tolerance but also in terms of the surface functionalisation aspects.

As a last comment, I want to mention that there are a few open questions that appeared during this work. For example, the origin of unexpected fringes when resonantly illuminating with coherent light at non-zero angles of incidence as seen in Figure 57, remains unknown to the best of my knowledge and it will be interesting to search for a possible explanation in the future.

References

[1] Soler, M., Olalla Calvo-Lozano and, M. C. E. & Lechuga, L. M. Nanophotonic biosensors: Driving personalized medicine. *Opt. Photon. News* **31**, 24–31 (2020).

[2] Holmes, A. H. *et al.* Understanding the mechanisms and drivers of antimicrobial resistance. *Lancet* **387**, 176–187 (2016).

[3] Lequin, R. M. Enzyme immunoassay (eia)/enzyme-linked immunosorbent assay (elisa). *Clinical Chemistry* **51**, 2415–2418 (2005).

[4] Luan, E. X., Shoman, H., Ratner, D. M., Cheung, K. C. & Chrostowski, L. Silicon photonic biosensors using label-free detection. *Sensors* **18** (2018).

[5] WHO. Antimicrobial resistance: global report on surveillance 2014. Report (2014).

[6] Panacek, A. *et al.* Bacterial resistance to silver nanoparticles and how to overcome it. *Nature Nanotechnology* **13**, 65–+ (2018).

[7] D'Costa, V. M. *et al.* Antibiotic resistance is ancient. *Nature* **477**, 457–461 (2011).

[8] Fleming, A. On the antibacterial action of cultures of a penicillium, with special reference to their use in the isolation of b. influenzae. *British Journal of Experimental Pathology* **10**, 226–236 (1929).

[9] Syal, K. *et al.* Current and emerging techniques for antibiotic susceptibility tests. *Theranostics* **7**, 1795–1805 (2017).

[10] Abraham, E. P. & Chain, E. An enzyme from bacteria able to destroy penicillin. *Nature* **146**, 837–837 (1940).

[11] Holden, M. T. G. *et al.* A genomic portrait of the emergence, evolution, and global spread of a methicillin-resistant staphylococcus aureus pandemic. *Genome Research* **23**, 653–664 (2013).

[12] Shrivastav, A. M., Cvelbar, U. & Abdulhalim, I. A comprehensive review on plasmonic-based biosensors used in viral diagnostics. *Communications Biology* **4** (2021).

[13] Leitis, A. *et al.* Angle-multiplexed all-dielectric metasurfaces for broadband molecular fingerprint retrieval. *Science Advances* **5** (2019).

[14] Gauglitz, G. Critical assessment of relevant methods in the field of biosensors with direct optical detection based on fibers and waveguides using plasmonic, resonance, and interference effects. *Analytical and Bioanalytical Chemistry* **412**, 3317–3349 (2020).

[15] Merkoci, A., Li, C. Z., Lechuga, L. M. & Ozcan, A. Covid-19 biosensing technologies. *Biosensors & Bioelectronics* **178** (2021).

[16] Troia, B., Paolicelli, A., De Leonardis, F. & Passaro, V. M. N. *Photonic Crystals for Optical Sensing: A Review* (2013).

[17] Nguyen, H. H., Park, J., Kang, S. & Kim, M. Surface plasmon resonance: A versatile technique for biosensor applications. *Sensors* **15**, 10481–10510 (2015).

[18] Tagit, O. & Hildebrandt, N. Fluorescence sensing of circulating diagnostic biomarkers using molecular probes and nanoparticles. *Acs Sensors* **2**, 31–45 (2017).

[19] Musumeci, D., Platella, C., Riccardi, C., Moccia, F. & Montesarchio, D. Fluorescence sensing using dna aptamers in cancer research and clinical diagnostics. *Cancers* **9** (2017).

[20] Yesilkoy, F. Optical interrogation techniques for nanophotonic biochemical sensors. *Sensors* (2019).

[21] Homola, J. Surface plasmon resonance sensors for detection of chemical and biological species. *Chemical Reviews* **108**, 462–493 (2008).

[22] Svedendahl, M., Chen, S., Dmitriev, A. & Kall, M. Refractometric sensing using propagating versus localized surface plasmons: A direct comparison. *Nano Letters* **9**, 4428–4433 (2009).

[23] Shrivastav, A. M., Cvelbar, U. & Abdulhalim, I. A comprehensive review on plasmonic-based biosensors used in viral diagnostics. *Communications Biology* **4** (2021).

[24] Xue, T. Y. *et al.* Ultrasensitive detection of mirna with an antimonene-based surface plasmon resonance sensor. *Nature Communications* **10** (2019).

[25] Minopoli, A. *et al.* Ultrasensitive antibody-aptamer plasmonic biosensor for malaria biomarker detection in whole blood. *Nature Communications* **11** (2020).

[26] Kabashin, A. V. & I., N. P. Interferometer based on a surface-plasmon resonance for sensor applications. *Quantum Electronics* **27** (1997).

[27] Huang, Y., Pui, H. H., Kai, K. S. & V., K. A. Phase-sensitive surface plasmon resonance biosensors: methodology, instrumentation and applications. *Annalen der Physik* **524**, 637–662 (2012).

[28] Yesilkoy, F. *et al.* Phase-sensitive plasmonic biosensor using a portable and large field-of-view interferometric microarray imager. *Light: Science & Applications* **7** (2017).

[29] Fabri-Faja, N. *et al.* Early sepsis diagnosis via protein and mirna biomarkers using a novel point-of-care photonic biosensor. *Analytica Chimica Acta* **1077**, 232–242 (2019).

[30] Li, X. K. *et al.* Plasmonic nanohole array biosensor for label-free and real-time analysis of live cell secretion. *Lab on a Chip* **17**, 2208–2217 (2017).

[31] Estevez, M. C., M., A. & M., L. L. Integrated optical devices for lab-on-a-chip biosensing applications. *Laser & Photonics Reviews* **6**, 463–487 (2011).

[32] Lechuga, L. M. *et al.* Biosensing microsystem platform based on the integration of si mach-zehnder interferometer, microfluidics and grating couplers. In *Conference on Silicon Photonics IV*, vol. 7220 of *Proceedings of SPIE* (2009).

[33] Schmitt, K., Bernd, S. & and, H. C. Interferometric biosensor based on planar optical waveguide sensor chips for label-free detection of surface bound bioreactions. *Biosensors and Bioelectronics* **22**, 2591–2597 (2007).

[34] Kitsara, M., Misiakos, K., Raptis, I. & Makarona, E. Integrated optical frequency-resolved mach-zehnder interferometers for label-free affinity sensing. *Optics Express* **18**, 8193–8206 (2010).

[35] Zinoviev, K. E., Gonzalez-Guerrero, A. B., Dominguez, C. & Lechuga, L. M. Integrated bimodal waveguide interferometric biosensor for label-free analysis. *Journal of Lightwave Technology* **29**, 1926–1930 (2011).

[36] Maldonado, J., Gonzalez-Guerrero, A. B., Fernandez-Gayela, A., Gonzalez-Lopez, J. J. & Lechuga, L. M. Ultrasensitive label-free detection of unamplified multidrug-resistance bacteria genes with a bimodal waveguide interferometric biosensor. *Diagnostics* **10** (2020).

[37] Ruiz-Vega, G., Soler, M. & Lechuga, L. M. Nanophotonic biosensors for point-of-care covid-19 diagnostics and coronavirus surveillance. *Journal of Physics-Photonics* **3** (2021).

[38] Pitruzzello, G. & F., K. T. Photonic crystal resonances for sensing and imaging. *Journal of Optics* **20** (2018).

[39] Magnusson, R. & Ieee. The guided-mode resonance biosensor: Principles, models, and applications. In *IEEE Photonics Conference (IPC)*, IEEE Photonics Conference (2020).

[40] Wang, S. S. & R., M. Theory and applications of guided-mode resonance filters. *Applied Optics* **32**, 2606–2613 (1993).

[41] Cunningham, B., Li, P., Lin, B. & Pepper, J. Colorimetric resonant reflection as a direct biochemical assay technique. *Sensors and Actuators B-Chemical* **81**, 316–328 (2002).

[42] Triggs, G. J. *et al.* Chirped guided-mode resonance biosensor. *Optica* **4**, 229–234 (2017).

[43] Tittl, A., Aleksandrs, L., Mingkai, L., Filiz, Y. & and, C. D.-Y. Imaging-based molecular barcoding with pixelated dielectric metasurfaces. *Science* **360**, 1105–1109 (2018).

[44] Yesilkoy, F. *et al.* Ultrasensitive hyperspectral imaging and biodetection enabled by dielectric metasurfaces. *Nature Photonics* **13**, 390–396 (2019).

[45] Magnusson, R., J., L. K. & D., W. Guided-mode resonance biosensors employing phase detection (2004).

[46] Kuo, W.-K., Ning-Chi, H., Hsueh-Ping, W. & Hsin-Her, Y. Tunable phase detection sensitivity of transmitted-type guided-mode resonance sensor in a heterodyne interferometer. *Optics Express* **22**, 22968–22973 (2014).

[47] Kuo, W.-K., Siang-He, S., Peng-Zhi, L. & Her, Y. H. Tunable sensitivity phase detection of transmitted-type dual-channel guided-mode resonance sensor based on phase-shift interferometry. *Applied Optics* **55**, 903–907 (2016).

[48] Sahoo, P. K., S., S. & J., J. High sensitivity guided-mode-resonance optical sensor employing phase detection. *Scientific Reports* **7** (2017).

[49] Barth, I., Conteduca, D., Reardon, C., Johnson, S. & Krauss, T. F. Common-path interferometric label-free protein sensing with resonant dielectric nanostructures. *Light-Science & Applications* **9** (2020).

[50] Drayton, A., Isabel, B. & F., K. T. Guided mode resonances and photonic crystals for biosensing and imaging 115–148 (2019).

[51] Kenaan, A. *et al.* Guided mode resonance sensor for the parallel detection of multiple protein biomarkers in human urine with high sensitivity. *Biosensors & Bioelectronics* **153** (2020).

[52] Li, K. Z. *et al.* Extended kalman filtering projection method to reduce the 3 sigma noise value of optical biosensors. *Acs Sensors* **5**, 3474–3482 (2020).

[53] Conteduca, D. *et al.* Dielectric nanohole array metasurface for high-resolution near-field sensing and imaging (2020).

[54] Feynman, R. P., Leighton, R. B. & Sands, M. *The Feynman Lectures on Physics* (California Institute of Technology, 1963). URL `https://www.feynmanlectures.caltech.edu/info/`.

[55] Joannopoulos, J. D., Johnson, S. G., Winn, J. N. & Meade, R. D. *Photonic Crystals: Molding the Flow of Light - Second Edition* (Princeton University Press, 2008), 2 edn.

[56] Saleh, B. E. A. & Teich, M. C. *Fundamentals of Photonics, 2 Volume Set, 3rd Edition* (Wiley, 2019).

[57] Joannopoulos, J. D., G., J. S., N., W. J. & D., M. R. *Photonic Crystals: Molding the Flow of Light, second edition* (Princeton University Press, 2008).

[58] Feynman, R. P. *QED: The Strange Theory of Light and Matter* (Penguin, 1990).

[59] Yariv, A. *Fiber and Integrated Optics - Chapter 10: THE COUPLED-MODE FORMALISM IN GUIDED-WAVE OPTICS* (Springer, 1979).

[60] M., B., C., S. & A., G. *Evanescent Waves in Optical Waveguides. In: Evanescent Waves in Optics.*, vol. 206 (Springer Series in Optical Sciences, 2017).

[61] Wood, R. W. On a remarkable case of uneven distribution of light in a diffraction grating spectrum. *Philosophical Magazine* **4**, 396–402 (1902).

[62] Gao, X. W. *et al.* Formation mechanism of guided resonances and bound states in the continuum in photonic crystal slabs. *Scientific Reports* **6** (2016).

[63] Turnbull, G. A., Andrew, P., Jory, M. J., Barnes, W. L. & Samuel, I. D. W. Relationship between photonic band structure and emission characteristics of a polymer distributed feedback laser. *Physical Review B* **64** (2001).

[64] Bykov, D. A., Doskolovich, L. L. & Soifer, V. A. Coupled-mode theory and fano resonances in guided-mode resonant gratings: the conical diffraction mounting. *Optics Express* **25**, 1151–1164 (2017).

[65] Fano, U. Effects of configuration interaction on intensities and phase shifts. *Physical Review* **124**, 1866 (1961).

[66] Miroshnichenko, A. E., Flach, S. & Kivshar, Y. S. Fano resonances in nanoscale structures. *Reviews of Modern Physics* **82**, 2257–2298 (2010).

[67] Joe, Y. S., Satanin, A. M. & Kim, C. S. Classical analogy of fano resonances. *Physica Scripta* **74**, 259–266 (2006).

[68] Hsu, C. W. *et al.* Observation of trapped light within the radiation continuum. *Nature* **499**, 188–191 (2013).

[69] Liu, M. K. & Choi, D. Y. Extreme huygens' metasurfaces based on quasi-bound states in the continuum. *Nano Letters* **18**, 8062–8069 (2018).

[70] Hsu, C. W., Zhen, B., Stone, A. D., Joannopoulos, J. D. & Soljacic, M. Bound states in the continuum. *Nature Reviews Materials* **1** (2016).

[71] Sun, Y. Y. *et al.* Dual-band fano resonance of low-frequency sound based on artificial mie resonances. *Advanced Science* **6** (2019).

[72] White, I. M. & Fan, X. D. On the performance quantification of resonant refractive index sensors. *Optics Express* **16**, 1020–1028 (2008).

[73] Dyson, J. Very stable common-path interferometers and applications. *Journal of the Optical Society of America* **53**, 690 (1963).

[74] Falldorf, C., Osten, S., von Kopylow, C. & Juptner, W. Shearing interferometer based on the birefringent properties of a spatial light modulator. *Optics Letters* **34**, 2727–2729 (2009).

[75] Terborg, R. A., Pello, J., Mannelli, I., Torres, J. P. & Pruneri, V. Ultrasensitive interferometric on-chip microscopy of transparent objects. *Science Advances* **2** (2016).

[76] Padgett, M. J. & Harvey, A. R. A static fourier-transform spectrometer based on wollaston prisms. *Review of Scientific Instruments* **66**, 2807–2811 (1995).

[77] Backoach, O., Kariv, S., Girshovitz, P. & Shaked, N. T. Fast phase processing in off-axis holography by cuda including parallel phase unwrapping. *Optics Express* **24**, 3177–3188 (2016).

[78] Young, G. *et al.* Quantitative mass imaging of single biological macromolecules. *Science* **360**, 423–+ (2018).

[79] Biovendor. Procalcitonin human elisa. *Website* (2021). URL `https://www.biovendor.com/`.

[80] Kurbatova, N. *et al.* Urinary metabolic phenotyping for alzheimer's disease. *Scientific Reports* **10** (2020).

[81] Dresser, L., Hunter, P. & Quinn, S. D. Amyloid oligomerization monitored by single-molecule stepwise photobleaching. *Methods* (2020).

[82] Liu, Y. H. *et al.* Optofluidic vapor sensing with free-space coupled 2d photonic crystal slabs. *Scientific Reports* **9** (2019).

[83] Drayton, A., Li, K. Z., Simmons, M., Reardon, C. & Krauss, T. F. Performance limitations of resonant refractive index sensors with low-cost components. *Optics Express* **28**, 32239–32248 (2020).

[84] Cappi, G. *et al.* Label-free detection of tobramycin in serum by transmission-localized surface plasmon resonance. *Analytical Chemistry* **87**, 5278–5285 (2015).

[85] Acimovic, S. S. *et al.* Lspr chip for parallel, rapid, and sensitive detection of cancer markers in serum. *Nano Letters* **14**, 2636–2641 (2014).

[86] Jang, H. R., Wark, A. W., Baek, S. H., Chung, B. H. & Lee, H. J. Ultrasensitive and ultrawide range detection of a cardiac biomarker on a surface plasmon resonance platform. *Analytical Chemistry* **86**, 814–819 (2014).

[87] Soler, M. *et al.* Direct detection of protein biomarkers in human fluids using site-specific antibody immobilization strategies. *Sensors* **14**, 2239–2258 (2014).

[88] Koshelev, K., Favraud, G., Bogdanov, A., Kivshar, Y. & Fratalocchi, A. Non-radiating photonics with resonant dielectric nanostructures. *Nanophotonics* **8**, 725–745 (2019).

[89] Molina, M. I., Miroshnichenko, A. E. & Kivshar, Y. S. Surface bound states in the continuum. *Physical Review Letters* **108** (2012).

[90] Cole, D., Young, G., Weigel, A., Sebesta, A. & Kukura, P. Label-free single-molecule imaging with numerical-aperture shaped interferometric scattering microscopy. *Acs Photonics* **4**, 211–216 (2017).

[91] Taylor, R. W. & Sandoghdar, V. Interferometric scattering microscopy: Seeing single nanoparticles and molecules via rayleigh scattering. *Nano Letters* **19**, 4827–4835 (2019).

[92] Taylor, R. W. *et al.* Interferometric scattering microscopy reveals microsecond nanoscopic protein motion on a live cell membrane. *Nature Photonics* **13**, 480–+ (2019).

[93] Ortega-Arroyo, J. & Kukura, P. Interferometric scattering microscopy (iscat): new frontiers in ultrafast and ultrasensitive optical microscopy. *Physical Chemistry Chemical Physics* **14**, 15625–15636 (2012).

[94] Li, N. T. *et al.* Photonic resonator interferometric scattering microscopy. *Nature Communications* **12** (2021).

[95] Harper, K. R. *Teory, Design, and Fabrication of Diffractive Grating Coupler for Slab Waveguide*, vol. 101 (All Theses and Dissertations, 2003).

[96] Moharam, M. G., Grann, E. B., Pommet, D. A. & Gaylord, T. K. Formulation for stable and efficient implementation of the rigorous coupled-wave analysis of binary gratings. *Journal of the Optical Society of America a-Optics Image Science and Vision* **12**, 1068–1076 (1995).

[97] Moharam, M. G., Pommet, D. A., Grann, E. B. & Gaylord, T. K. Stable implementation of the rigorous coupled-wave analysis for surface-relief gratings - enhanced transmittance matrix approach. *Journal of the Optical Society of America a-Optics Image Science and Vision* **12**, 1077–1086 (1995).

[98] Liu, V. Lua api reference. *https://web.stanford.edu/group/fan/S4/lua_api.html* **2021** (2013).

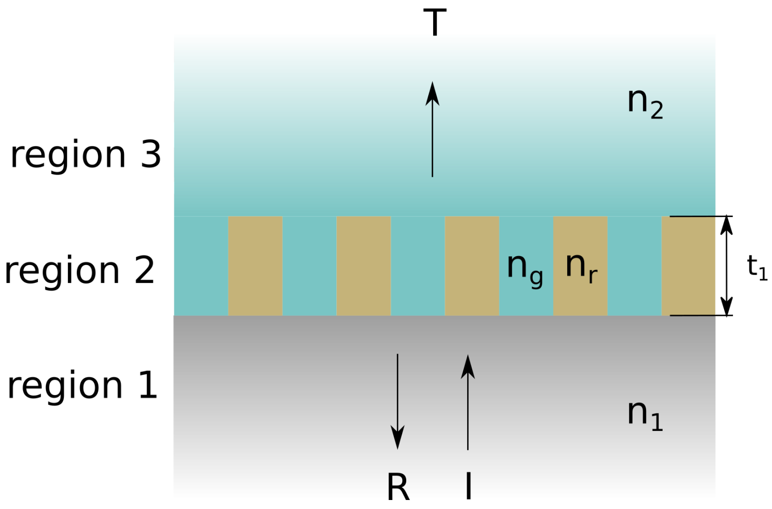

Figure 61: Binary grating as exemplary structure in RCWA.

8 Appendix

8.1 Simulation methods

8.1.1 Rigorous coupled wave analysis - principle and implementation

Rigorous coupled wave analysis (RCWA) is a widely used computation method to determine diffraction efficiencies of binary gratings as relevant for this work. The three layers (substrate, grating, cover) are assumed to be infinitely extended in the direction of the grating vector and the first region (cover region) as well as the third region (substrate region) further extend infinitely in the vertical direction around the periodic grating.

The infinite periodicity of the grating allows to describe the grating with a Fourier series. By taking the boundary conditions for the electric field of each layer into account as given by Maxwell's equations, the total electric field can be expressed as set of coupled wave equations which are solved numerically.

For some of the simulations shown in this work, which are indicated as RCWA-simulations, I modified and used a script originally implemented in MATLAB by Dr Graham Triggs in our group. The script is based on that by D. Brundrett published in [95] (pp. 149-153), which in turn is based on 'Formulation for stable and efficient implementation of the rigorous coupled-wave analysis of binary gratings' [96] and 'Stable implementation of the rigorous coupled-wave analysis of surface-relief gratings:enhanced transmittance matrix approach' [97] by Moharam et. al.

Some of the simulations presented in this work, in particular the E-field confinement simulations, are based on my own scripts using the Stanford Stratified Structure Solver which is explained in detail in the following.

8.1.2 Stanford Stratified Structure Solver (S^4)

Stanford Stratified Structure Solver (S^4) is a frequency domain code to solve the linear Maxwell's equations in layered periodic structures. Internally, it uses RCWA and the S-matrix algorithm. For this work, the program is implemented using a Lua frontend. S^4 was developed by Victor Liu of the Fan Group in the Stanford Electrical Engineering Department and it is freely available on their website. Using S^4 requires writing a Lua script to call S^4. All of the S^4 specific functions that can be called within the Lua environment are described and explained here [98].

8.1.3 S^4 simulation harmonics convergence test

A sufficient number of harmonics has to be used for accurate and converging results and in Figure 62, I illustrate this statement with simulations of spectra showing the convergence of the resonance wavelength with increasing number of harmonics. Most of the simulations shown in this work are carried out with 20 harmonics.

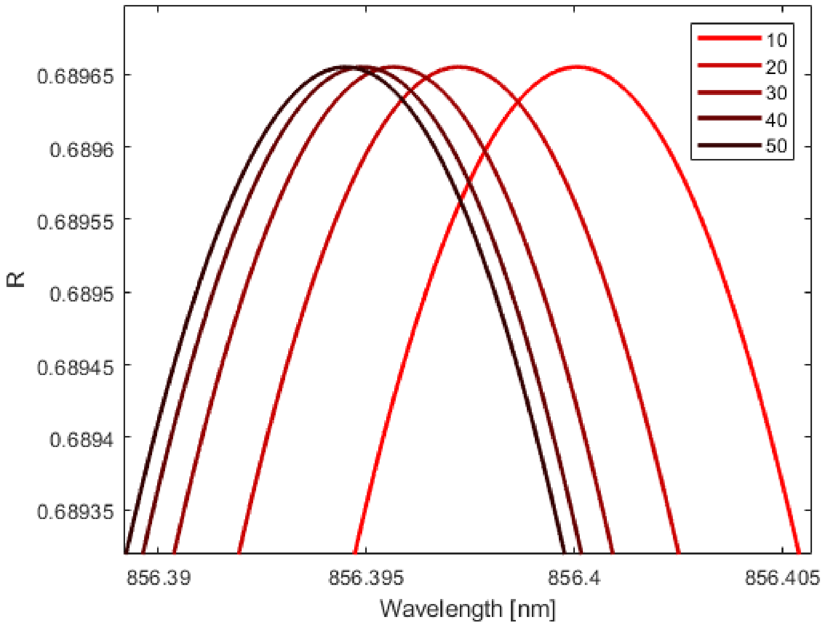

Figure 62: S^4-simulations of typical 1D GMR resonance to illustrate exemplary test of convergence. Since the required number of harmonics depends on the specific requirements of the simulation in each case, there is no general conclusion on necessary number of harmonics available. The conclusion is that care needs to be taken when simulating with RCWA to be sure the number of harmonics is sufficiently high for the accuracy that is required.

8.2 Detailed experimental methods

The following methods were used but not invented or advanced by myself and are as such not part of the novelty of this work, unless indicated in the main body of this thesis.

8.2.1 Dielectric nanostructure fabrication

Commercial wafers consisting of a 150 nm thick film of Si_3N_4 on a 500-μm glass substrate (Silson, UK) are diced into (15x15)mm^2 pieces before cleaning them by sonication in acetone (ACE) for 10 min, rinsing in isopropanol (IPA), and placing in a plasma asher for 5 min. The resist used for electron-beam lithography (EBL) is AR-P 6200.13 from Allresist GmbH spun at 5000 rpm for 60 s and baked on a hotplate at 180 °C for 5 min. For charge dissipation during EBL exposure, we use the conductive polymer AR-PC 5090 (Allresist GmbH) spun at 2000 rpm and baked on a hotplate at 90 °C for 2 min. The pattern is written with a Voyager EBL system from Raith GmbH, 50 kV, with a beam current of 130 pA and a dose of 150 μCmm^{-2}. After removing the charge dissipation layer in deionized water at room temperature for 2 min, I develop the pattern in xylene for 2 min at room temperature, and stop the development with a rinse in IPA. Next, the pattern is transferred into the Si_3N_4 layer by plasma-based reactive ion etching (RIE) using a gas mixture of O_2 and CHF_3 at a ratio of 2:58. After etching for 7 min, I remove the remaining resist with gentle sonication in a 1165 Microposit Remover (Shipley) for 10 min.

8.2.2 Microfluidics fabrication

To fabricate a mold for the polydimethylsiloxane (PDMS) channels, I first clean a silicon wafer piece with sonication in ACE and a rinse in IPA and deionized H_2O. I spin the permanent epoxy-negative photoresist SU-8 2050 (Microchem Inc.) at a speed of first 150 rpm for 10 s, then 750 rpm for 10s, and finally 1000 rpm for 60 s to reach a

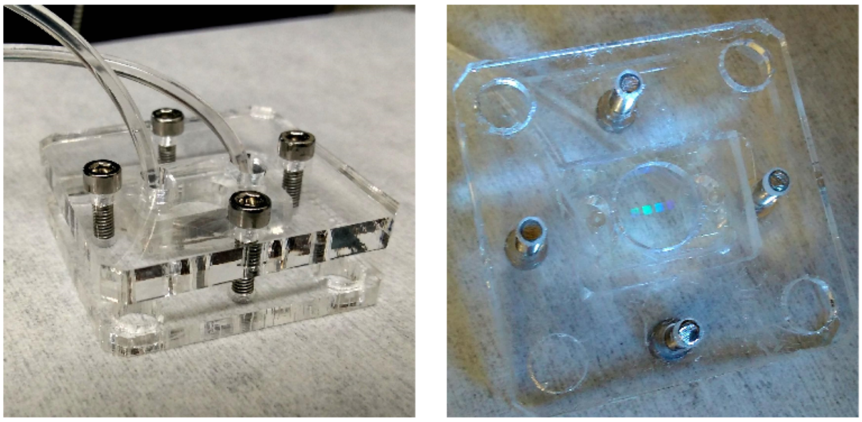

Figure 63: Microfluidic clamping system system. The metal screws are used to clamp the PDMS microfluidic channel to the sensor by applying even pressure using the transparent plastic disks. The tubing is then inserted into the micropunched PDMS channels through small holes in the plastic holder disks. On the right, the sample is flipped such that the photonic sensors are visible as shiny squares through the opening that is left in the disks to illuminate the sample from the bottom.

thickness of $\approx$170 μm, and soft-bake at 65°C for 5 min and then 95 °C for 30 min. Next, the pattern is exposed with direct laser writing (KLOE DILASE, λ = 375 nm) with a 10X objective, 1 mm s^{-1} stage speed, and 65% modulation. Following exposure, I post exposure bake at 65 °C for 5 min and 95 °C for 12 min. Then, the pattern is developed in EC solvent at room temperature for 15 min with constant agitation. I stop the process with a rinse in IPA, and leave the sample in an oven at 180 °C overnight. The PDMS is created by mixing elastomer and curing agent at a ratio of 7:1 and leaving it in a desiccator for 20 min to remove air. This mixture is then poured over the channel mold and baked at 60 °C overnight. I remove the PDMS from the mold, and use a micropuncher to create holes for the microfluidic tubing (Tygon E-3606, 0.8 mm inner diameter).

8.2.3 Surface functionalisation protocol

First, the sensor is cleaned in Piranha solution, which consists of a mixture of sulfuric acid and hydrogen peroxide at a ratio of 21:9. This step also ensures hydroxylation of the sensor surface, which is necessary for the salinisation step following cleaning. To salinise the Si_3N_4 surface, I leave it in a 5% solution of (3-mercaptopropyl)trimethoxysilane (MPTS) in dry ethanol for 6 h. Following a rinse in ethanol and in dimethyl sulfoxide (DMSO), I functionalize the surface overnight with a PEGylated SMCC cross-linker (SM(PEG)6 from Thermo Fisher) at a concentration of 1 mM in DMSO while avoiding exposure to humidity during this process. Following a rinse in DMSO and drying the sensor with nitrogen, I clamp it to a microfluidic channel made of PDMS, and the remainder of the surface functionalisation protocol takes place in this microfluidic system at room temperature. I use a microfluidic pump to pull the solutions over the surface through the microfluidic channels at $20\,\mu\mathrm{L\,min^{-1}}$. To avoid hydrolysis, I introduce a short PBS baseline for 10 min only before flowing the anti-PCT antibody (Abcam) at a concentration of $50\,\mu\mathrm{g\,mL^{-1}}$ in PBS over the sensor surface for 1 h. Then, a 10-min PBS washing step is introduced before flowing a 1% casein-blocking buffer (diluted 10X casein- blocking buffer from Sigma-Aldrich, UK) for half an hour to ensure that any remaining nonspecific binding sites are blocked before the final target biomarker binding. The PBS washing step after casein is continued, until a flat phase response is reached, which takes 30-45 min. Then, the antigen (e.g. recombinant human PCT protein, Abcam) in PBS is introduced to the functionalised sensor surface.

8.2.4 Optical setup and data acquisition methods

An inverted microscope is used for sensing experiments in reflection, with only a few modifications necessary for phase-sensitive operation. These modifications include using a coherent source, and implementing a Wollaston prism and analyser. The collimated output of a VCSEL-based laser diode module (Thorlabs Inc., CPS850V) is directed toward a lens and focused in the back-focal plane of a 5X objective. The objective collimates the light, and after being resonantly reflected from the GMR sensor, the beam is directed toward the Wollaston prism (Thorlabs Inc., WPQ10) by a beam splitter. The Wollaston prism is aligned and fixed, such that the orthogonally polarised TE and TM modes are split into two diverging beams with approximately equal intensity. The analyser then enables the common components of these beams to interfere, and the interferogram is recorded with a CMOS camera (Thorlabs Inc., Compact USB 2.0 CMOS Camera). The contrast of the interferogram fringes can be adjusted in the beginning of a measurement by rotating the analyser. For sensing experiments, I take images at a rate of 0.2 fps.

8.3 Data processing methods

From the raw camera images, the data processing usually includes the following steps using a custom MATLAB script:

1. image rotation to align fringe direction with x-axis
2. image crop to select ROIs of each grating structure of interest
3. 2D fft filtering of interferogram
4. averaging of filtered interferogram
5. cosine fit for phase extraction

Even though the phase can alternatively be directly extracted from the Fourier transform of the averaged interferogram, I used the above process of cosine fitting to visualise the phase extraction process in a more intuitive way.
For the direct phase extraction based on FFT, the following steps are considered for a practical implementation:

1. image rotation to align fringe direction with x-axis
2. image crop to select ROIs of each grating structure of interest
3. averaging of interferogram to create 1D sinusoidal signal I
4. I_{fft} = fftshift(fft(I)) to extract spatial fringe frequency of averaged interferogram
5. setting values of I_{fft} to zero if corresponding magnitudes are below defined tolerance value
6. extracting phase information by calculating the unwrapped phase angle(I_{fft}) at (positive or negative) spatial interferogram frequency

8.4 List of Figures

List of Figures

1 Schematic principle of biosensor operation as transducer. Biorecognition is commonly achieved with specific antibodies binding to a target molecule while the transducer (biosensor) enables the translation of the biorecognition into a measurable signal. 5

2 Principle of evanescent field refractive index sensing schematic. Any evanscent field refractive index biosensor relies on an effective index change caused by the presence of biomaterial, which perturbes the evanescent field. This effective index change is transduced usually by analysing the response in resonance wavelength or angle. 6

3 Attenuated total reflection method (Kretschmann geometry) used for exciting a surface plasmon resonance. Figure adapted from [17]. . . . 8

4 Schematic of standard planar waveguide Mach-Zehnder-Interferometer configuration adapted from [34]. 9

5 Guided-mode resonance (GMR) schematic sensing principle. A narrow range of wavelengths of the broadband incident light is resonantly guided in the grating layer and coupled out again, such that an intensity peak is observed in reflection. The resulting evanscent field is perturbed by the target biomolecules, which changes the effective index of the ‘leaky’ guided mode. The corresponding change in resonance wavelength is typically observed with a spectrometer. Adapted from [39]. 11

6 Interface between two dielectrics with $\varepsilon_1 > \varepsilon_2$. Light is incident with angle θ_1 and refracted with angle θ_2. Translational symmetry demands that the parallel component $k_{||}$ of the wave vector $\vec{k}$ is conserved. . . . 17

7 A diffraction grating can be seen as the interaction between waves scattered from adjacent point scatterers (grating grooves with distance a). The optical path difference between the waves scattered from adjascent grooves is $a \cdot sin\theta_{out} - a \cdot sin\theta_{in}$. Figure loosely adapted from [54]. . . 18

8 Waveguide schematic with the refractive index of the waveguide material being higher than that of the surrounding medium ($n_{guide} > n_{cladding}$). Rectangular shape of the waveguide with height h. The width in y-direction is not relevant for the considerations since the E-field has only one component in y-direction: $\vec{E} = (0, E_y, 0)$. In fact, the waveguide can be assumed to be infinitely extended in y and x. 20

9 One dimensional grating with discrete translational symmetry, period a and groove width w. The refractive index of the grating surrounding medium is lower than the effective index of the grating layer. 23

10 Simulated dispersion relation of GMR TE-mode. The structure assumed for this S^4-simulation is a one dimensional Si_3N_4-grating with x-y- infinity and height of 150 nm. For this example, there exists up-down mirror symmetry with a SiO_2 substrate and superstrate. 25

11 Schematic of a Fano resonance as a result of the interference between the radiative continuum (Fabry-Perot (FP) effect) and a discrete state of the waveguide. Due to the phase variation of the discrete state with respect to the wavelength (x-axis), and the resulting relative change in phase compared to the continuum, destructive interference leads to a dip on one side of the resonance. On which side the destructive interference is observed depends on the thickness of the waveguide layer because the FP effect determines the relative phase difference between discrete state and continuum. 27

12 Dependence of Fano line shape of TE GMR mode on grating layer thickness. The asymmetry of the resonance peak depends on the thickness because the Fabry-Perot effect in the grating layer depends on it and the resonance peak is a result of interference between the resonance and the FP. The dip in the Fano line shape occurs when there is complete destructive interference between the resonance and the FP, which means when the phase difference is π and the intenisties are the same. 28

13 Top: RCWA simulations of reflectance and phase response of GMR (TE mode) depending on slab thickness. Bottom: Selected exemplary phase responses for specific slab thicknesses in the range between 100 nm and 350 nm. 30

14 Evanescent field in the case of total internal reflection (TIR) from a Si_3N_4-H_2O interface (left) and in the case of a GMR mode in a Si_3N_4 grating on a SiO_2 substrate with a H_2O-cover (middle). The figure on the right shows the evanescent decay from the surface away in z-direction, indicated by the grey dotted lines in the left and middle panel. 31

15 Resonance maps in dependence of grating parameters illustrate the limits of guided-mode resonance excitation in parameter space. The dashed bright blue lines indicate the usual point of operation, meaning the approximate parameter combination which is used for this work. The 4 maps show the dependence on **A** the grating slab thickness t, **B** the grating period a, **C** the refractive index of the dielectric grating material (not effective index) and **D** the filling factor FF of the grating ((a - w)/a see Fig. 9). The parameters, which are kept constant while one parameter is swept, are a = 575 nm, FF = 78%, t = 150 nm and $n_{\text{grating}} = 2.02$. 32

16 Lineiwdth definition depending on peak shape. $\delta\lambda$ for a symmetric line shape is the full-width-at-half-maximum (FWHM) while $\delta\lambda_{\text{fano}}$ depends on the positions of the peak and the dip of the resonance line shape. 35

17 Left: Simulated reflectance response depending on wavelength and bulk index change of the medium surrounding the grating surface. S^4 was used for this simulation and the parameters of the grating are $n_{\text{substrate}} = 1.45$, $n_{\text{grating}} = 2.02$, grating thickness t = 150 nm, filling factor FF = 0.78, TE polarisation. Right: Wavelength shift $\Delta\lambda$ in response to refractive index alteration by $\Delta n = 0.01$. 37

18 Surface sensitivity schematic to illustrate the principle of detecting a thin biolayer. 38

19 Intensity as a function of delay d between two plane waves according to Equation (27), adapted from [56]. 42

20 Interference of two oblique plane waves. Adapted from [56]. 43

21 Schematic of the phase-sensitive detection principle. The figure shows the optical setup where the collimated output of an 855-nm laser diode is focused onto the back-focal plane (BFP) of a 5X objective after passing through a polarising beam splitter. This setup creates collimated light which excites the guided-mode resonance. The grating grooves are oriented at 45° with respect to the polarisation of the incident light, such that the TE and TM modes are equally excited. The resonantly reflected light from the sensor carries information about the effective refractive index encountered by the orthogonally polarized guided modes stored as phase information. The Wollaston prism introduces an angle of 1° between the two modes. The two diverging beams overlap in the camera plane, and generate a high-contrast interferogram for an analyser orientation of approximately 45°. 46

22 Working principle of a Wollaston prism. A light beam passing through the prism is split into two beams with orthogonal polarisation which diverge with an angle α. This is achieved by using a birefringent material which introduces a path difference between the two polarisations. 48

23 **a**, Schematic of a typical GMR structure consisting of a silicon nitride (n=2.02) grating of 150 nm thickness on glass (n=1.45) substrate immersed in water (n=1.33). The grating period in this example is a = 572 nm and the filling factor is 75%. A plane wave is incident from the glass substrate layer. The TE/TM mode is excited when the E-field vector of the incident beam is oriented perpendicular/parallel to the grating vector. **b, c,** Dominant E-field components of TE (y-component) and TM (z-component) modes with an evanescent field decaying from the grating surface into the cover layer. **d,** Simulated reflectance with spectral mode overlap and **e,** simulated phase response, using rigorous coupled wave analysis (RCWA). 49

24 RCWA simulation showing the spectral mode overlap of a single structure for different filling factors (FF). The phase sensitivity is higher for maximised FF, while the spectral overlap for the TE/TM mode is only achieved for a narrow range of lower FF. 50

25 Design parameters (period a, filling factor FF) and corresponding simulated resonance peaks. All other parameters (index, thickness...) are provided in the caption of Fig. 23. Areas within the field-of-view (FOV) designed to excite a TE mode are marked blue and those exciting a TM mode are marked red. The orientation of the grating grooves, for both TE and TM designs, is along the long axis, as indicated in the top right zoom. This design schematic is the basis of the experimental images shown in Figure 28. 52

26 Spectral characterisation of structures designed as shown in Figure 25, here with a wider grating period variation range on the left. The spectra were aquired by taking hyperspectral images using a halogen lamp in combination with a monochromator and recording the intensity in every pixel. On the right, the two spectra correspond to identically designed gratings fabricated on two different samples. 54

27 Top: Schematic of nanofabrication process. Bottom: SEM and AFM of fabricated grating structures in Si_3N_4 with a charge dissipation layer for the SEM to avoid distortions due to charging. A detailed fabrication protocol can be found in Apprendix 8.2.1. 55

28 Schematics and camera images showing the spatial grating overlap principle. Compare to design in Figure 25. **a** Schematic of interferogram formation with spatial mode overlap of adjacent structures designed to resonate for TE/TM polarization shown for 0°, 45°, and 90° analyzer orientations. The blue/red frame indicates the structure resonating for TE/TM polarization. **b** Corresponding analyser orientations and **c** corresponding camera images. The area with a blue frame is a uniform grating designed to resonate at $\lambda = 855\,nm$ in water for TE polarization. Correspondingly, it shows high reflectance for the 0° analyser orientation. The narrow stripes are designed, such that one resonates for TM polarization; since the TM resonance is much narrower, I here use several stripes consisting of gratings with different periods ($\Delta a = 1nm$) to ensure that at least one of them is on resonance within the expected refractive index range of the analyte. This principle ensures a high dynamic range. Correspondingly, only one of the grating stripes lights up at the 90° analyser orientation (red frames). When the analyser axis is set to 45°, the TE and TM components can interfere and create an interferogram in the beam-overlap region. **d** Schematic of sensors integrated in a microfluidic system. I use a signal and a reference channel to enable drift subtraction. **e** Zoom of **c** (middle) 57

29 Principle of phase extraction from interferogram by fast Fourier transform (FFT) with MATLAB script. The 2D interferogram is first averaged orthogonal to the fringe direction and the magnitude of the FFT of this 1D sinusoidal function reveals the spatial fringe frequency (top right), while the phase angle of the complex FFT is used to extract the phase information of this spatial frequency over time. See Appendix 8.3 for details. 58

30 The camera, which is used in the optical setup for interferometry, has a default infrared filter (IR filter) in front of the camera sensor. By removing the filter, the clean, expected fringes are obtained. 59

31 Raw camera images for qualitative comparison of interferogram contrast using a laser diode (left) and a spectrally filtered superluminescent diode (SLED, right). 61

32 SLED interferogram with and without spectral filtering. 62

33 Mechanical noise in the case of mirror as sample when the mirror is not fixed on the sample stage. Overall drift reduces over the course of one hour, while smaller vibrations are still present after this initial stabilisation. 64

34 Noise characterisation - dependence of noise on fringe contrast independent of temperature drift. The sample is a mirror and the laser diode was switched on 1 hour before this measurement to exclude the effect of temperature dependent wavelength drift. The contrasts C are calculated with Eq. (34) and are marked in the corresponding raw image position to show both the absolute contrast and the contrast variation due to the Gaussian beam. 66

35 Example data showing the drift referencing principle. The signal ‘s’ corresponds to the phase response determined in one microfluidic channel and the reference ‘r’ to the signal obtained from the adjacent channel, which is subtracted from the signal to obtain the effective phase response over time while flowing DI H_2O through both channels in this case. 67

36 Variations in the PDMS microfluidic channel thickness as a possible source of noise. The tubing is not mechanically isolated from the PDMS channel, which can lead to pressure being applied to the channel by the tubing, which results in pulling the PDMS around the holes up while the pressure applied by the clamping system pushes the PDMS down, which leads to deformations. 69

37 Raw camera images illustrate backreflections from the PDMS microfluidic channel in air (right image). The interface here is chosen to be air-PDMS (off resonance) because the effect of the backreflections is difficult to visualise for the lower index contrast of a water-PDMS interface. On the left, the effect of using an absorbing layer (‘camouflage’ spray paint) which is sprayed on the PDMS surface inside the channel is visible. The absorbing layer significantly reduces the backreflections, which are not detectable by eye anymore in the left image. 69

38 Experimentally determined refractive index of different glucose-H_2O-solutions. The refractometer which was used has an accuracy of $\Delta n = 10^{-4}$. 71

39 Bulk sensitivity measurements and experimental phase curve. **a** Starting from a H_2O baseline with a refractive index of 1.3331, glucose solutions of a refractive index in a range between 1.3342 and 1.3437 were flowed over the surface, and the corresponding phase response was measured. I repeated the measurement twice for each concentration to verify system stability. **b** Phase curve obtained from the measurement on the left in comparison with the simulated phase response. The error of Φ of each single blue point is determined by calculating the standard deviation of the saturated response in each glucose step shown in **a**. This error is smaller than the marker size in **b**. 72

40 Phase response measured upon introduction of glucose solution of calibrated refracted index. The figure shows the phase response of two adjacent gratings with 1 nm difference in grating period. The standard deviation of Φ over time, which is the data that the graph is based on, while flowing the glucose solutions is smaller than the marker size. The bulk refractive index is calibrated by measuring the refractive index of glucose solutions with a refractometer. The two grating structures are introduced to the same glucose solutions at the same time. The response is referenced with the microfluidic referencing system. 76

41 Measured phase response of two different grating structures, which were fabricated using a difference in electron beam lithography dose factor of 0.05 $\mu C/cm^2$. The errorbars correspond to the standard deviation σ of the phase response over time while flowing each glucose solution. Calibration and experimental details as described in caption of Fig. 40. 77

42 Divergence angle determination. **a** beam profiles at position 0 and position 0 + 20.2cm. **b** camera images of beam profile taken at different camera positions as indicated in setup schematic in **c** 79

43 Schematic of surface functionalisation steps (not to scale). **A** the bare sensor is cleaned either using Piranha or ozone cleaning (see Appendix 8.2.3) to introduce hydroxyl groups on the surface which allows **B** MPTS to form a monolayer on the surface. This MPTS step is called silanisation, during which covalent -Si-O-Si- bonds are formed. **C** SM(PEG)$_6$ binds to the MPTS and forms another monolayer to which **D** any antibody can bind. **E** Casein is a blocking buffer and binds to any remaining non-specific binding sites on the surface. **F** the target antigen then binds to the specifically chosen antibody. 82

44 **a**, Schematic of functionalisation steps and the corresponding phase shift observed experimentally in **b**, Anti-PCT antibodies (50 $\mu g\,mL^{-1}$) are binding to the PEG spacer layer (see methods appendix 8.2.3). After saturating the surface, casein is introduced to block any remaining non-specific binding sites. The following PBS washing results in most of the casein being washed away suggesting the PEG layer is already blocking the surface effectively. We observe a 0.019 π phase shift in equilibrium for a procalcitonin concentration of 1 $pg\,mL^{-1}$. 83

45 PCT control sensing with a commercial Quartz-crystal-microbalance (Biolin Scientific, Qsense Analyzer) instrument. Note that, unlike in the photonic measurement, mass binding registers as a reduction of the resonance value. The anti-PCT antibody concentration is the same as for the measurement shown in Fig. 44, $50\,\mu\mathrm{g\,mL^{-1}}$. The experiments are performed at room temperature and the microfluidic pump speed is $20\,\mu\mathrm{L\,min^{-1}}$, which are the same parameters as for the photonic sensing experiments. 84

46 Procalcitonin sensing with non-specific antibodies as control experiment. The antibodies are specific to immunoglobulin G (anti-IgG antibodies, R2004 Sigma Aldrich). The rest of the experimental details are identical to the previously discussed experiment shown in Fig. 44 with the difference that a higher PCT concentration is chosen to test the specificity at concentrations that are far from the LOD. 85

47 QCM-D amyloid sensing to test the surface functionalisation and, in particular, the specificity by flowing β-amyloid in both a signal and a reference channel, the latter without any antibodies (blue). The arrow on the right indicates the shift in the signal channel upon amyloid binding, which is non-existent in the control experiment. The drift of the system, which is extrapolated by the dashed orange line, should be taken into account when analysing this data. 88

48 Interferometric amyloid sensing with 1D GMR grating 89

49 **a** Design of nanohole array. **b** SEM images of dielectric nanoholes. Both generated by Dr Donato Conteduca. 92

50 Interferometry with dielectric nanoholes in hydrogenated, amorphous silicon instead of silicon nitride fabricated by Dr. Donato Conteduca. The interferogram is created by means of the Wollaston prism as in Figure 28. The difference between this structure and the one-dimensional structures above is not only the two-dimensional periodicity of the nanoholes and the material with higher refractive index but also the choice of resonance wavelength, which here in this image is 635 nm. **a** Interferogram showing several stripes resonating for the 'TM'-mode and a single structure each resonating for the 'TE'-mode. **b** - Spectra of TE and TM modes of dielectric nanoholes resonating around the laser wavelength (red line). The spectra were recorded by Dr. Donato Conteduca. 93

51 Schematic of a miniaturised lensless optical setup using a double slit as diffractive element to replace the Wollaston prism. The light of a collimated laser diode module is used to excite a TM resonance in the GMR sensor. The only difference between TM 1 and TM 2 is their separation by a microfluidic system and their functionalisation. Therefore, TM 1 is a resonant structure operating in channel 1 while the photonically identical TM 2 structure operates in channel 2. The reflected light from each of these channels is then each aligned with a slit such that the interferogram contains information about the relative phase changes between the two channels. This system, as such, is a self-referencing system. 94

52 Raw images demonstrating sensing with a double slit as the diffractive element. On the left, two identical gratings are on resonance and are imaged. On the right, a double slit is aligned with the same gratings such that the light from each grating falls onto one slit only, thereby being able to interfere in the camera plane. The method is based on the well-known Young's slit interference experiment. The images are meant to illustrate the working principle only. 95

53 Refractive index sensing with double-slit read-out in bulk setup for proof-of-principle. The jump in phase corresponds to dropping a small drop of IPA onto the initial water drop which increases the refractive index by an unknown amount. Quantification is not the goal of this test experiment, its purpose is solely to verify the operation of the interferometer with a double slit. 96

54 Consideration with respect to double slit distance, width and camera distance. On the right: corresponding interferogram recorded in the miniaturised setup. Design figure in A by Alexander Drayton. 98

55 IgG sensing in serum using a chirped GMR sensor (no interferometry). 100

56 Simulations showing a symmetry protected Quasi-BIC mode in **a** (compare upper band in Fig. 10), where the symmetry is broken by assuming an incidence angle of $\theta = 0.1°$ as well as **b** a typical TM mode both in the same Si_3N_4-grating with the only difference being the grating period to achieve resonances at similar wavelengths. The Quasi-BIC is based on a grating period a = 527 nm and the TM a = 570 nm both with FF = 0.8. The spectra in **c** qualitatively show the corresponding surface sensitivities by simulating the response with and without a 20 nm thick generic model layer of biomolecules of refractive index n = 1.43 on the surface of the structure. 103

57 Red curve: TM mode spectrum obtained from a chirped grating response (upper right image) when excited with single wavelength laser diode at 855 nm. The green curve was obtained in same manner, but for a Quasi symmetry protected mode excited at the same wavelength as the TM mode in a grating with lower period at an incidence angle of $\approx 1^\circ$. Note that the fringes visible in the bottom camera image on the right are unexpected and their origin will be part of future investigations. Those fringes were not created by means of a Wollaston prism or any other diffractive element. 104

58 Interferometric Scattering Microscopy (iScat) working principle. The scattered light from the particle (e.g. protein) is interfered with a reference field, which is the light reflected from the surface-liquid interface. This superposition of a spherical scattered wave and a plane reference wave results in a characetristic Airy interference pattern where the contrast depends on the particle size and the phase depends on the particle's distances from the surface. Adapted from [92]. 106

59 Dispersion diagram of TE mode in an one-dimensional grating with period a = 350 nm, thickness t = 150 nm and filling factor FF = 50%. The lower band is the even TE mode which is spectrally broad at an incidence angle $\theta = 0^\circ$ (Γ-point) while the upper band odd mode vanishes at $\theta = 0^\circ$ which is the symmetry protected mode discussed in this section for iScat. 107

60 Simulation and first experimental data of Quasi BIC resonances for resonantly enhanced iScat. **a** Simulated spectrum of Quasi BIC in Si_3N_4 grating with 0.1° angle of incidence to break symmetry for the purpose of identifying a resonance wavelength to simulate the field enhancement shown in **c**. **b** shows the resonance response depending on the grating period for TE and TM polarised light. The Quasi-BIC mode is excited with TE polarised light. This 'period-spectrum' is realised experimentally by tuning the grating period in one direction and achieving a spatially defined spectrum in the imaged grating as shown in **d**. The modes seen in this chirped grating in **d** are not yet in accordance with the simulations. The experimental period sweep was fabricated in a range from 300 nm to 400 nm and the image is taken with 45° polarised light where the left resonances at around 330 nm period are TE modes and the right mode at around 350 nm period is a TM mode. These measurements were taken with Manuel Deckart in the iScat setup that he built in our group. 109

61 Binary grating as exemplary structure in RCWA. 125

62 S^4-simulations of typical 1D GMR resonance to illustrate exemplary test of convergence. Since the required number of harmonics depends on the specific requirements of the simulation in each case, there is no general conclusion on necessary number of harmonics available. The conclusion is that care needs to be taken when simulating with RCWA to be sure the number of harmonics is sufficiently high for the accuracy that is required. 127

63 Microfluidic clamping system system. The metal screws are used to clamp the PDMS microfluidic channel to the sensor by applying even pressure using the transparent plastic disks. The tubing is then inserted into the micropunched PDMS channels through small holes in the plastic holder disks. On the right, the sample is flipped such that the photonic sensors are visible as shiny squares through the opening that is left in the disks to illuminate the sample from the bottom. . . . 129